SO(5) theory of antiferromagnetism and superconductivity

Eugene Demler

Department of Physics, Harvard University, Cambridge, Massachusetts 02138, USA

Werner Hanke

Institute for Theoretical Physics, University of Würzburg Am Hubland, D-97074 Würzburg, Germany

Shou-Cheng Zhang

Department of Physics, Stanford University, Stanford, California 94305, USA

(Published 18 November 2004)

Antiferromagnetism and superconductivity are both fundamental and common states of matter. In many strongly correlated systems, including the high-T_c cuprates, the heavy-fermion compounds, and the organic superconductors, they occur next to each other in the phase diagram and influence each other's physical properties. The $SO(5)$ theory unifies these two basic states of matter by a symmetry principle and describes their rich phenomenology through a single low-energy effective model. In this paper, the authors review the framework of the $SO(5)$ theory and compare it with numerical and experimental results.

CONTENTS

I. INTRODUCTION

The phenomenon of superconductivity is one of the most profound manifestations of quantum mechanics in the macroscopic world. The celebrated Bardeen-Cooper-Schrieffer (BCS) theory (Bardeen *et al.*, 1957) of superconductivity provides a basic theoretical framework for understanding this remarkable phenomenon in terms of the pairing of electrons with opposite spin and momentum to form a collective condensate state. Not only does this theory quantitatively explain the experimental data of conventional superconductors, but the basic concepts developed from this theory, including spontaneously broken symmetry, the Nambu-Goldstone modes, and the Anderson-Higgs mechanism, also provide the essential building blocks for the unified theory of fundamental forces. The discovery of high-

temperature (high-T_c) superconductivity (Bednorz and Müller, 1986; Wu *et al.*, 1987) in copper oxide materials poses a profound challenge to our theoretical understanding of superconductivity in the extreme limit of strong correlations. While the basic idea of electron pairing in the BCS theory carries over to high-T_c superconductors, other aspects, like the weak-coupling mean-field approximation and the phonon-mediated pairing mechanism, may not apply without modifications. Therefore high-temperature superconducting systems provide an exciting opportunity to develop new theoretical frameworks and concepts for strongly correlated electronic systems.

Since the discovery of high-T_c superconductivity, a tremendous number of experimental data have been amassed on the cuprates. In this theoretical review it is not possible to give a detailed review of all the experimental findings. Instead, we refer the readers to a number of excellent review articles on the subject (Imada *et al.*, 1998; Kastner *et al.*, 1998; Maple, 1998; Timusk and Statt, 1999; Orenstein and Millis, 2000; Campuzano *et al.*, 2002; Yeh, 2002; Damascelli *et al.*, 2003). Below, we summarize the phase diagram of the high-T_c superconducting cuprates and discuss some of the basic and (more or less) universal properties in each phase.

To date, a number of different high-T_c superconducting materials have been discovered. The best studied of these include hole-doped $La_{2-x}Sr_xCuO_{4+\delta}$ (LSCO), $YBa_2Cu_3O_{6+\delta}$ (YBCO), $Bi_2Sr_2CaCu_2O_{8+\delta}$ (BSCO), and $Tl_2Ba_2CuO_{6+\delta}$ (TBCO) materials, and electron-doped $Nd_{2-x}Ce_xCuO_4$ (NCCO). All these materials have two-dimensional CuO_2 planes and display an antiferromagnetic (AF) insulating phase at half filling. The magnetic properties of this insulating phase are well approximated by the AF Heisenberg model with spin $S=1/2$ and an AF exchange constant $J\sim 100$ meV. The Néel temperature for three-dimensional AF ordering is approximately given by $T_N\sim 300-500$ K. The high-T_c superconducting materials can be doped either by holes or by electrons. In the doping range of $5\% \lesssim x \lesssim 15\%$, there is a superconducting (SC) phase, which has a domelike shape in the temperature-versus-doping plane. The maximal SC transition temperature T_c is of the order of 100 K. The three doping regimes are divided by the maximum of the dome and are called the underdoped, optimally doped, and overdoped regimes, respectively. A generic phase diagram of high-temperature superconductivity is shown in Fig. 1.

One of the main questions concerning the high-T_c superconductivity phase diagram is the transition region between the AF and SC phases. Partly because of the complicated materials chemistry in this regime, there is no universal agreement among experiments. Different experiments indicate several different possibilities, including phase separation with an inhomogeneous density distribution (Howald *et al.*, 2001; Lang *et al.*, 2002), a uniform mixed phase between the AF and SC phases (Brewer *et al.*, 1988; Miller *et al.*, 2003), and periodically ordered spin and charge distributions in the form of stripes or checkerboards (Tranquada *et al.*, 1995).

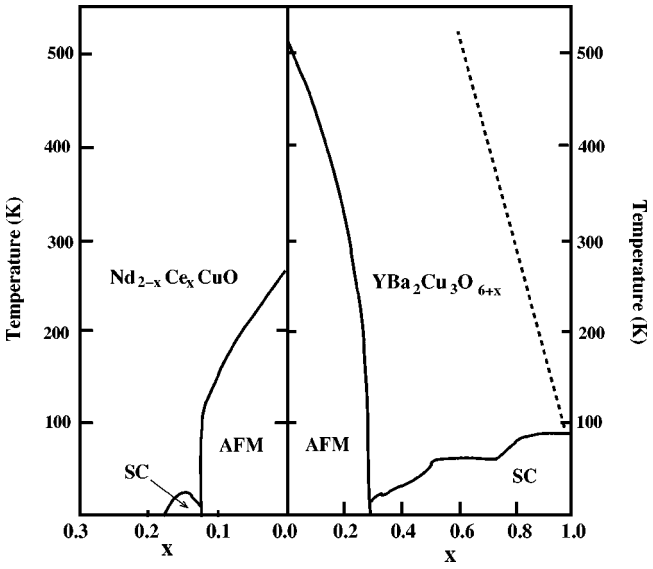

FIG. 1. Phase diagram of the NCCO and the YBCO superconductors.

The phase diagram of the high-T_c cuprates also contains a regime with anomalous behavior conventionally called the *pseudogap phase*. This region of the phase diagram is indicated by the dashed line in Fig. 1. In conventional superconductors, a pairing gap opens up at T_c. In a large class of high-T_c cuprates, however, a gap, which can be observed in a variety of spectroscopic experiments, starts to open up at a temperature T^*, much higher than T_c. Many experiments indicate that the pseudogap "phase" is not a true thermodynamic phase but rather a precursor of crossover behavior. The phenomenology of the pseudogap behavior is extensively reviewed by Timusk and Statt (1999) and Tallon and Loram (2001).

The SC phase of a high-T_c superconductor has a number of striking properties not shared by conventional superconductors. First of all, phase-sensitive experiments indicate that the SC phase of most cuprates has *d*-wave-like pairing symmetry (Van Harlingen, 1995; Tsuei and Kirtley, 2000). This is also supported by photoemission experiments, which show the existence of nodal points in the quasiparticle gap (Campuzano *et al.*, 2002; Damascelli *et al.*, 2003). Neutron-scattering experiments find a new type of collective mode, carrying spin one, lattice momentum close to (π,π), and a resolution-limited sharp resonance energy around 20–40 meV. Most remarkably, this resonance mode appears only below T_c in the optimally doped cuprates. It has been found in a number of materials, including the YBCO, BSCO, and TBCO classes of materials (Rossat-Mignod, Regnault, Vettier, Burlet, *et al.*, 1991; Mook *et al.*, 1993, 1998; Fong *et al.*, 1995, 1996, 1999, 2000; Dai *et al.*, 1996, 1998; He *et al.*, 2001, 2002). Another property quite different from the conventional superconductors is the vortex state. Most high-T_c superconductors are of type II in which the magnetic field can penetrate into the

SC state in the form of a vortex lattice, with the SC order being destroyed at the center of the vortex core. In conventional superconductors, the vortex core is filled by normal metallic electrons. However, a number of different experimental probes, including neutron scattering, muon spin resonance (μSR), and nuclear magnetic resonance (NMR), have shown that vortex cores in the high-T_c cuprates are antiferromagnetic rather than normal metallic.[1] This phenomenon has been observed in almost all high-T_c materials, including LSCO, YBCO, TBCO, and NSCO; thus it appears to be a universal property of the high-T_c cuprates.

High-T_c superconducting materials also have highly unusual transport properties. While conventional metals have a T^2 dependence of resistivity, in accordance with the predictions of the Fermi-liquid theory, the high-T_c materials display a linear T dependence of the resistivity near optimal doping. This dependence extends over a wide temperature window and seems to be universal among the cuprates. When the underdoped or sometimes optimally doped SC state is destroyed by applying a high magnetic field, the resulting "normal state" is not a conventional conducting state (Ando *et al.*, 1995, 1996; Boebinger *et al.*, 1996; Hill *et al.*, 2001) but exhibits insulatorlike behavior, at least along the c axis, i.e., the axis perpendicular to the CuO_2 planes. This phenomenon may be related to the insulating AF vortices mentioned in the previous paragraph.

The high-T_c materials attracted great attention because of their high SC transition temperatures. However, many of the striking properties discussed above are also shared by other materials, which have a similar phase diagram but typically much reduced temperature and energy scales. The 2D organic superconductor κ-(BEDT-TTF)$_2X$ (X=anion) displays a similar phase diagram in the temperature versus pressure plane, where a direct first-order transition between AF and SC phases can be tuned by pressure or magnetic field (Lefebvre *et al.*, 2000; Singleton and Mielke, 2002; Taniguchi *et al.*, 2003). In this system, the AF transition temperature is approximately $T_N \sim 30$ K, while the SC transition temperature is $T_c \sim 14$ K. In heavy-fermion compounds like $CeCu_2(Si_{1-x}Ge_x)_2$ (Kitaoka *et al.*, 2001), $CePd_2Si_2$, and $CeIn_3$ (Mathur *et al.*, 1998), the SC phase also appears near the boundary to the AF phase. In all these systems, even though the underlying solid-state chemistries are rather different, the resulting phase diagrams are strikingly similar and robust. This similarity suggests that the overall features of all these phase diagrams are controlled by a single energy scale. Different classes of materials differ only by this overall energy scale. Another interesting example of competing antiferromagnetism and superconductivity is that of quasi-one-dimensional Bechgaard salts. The best studied material from this family, $(TMTSF)_2PF_6$, is an AF insulator at ambient pressure and becomes a triplet superconductor above a certain critical pressure (Jerome *et al.*, 1980; Lee *et al.*, 1997, 2003; Vuletic *et al.*, 2002).

The discovery of high-T_c superconductivity has greatly stimulated the theoretical understanding of superconductivity in strongly correlated systems. Since the theoretical literature is extensive, the readers are referred to a number of excellent reviews and representative articles.[2] The present review article focuses on a particular theory, which unifies the AF and SC phases of the high-T_c cuprates based on an approximate $SO(5)$ symmetry (Zhang, 1997). The $SO(5)$ theory draws its inspiration from the successful application of symmetry principles in theoretical physics. All fundamental laws of Nature are statements about symmetry. Conservation of energy, momentum, and charge are direct consequences of global symmetries. The forms of the fundamental interactions are dictated by local gauge symmetries. Symmetry unifies apparently different physical phenomena into a common framework. For example, electricity and magnetism were discovered independently and viewed as completely different phenomena before the 19th Century. Maxwell's theory and the underlying relativistic symmetry between space and time unified the electric field $\vec{E}$ and the magnetic field $\vec{B}$ into a common electromagnetic-field tensor $F_{\mu\nu}$. This unification shows that electricity and magnetism share a common microscopic origin and can be transformed into each other by going to different inertial frames. As discussed in the Introduction, the two robust and universal ordered phases of the high-temperature superconductor are the AF and SC phases. The central question in this field concerns the transition from one phase to the other as the doping level is varied.

The $SO(5)$ theory unifies the three-dimensional AF order parameter (N_x, N_y, N_z) and the two-dimensional SC order parameter $(\mathrm{Re}\,\Delta, \mathrm{Im}\,\Delta)$ into a single, five-dimensional order parameter called the *superspin*, in a way similar to the unification of electricity and magnetism in Maxwell's theory:

$$F_{\mu\nu} = \begin{pmatrix} 0 & & & & \\ E_x & 0 & & & \\ E_y & B_z & 0 & & \\ E_z & -B_y & B_x & 0 & \end{pmatrix} \Leftrightarrow n_a = \begin{pmatrix} \mathrm{Re}\Delta \\ N_x \\ N_y \\ N_z \\ \mathrm{Im}\Delta \end{pmatrix}. \qquad (1)$$

[1] See, for example, Katano *et al.*, 2000; Lake *et al.*, 2001, 2002; Mitrovic *et al.*, 2001, 2003; Khaykovich *et al.*, 2002; Levi, 2002; Miller *et al.*, 2002; Fujita *et al.*, 2003; Kakuyanagi *et al.*, 2003; Kang *et al.*, 2003.

[2] Among them are Inui *et al.*, 1988; Schrieffer *et al.*, 1989; Dagotto, 1994; Scalapino, 1995; Wen and Lee, 1996; Anderson, 1997; Balents *et al.*, 1998; Varma, 1999; Zaanen, 1999b; Abrikosov, 2000; Chakravarty *et al.*, 2001; Senthil and Fisher, 2001; Carlson *et al.*, 2002; Franz, Tesanovic, and Vafek, 2002; Ioffe and Millis, 2002; Laughlin, 2002; Sachdev, 2002a; Shen *et al.*, 2002; Anderson *et al.*, 2003; Chubukov *et al.*, 2003; Norman and Pepin, 2003; Manske *et al.*, 2003; Fu *et al.*, 2004.

This unification relies on the postulate that a common microscopic interaction is responsible for both AF and SC phases in the high-T_c cuprates and related materials. A well-defined $SO(5)$ transformation rotates one form of the order into another. Within this framework, the mysterious transition from the AF to SC phase as a function of doping is explained in terms of a rotation in the five-dimensional order-parameter space. Symmetry principles are not only fundamental and beautiful, they are also practically useful in extracting information from a strongly interacting system that can be tested quantitatively. As can be seen in the examples, applying the isospin $SU(2)$ and the $SU(3)$ symmetries to the strong interaction allows one to make and test some quantitative predictions even when the symmetry is broken. The approximate $SO(5)$ symmetry between the AF and SC phases has many direct consequences, which can be tested both numerically and experimentally. We shall discuss a number of these tests in this review article.

Historically, the $SO(5)$ theory concentrated on the competition between AF and SC orders in the high-T_c cuprates. The idea of some order competing with superconductivity is common in several theories. Staggered flux or a d-density-wave phase has been suggested (Affleck and Marston, 1988; Wen and Lee, 1996; Chakravarty *et al.*, 2001), the spin-Peierls order has been discussed (Vojta and Sachdev, 1999; Park and Sachdev, 2001), and spin- and charge-density-wave orders have been considered (Zaanen, 1990a; Kivelson *et al.*, 2001; Zhang *et al.*, 2002). The $SO(5)$ theory extends simple consideration of the competition between AF and SC phases in the cuprates by unifying the two order parameters using a larger symmetry and examining the consequences of such symmetry.

The microscopic interactions in the high-T_c materials are highly complex, and the resulting phenomenology is extremely rich. The $SO(5)$ theory is motivated by a confluence of the phenomenological top-down approach with the microscopic bottom-up approach, as discussed below.

A. The top-down approach

Upon first glance at the phase diagram of the high-T_c cuprates, one is immediately impressed by its striking simplicity; there are only three universal phases in this diagram: the AF, the SC, and the metallic phases, all with homogeneous charge distributions. However, closer inspection reveals a bewildering complexity of other possible phases, which may not be universally present in all high-T_c cuprates and which may have inhomogeneous charge distributions. Because of this complexity, formulating a universal theory of high-T_c superconductivity is a formidable challenge. The strategy of the $SO(5)$ theory can be best explained with an analogy: we see a colorful world around us, but the entire rainbow of colors is composed of only three primary colors. In the $SO(5)$ theory, the superspin plays the role of the primary colors.

A central macroscopic hypothesis of the $SO(5)$ theory is that the ground state and the dynamics of collective excitations in various phases of the high-T_c cuprates can be described in terms of the spatial and temporal variations of the superspin. This is a highly constraining and experimentally testable hypothesis, since it excludes many possible phases. It does include a homogeneous state in which AF and SC phases coexist microscopically. It includes states with spin and charge-density-wave orders, such as striped phases, checkerboards, and AF vortex cores, which can be obtained from spatial modulations of the superspin. It also includes quantum-disordered ground states and Cooper-pair density waves, which can be obtained from the temporal modulation of the superspin. The metallic Fermi-liquid state on the overdoped side of the high-T_c superconductivity phase diagram seems to share the same symmetry as the high-temperature phase of the underdoped cuprates. Therefore they can also be identified with the disordered state of the superspin, although extra care must be given in that case to treat the gapless fermionic excitations. If this hypothesis is experimentally proven to be correct, a great simplicity emerges from the complexity: a full dynamical theory of the superspin field can be the universal theory of the high-T_c cuprates. Part of this review article is devoted to describing and classifying phases that can be obtained from this theory. This top-down approach focuses on the low-energy collective degrees of freedom and takes as its starting point a theory expressed exclusively in terms of these collective degrees of freedom. This is to be contrasted with the conventional approach based on weak-coupling Fermi-liquid theory, of which the BCS theory is a highly successful example. For an extensive discussion on the relative merits of both approaches for the problem of high-T_c superconductivity, we refer the reader to an excellent recent review article by Carlson *et al.* (2002).

The $SO(5)$ theory is philosophically inspired by the Landau-Ginzburg theory, a highly successful phenomenological theory, in which one first makes observations of the phase diagram, then introduces one order parameter for each broken symmetry phase and constructs a free-energy functional by expanding in terms of different order parameters (a review of earlier work based on this approach is given by Vonsovsky *et al.*, 1982). However, given the complexity of interactions and phases in the cuprates, introducing one order parameter for each phase with unconstrained parameters would greatly compromise the predictive power of the theory. The $SO(5)$ theory extends the Landau-Ginzburg theory in several important directions. First, it postulates an approximately symmetric interaction potential between the AF and the SC phases in the underdoped regime of the cuprates, thereby greatly constraining theoretical model building. Second, it includes a full set of dynamic variables canonically conjugate to the superspin order parameters, including the total spin, the total charge, and the so-called π operators. Therefore, unlike the

classical Landau-Ginzburg theory, which only contains the classical order-parameter fields without their dynamically conjugate variables, the $SO(5)$ theory is capable of describing quantum-disordered phases and the quantum phase transitions between these phases. Because the quantum-disordered phases are described by the degrees of freedom canonically conjugate to the classical order parameters, a definite relationship, the so-called $SO(5)$ orthogonality relation, exists between them, which can give highly constrained theoretical predictions. Therefore, in this sense, the $SO(5)$ theory makes great use of the Landau-Ginzburg theory but also goes far beyond it in making more constrained and more powerful predictions that are subject to experimental falsification.

B. The bottom-up approach

Soon after the discovery of the high-T_c cuprates, Anderson (1987) introduced the repulsive Hubbard model to describe the electronic degrees of freedom in the CuO_2 plane. Its low-energy limit, the t-J model, is defined by (Zhang and Rice, 1988)

$$H = -t \sum_{\langle x,x' \rangle} c_\sigma^\dagger(x) c_\sigma(x') + J \sum_{\langle x,x' \rangle} \vec{S}(x) \cdot \vec{S}(x'), \tag{2}$$

where the t term describes the hopping of an electron with spin σ from a site x' to its nearest neighbor x, with double occupancy removed, and the J term describes the nearest-neighbor spin-exchange interaction. The main merit of these models does not lie in their microscopic accuracy or realism but rather in their conceptual simplicity. However, despite their simplicity, these models are still very hard to solve, and their phase diagram cannot be compared directly with experiments.

The t-J model certainly contains an AF phase at half filling. While it is still not fully settled whether it has a d-wave SC ground state with a high transition temperature (Pryadko *et al.*, 2003), it is reasonably convincing that it has strong d-wave pairing fluctuations (Sorella *et al.*, 2002). Therefore it is plausible that a small modification could give a robust SC ground state. The basic microscopic hypothesis of the $SO(5)$ theory is that AF and SC states arise from the same interaction with a common energy scale of J. This common energy scale justifies the treatment of antiferromagnetism and superconductivity on an equal footing and is also the origin of an approximate $SO(5)$ symmetry between these two phases. By postulating an approximate symmetry between the AF and SC phases, and by systematically testing this hypothesis experimentally and numerically, one should be able to resolve the question of the microscopic mechanism of high-T_c superconductivity. In this context, early numerical diagonalizations showed that the low-lying states of the t-J model fit into irreducible representations of the $SO(5)$ symmetry group (Eder *et al.*, 1998). If the $SO(5)$ symmetry is valid, then high-T_c superconductivity shares a common microscopic origin with the antiferromagnetism, which is a well understood phenomenon.

The basic idea is to solve these models by two steps. The first step is a renormalization-group transformation, which maps these microscopic models to an effective superspin model on a plaquette, typically of the size of $2a \times 2a$ or larger. This step determines the form and the parameters of the effective models. The next step is to solve the effective model either through accurate numerical calculations or tractable analytical calculations.

There is a systematic method to carry out the first step. Using the contractor-renormalization-group (CORE; Morningstar and Weinstein, 1996) approach, Altman and Auerbach (2002) derived the projected $SO(5)$ model from the Hubbard and t-J models. Within the approximations studied to date, a simple and consistent picture emerges. There are only five low-energy states on a coarse-grained lattice site, namely, a spin-singlet state and a spin-triplet state at half filling and a d-wave hole pair state with two holes. These states correspond exactly to the local and dynamical superspin degrees of freedom hypothesized in the top-down approach. The resulting effective $SO(5)$ superspin model, valid near the underdoped regime, contains only bosonic degrees of freedom. This model can be studied by quantum Monte Carlo simulations up to very large sizes, and the accurate determination of the phase diagram is possible (in contrast to the Hubbard and t-J models) because of the absence of the minus-sign problems. Once the global phase diagrams are determined, fermionic excitations in each phase can also be studied by approximate analytic methods. Within this approach, the effective $SO(5)$ superspin model derived from the microscopic physics can give a realistic description of the phenomenology and phase diagram of the high-T_c cuprates and account for many of their physical properties (Dorneich *et al.*, 2002a, 2002b). This agreement can be further tested, refined, and possibly disproved. This approach can be best summarized by the following block diagram:

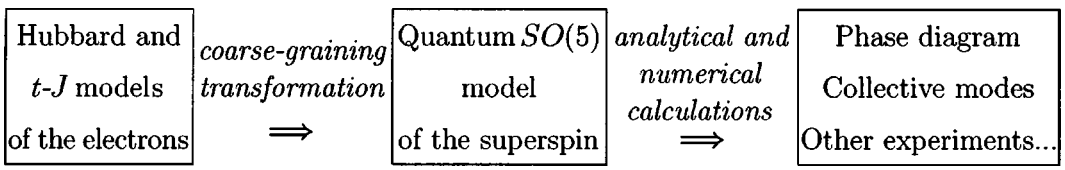

While the practical execution of the first step already introduces errors and uncertainties, we need to remember that the Hubbard and the t-J models are effective models themselves, and they contain errors and uncertainties compared with the real materials. The error involved in our coarse-grain process is not inherently larger than the uncertainties involved in deriving the Hubbard and the t-J models from more realistic models. Therefore, as long as we study a reasonable range of the parameters in the second step and compare them directly with experiments, we can determine these parameters.

This review is intended as a self-contained introduction to a particular theory of the high-T_c cuprates and related materials and is organized as follows. Section II describes three toy models which introduce some important concepts used in the rest of the paper. Section III introduces the concept of the $SO(5)$ superspin and its symmetry transformation, as well as effective dynamical models of the superspin. The global phase diagram of the $SO(5)$ model is discussed and solved numerically in Sec. IV. Section V introduces exact $SO(5)$ symmetric microscopic models, the numerical tests of the $SO(5)$ symmetry in the t-J and Hubbard models, and the Altman-Auerbach procedure of deriving the $SO(5)$ model from microscopic models of the high-T_c cuprates. Section VI discusses the π-resonance model and the microscopic mechanism of high-temperature superconductivity. Finally, in Sec. VII, we discuss experimental predictions of the $SO(5)$ theory and make comparisons with the tests performed so far. The readers are assumed to have a general knowledge of quantum many-body physics and are referred to several excellent textbooks for pedagogical introductions to the basic concepts and theoretical tools (Schrieffer, 1964; Pines and Nozières, 1966; Abrikosov *et al.*, 1993; Auerbach, 1994; Tinkham, 1995; Anderson, 1997; Sachdev, 2000).

II. THE SPIN FLOP AND THE MOTT-INSULATOR-TO-SUPERCONDUCTOR TRANSITION

Before presenting the full $SO(5)$ theory, let us first discuss a much simpler class of toy models, which includes the anisotropic Heisenberg model in a magnetic field, the hard-core lattice boson model, and the negative-U Hubbard model. The low-energy limits of these models are all equivalent to each other and can be described by a universal quantum field theory, the $SO(3)$ quantum nonlinear sigma model. Although these models are simple to solve, they exhibit some of the key properties of the high-T_c cuprates, including strong correlation, competition of different orders, low superfluid density near the insulating phase, maximum of T_c, and the pseudogap behavior.

The spin-1/2 anisotropic AF Heisenberg model on a square lattice is described by the following Hamiltonian:

$$H = \sum_{\langle x,x'\rangle} S^z(x)V(x,x')S^z(x') + J\sum_{\langle x,x'\rangle}[S^x(x)S^x(x) + S^y(x)S^y(x)] - B\sum_x S^z(x). \tag{3}$$

Here, $S^\alpha=\frac{1}{2}\tau^\alpha$ is the Heisenberg spin operator and τ^α is the Pauli matrix. J describes the nearest-neighbor exchange of the xy components of the spin, while $V(x,x')$ describes the z component of the spin interaction. We shall begin by considering only the nearest-neighbor (denoted by $\langle x,x'\rangle$) spin-interaction V. B is an external magnetic field. At the point of $B=0$ and $J=V$, this model enjoys an $SO(3)$ symmetry generated by the total spin operators:

$$S^\alpha = \sum_x S^\alpha(x), \quad [S^\alpha,S^\beta] = i\epsilon_{\alpha\beta\gamma}S^\gamma, \quad [H,S^\alpha]=0. \tag{4}$$

The order parameter in this problem is the Néel operator, which transforms according to the vector representation of the $SO(3)$ group,

$$N^\alpha = \sum_x (-)^x S^\alpha(x), \quad [S^\alpha,N^\beta] = i\epsilon_{\alpha\beta\gamma}N^\gamma. \tag{5}$$

Here $(-)^x=1$ if x is on an even site and $(-)^x=-1$ if x is on an odd site. The symmetry generators and the order parameters are canonically conjugate degrees of freedom, and the second part of Eq. (5) is similar to the Heisenberg commutation relation $[x,p]=i\hbar$ between the canonically conjugate position and momentum. Just as p can be expressed as $(\hbar/i)\partial/\partial x$, one can express

$$S^\alpha = i\epsilon^{\alpha\beta\gamma}N^\beta\frac{\partial}{\partial N^\gamma}, \quad N^\alpha S^\alpha = 0, \tag{6}$$

where the second part of the equation, called the $SO(3)$ *orthogonality relation*, follows directly from the first. The symmetry algebra, the canonical conjugation, and the orthogonality constraint are fundamental concepts important to the understanding of the dynamics and the phase diagram of the model.

Let us first consider the classical, mean-field approximation to the ground state of the anisotropic Heisenberg model defined in Eq. (3). For $V>J$, the spins like to align antiferromagnetically along the z direction. In the Ising phase, $S^z(x)=(-1)^xS$, the ground-state energy per site is given by $e_{\text{Ising}}(B)=-(zV/2)S^2$, where z is the coordination number, which is 4 for the square lattice. Note that the energy is independent of the B field in the Ising phase. For larger values of B, the spins "flop" into the XY plane and tilt uniformly toward the Z axis [see Fig. 2(a)]. Such a spin-flop state is given by $S^z(x)=S\cos\theta$ and $S^x(x)=(-1)^xS\sin\theta$. The minimal energy configuration is given by $\cos\theta=B/zS(V+J)$, and the energy per site for this spin-flop state is $e_{XY}(B)=-zJS^2/2-B^2/2z(V+J)$. Comparing the energies of both states, we obtain the critical value of B where the spin-flop transition occurs: $B_{c1}=zS\sqrt{V^2-J^2}$. On the other hand, we require $|\cos\theta|$

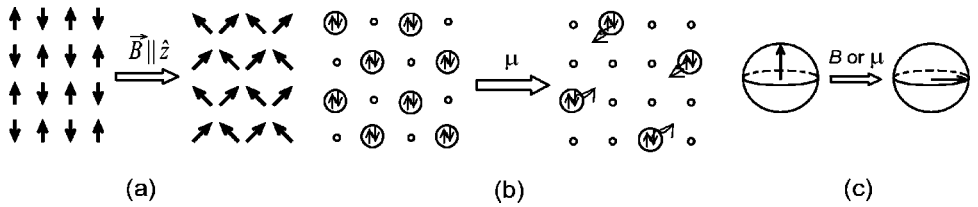

FIG. 2. Spin-flop transition. (a) The spin-flop transition of the XXZ Heisenberg model; (b) the Mott insulator-to-superfluid transition of the hard-core boson model or the $U<0$ Hubbard model. (c) Dscription of both transitions as the spin or the pseudospin flop transition in the $SO(3)$ nonlinear σ model, induced either by the magnetic field or by the chemical potential.

$\leqslant 1$, which implies a critical field $B_{c2}=zS(V+J)$ at which $|\cos\theta|=1$, and the staggered order parameter vanishes. Combining these phase-transition lines, we obtain the *class-B transition* in the ground-state phase diagram depicted in the B-J/V plane [see Fig. 3(a)]. Here and later in the paper, the "class-B" transition refers to the transition induced by the chemical potential or the magnetic field. At the $SO(3)$ symmetric point, $V=J$ and $B_{c1}=0$. For $V<J$, the ground state has XY order even at $B=0$, and there is no spin-flop transition as a function of the magnetic field B. The Ising-to-XY transition can also be tuned by varying J/V at $B=0$, and the phase transition occurs at the special $SO(3)$ symmetric Heisenberg point. This type of transition is also depicted in Fig. 3(a) and will be called the *class-A transition* in this paper.

The spin-1/2 Heisenberg model can be mapped to a hard-core boson model, defined by the following Hamiltonian:

$$H=\sum_{\langle x,x'\rangle} n(x)V(x,x')n(x')-\frac{1}{2}J\sum_{\langle x,x'\rangle}[b^{\dagger}(x)b(x') + \text{H.c.}]-\mu\sum_{x} n(x). \tag{7}$$

Here $b(x)$ and $b^{\dagger}(x)$ are the hard-core boson annihilation and creation operators and $n(x)=b^{\dagger}(x)b(x)$ is the boson density operator. In this context, V, J, and μ describe the interaction, hopping, and the chemical potential energies, respectively. There are two states per site; $|1\rangle$ and $|0\rangle$ denote the filled and empty boson states, respectively. They can be identified with the spin-up $|\uparrow\rangle$ and the spin-down $|\downarrow\rangle$ states of the Heisenberg model. The operators in the two theories can be identified as follows:

$$b(x)^{\dagger}=(-)^{x}[S^{x}(x)+iS^{y}(x)],$$
$$b(x)=(-)^{x}[S^{x}(x)-iS^{y}(x)], \tag{8}$$
$$n(x)=S^{z}(x)+\frac{1}{2}.$$

We see that these two models are identical to each other when $\mu=B+zV/2$. From this mapping, we see that the spin-flop phase diagram has another interpretation: the Ising phase is equivalent to the Mott insulating phase of bosons with a charge-density-wave (CDW) order in the ground state. The XY phase is equivalent to the superfluid phase of the bosons. The two paramagnetic states correspond to the full and empty states of the bosons. While Heisenberg spins are intuitively associated with the $SO(3)$ spin rotational symmetry, lattice boson models generically have only a $U(1)$ symmetry generated by the total number operator $N=\Sigma_x n(x)$, which transforms the boson operators by a phase factor: $b^{\dagger}(x)\rightarrow e^{i\alpha}b^{\dagger}(x)$ and $b(x)\rightarrow e^{-i\alpha}b(x)$. From this point of view, it is rather interesting and nontrivial that the boson model can also have an additional $SO(3)$ symmetry at the special point

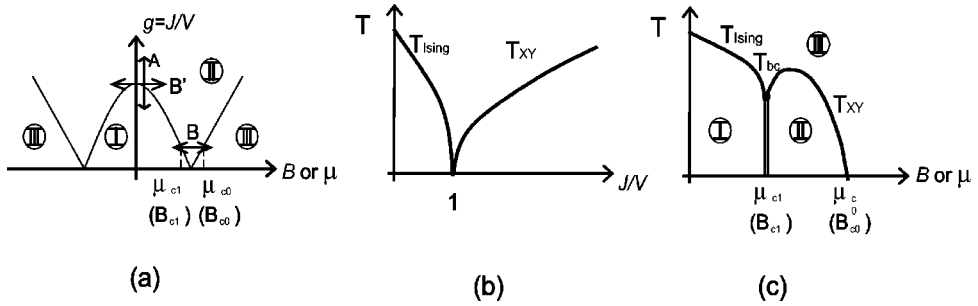

FIG. 3. Systems with competing CDW and superfluid phases: (a) Zero-temperature phase diagram of the XXZ Heisenberg model, the hard-core boson model, or the negative-U Hubbard model. Phase I is the Ising or the charge-density-wave (CDW) phase, phase II is the XY or the superfluid phase, and phase III is the fully polarized or the normal phase. Class-A transition is induced by the anisotropy parameter $g=J/V$, while the class-B transition is induced by the chemical potential or the magnetic field. (b) Finite-temperature phase diagram for the class-A transition in $D=2$. Because of the $SO(3)$ symmetry at $J=V$ point, the transition temperature vanishes according to the Mermin-Wagner theorem. (c) Finite-temperature phase diagram for the class-B transition in $D=3$. T_{bc} denotes the $SO(3)$-symmetric bicritical point.

$J=V$ because of its equivalence to the Heisenberg model.

Having discussed the Heisenberg spin model and the lattice boson models, let us now consider a fermion model, namely, the negative-U Hubbard model, defined by the Hamiltonian

$$H=-t\sum_{\langle x,x'\rangle}[c_\sigma^\dagger(x)c_\sigma(x')+\text{H.c.}]+U\sum_x\left(n_\uparrow(x)-\frac{1}{2}\right)\times\left(n_\downarrow(x)-\frac{1}{2}\right)-\mu\sum_x n_\sigma(x), \tag{9}$$

where $c_\sigma(x)$ is the fermion operator and $n_\sigma(x)=c_\sigma^\dagger(x)c_\sigma(x)$ is the electron density operator at site x with spin σ. Here t, U, and μ are the hopping, interaction, and chemical-potential parameters, respectively. A detailed discussion of the negative-U Hubbard model is given by Micnas *et al.* (1990). The Hubbard model has a pseudospin $SU(2)$ symmetry generated by the operators

$$\eta^-=\sum_x(-)^x c_\uparrow(x)c_\downarrow(x),$$

$$\eta^+=(\eta^-)^\dagger,\ \eta^z=\frac{1}{2}\sum_\sigma\left(n_\sigma(x)-\frac{1}{2}\right), \tag{10}$$

$$[\eta^\alpha,\eta^\beta]=i\epsilon_{\alpha\beta\gamma}\eta^\gamma,$$

where $\eta^\pm=\eta^x\pm i\eta^y$ and $\alpha=x,y,z$, as before. Yang and Zhang (Yang, 1989; Yang and Zhang, 1990; Zhang, 1990) pointed out that these operators commute with the Hubbard Hamiltonian when $\mu=0$ (i.e., $[H,\eta^\alpha]=0$); therefore they form the symmetry generators of the model. Combined with the standard $SU(2)$ spin rotational symmetry, the Hubbard model enjoys a $SO(4)=SU(2)\otimes SU(2)/Z_2$ symmetry. This symmetry has important consequences in the phase diagram and the collective modes in the system. In particular, it implies that the SC and CDW orders are degenerate at half filling. The SC and the CDW order parameters are defined by

$$\Delta^-=\sum_i c_{i\uparrow}c_{i\downarrow},\quad \Delta^+=(\Delta^-)^\dagger,\quad \Delta^z=\frac{1}{2}\sum_{i\sigma}(-1)^i n_{i\sigma},$$

$$[\eta^\alpha,\Delta^\beta]=i\epsilon_{\alpha\beta\gamma}\Delta^\gamma, \tag{11}$$

where $\Delta^\pm=\Delta^x\pm i\Delta^y$. The last equation above shows that the η operators perform the rotation between the SC and CDW order parameters. Thus η^α is the pseudospin generator and Δ^α is the pseudospin order parameter. Just like the total spin and the Néel order parameter in the AF Heisenberg model, they are canonically conjugate variables. Since $[H,\eta^\alpha]=0$ at $\mu=0$, this exact pseudospin symmetry implies the degeneracy of SC and CDW orders at half filling.

The phase diagram of the $U<0$ Hubbard model corresponds to a 1D slice of the 2D phase diagram, as depicted in Fig. 3(a). The exact pseudospin symmetry implies that the class-B transition line for the $U<0$ Hubbard model exactly touches the tip of the Mott lobe, as shown by the B' line in Fig. 3(a). At $\mu=0$, the SC and CDW orders are exactly degenerate, and they can be freely rotated into each other. For $\mu\neq 0$, the system is immediately rotated into the SC state. One can add additional interactions in the Hubbard model, such as a nearest-neighbor repulsion, which breaks the $SU(2)$ pseudospin rotation symmetry even at $\mu=0$. In this case, the pseudospin anisotropy either picks the CDW Mott insulating phase or the SC phase at half filling. By adjusting the nearest-neighbor interaction, one can move the height of the class-B transition line.

We have seen that the hard-core boson model is equivalent to the Heisenberg model because of the mapping (8). The $U<0$ model, on the other hand, is only equivalent to the Heisenberg model in the low-energy limit. In fact, it is equivalent to a $U>0$ Hubbard model at half filling in the presence of a Zeeman magnetic field. The ground state of the half-filled Hubbard model is always AF; therefore its low-energy limit is the same as that of the Heisenberg model in a magnetic field. All three models are constructed from very different microscopic origins. However, they all share the same phase diagram, symmetry group, and low-energy dynamics. In fact, these universal features can all be captured by a single effective quantum-field-theory model, namely, the $SO(3)$ quantum nonlinear σ model. This model can be derived as an effective model from the microscopic models introduced earlier or it can be constructed purely from symmetry principles and the associated operator algebra as defined in Eqs. (4) and (5). The fact that both derivations yield the same model is hardly surprising, since the universal features of all these models are direct consequences of their symmetry.

The $SO(3)$ nonlinear σ model is defined by the following Lagrangian density for a unit vector field n_α with $n_\alpha^2=1$:

$$\mathcal{L}=\frac{\chi}{2}\omega_{\alpha\beta}^2-\frac{\rho}{2}(\partial_i n_\alpha)^2-V(n),$$

$$\omega_{\alpha\beta}=n_\alpha(\partial_t n_\beta-iB_{\beta\gamma}n_\gamma)-(\alpha\leftrightarrow\beta), \tag{12}$$

where the Zeeman magnetic field is given by $B_\alpha=\frac{1}{2}\epsilon_{\alpha\beta\gamma}B_{\beta\gamma}$. Without loss of generality, we pick the magnetic field B to be along the z direction. χ and ρ are the susceptibility and stiffness parameters and $V(n)$ is the anisotropy potential, which can be taken as $V(n)=-(g/2)n_z^2$. Exact $SO(3)$ symmetry is obtained when $g=B=0$. $g>0$ corresponds to easy-axis anisotropy or $J/V<1$ in the Heisenberg model. $g<0$ corresponds to easy-plane anisotropy or $J/V>1$ in the phase diagram of Fig. 3. In the case of $g>0$, there is a phase transition as a function of B. To see this, let us expand the first term in Eq. (12) in the presence of the B field. The time-independent part contributes to an effective potential $V_{\text{eff}}=V(n)-(B^2/2)(n_x^2+n_y^2)$, from which we see that there is a phase transition at $B_{c1}=\sqrt{g/\chi}$. For $B<B_{c1}$, the system is in the Ising phase, while for $B>B_{c1}$ the system is

in the XY phase. Therefore tuning B for a fixed $g>0$ traces out the class-B transition line, as depicted in Fig. 3(a). On the other hand, fixing $B=0$ and varying g traces out the class-A transition line, as depicted in Fig. 3(a). Therefore we see that the $SO(3)$ nonlinear σ model has a phase diagram similar to that of the microscopic models discussed earlier. For a more detailed discussion of phase transitions in $SO(3)$ nonlinear σ models, we refer the reader to an excellent review paper by Auerbach *et al.* (2000).

In $D=2$, both the XY and the Ising phase can have a finite-temperature phase transition into the disordered state. However, because of the Mermin-Wagner theorem, a finite-temperature phase transition is forbidden at the point $B=g=0$, where the system has an enhanced $SO(3)$ symmetry. The finite-temperature phase diagram is shown in Fig. 3(b). Approaching from the SC side, the Kosterlitz-Thouless transition temperature T_{XY} is driven to zero at the Mott to superfluid transition point $J/V=1$. In the 2D XY model, the superfluid density and the transition temperature T_{XY} are related to each other by a universal relationship (Nelson and Kosterlitz, 1977); therefore the vanishing of T_{XY} also implies the vanishing of the superfluid density as one approaches the Mott to superfluid transition. Scalettar *et al.* (1989) and Moreo and Scalapino (1991) have performed extensive quantum Monte Carlo simulations on the negative-U Hubbard model and have indeed concluded that the superfluid density vanishes at the symmetric point. The $SO(3)$ symmetric point leads to a large regime below the mean-field transition temperature in which fluctuations dominate. The single-particle spectral function of the 2D attractive Hubbard model has been studied extensively by Allen *et al.* (1999) near half filling. They identified the pseudogap behavior in the single-particle density of states within this fluctuation regime. Based on this study, they argued that the pseudogap behavior is not only a consequence of the SC phase fluctuations (Doniach and Inui, 1990; Emery and Kivelson, 1995; Uemura, 2002) but also a consequence of the full $SO(3)$ symmetric fluctuations, which also include the fluctuations between the SC and the CDW phases. Figure 3(c) shows the generic finite-temperature phase diagram of these $SO(3)$ models in three dimensions. In this case, the Ising and the XY transition temperatures meet at a single bicritical point T_{bc}, which has the enhanced $SO(3)$ symmetry. At the class-A transition point $g=B=0$, the quantum dynamics is fully $SO(3)$ symmetric. On the other hand, at the class-B transition point $T=T_{bc}$, only the static potential is $SO(3)$ symmetric. We shall return to a detailed discussion of this distinction in Sec. III.C.

The pseudospin $SU(2)$ symmetry of the negative-U Hubbard model has another important consequence. Away from half filling, the η operators no longer commute with the Hamiltonian, but they are eigenoperators of the Hamiltonian, in the sense that

$$[H,\eta^{\pm}]=\mp 2\mu\eta^{\pm}. \tag{13}$$

Thus the η operators create well-defined collective modes in the system. Since they carry charge ± 2, they usually do not couple to any physical probes. However, in a SC state, the SC order parameter mixes the η operators with the CDW operator Δ^z, via Eq. (11). From this reasoning, Zhang (Zhang, 1990, 1991; Demler *et al.*, 1996) predicted a pseudo-Goldstone mode in the density response function at wave vector (π,π) and energy -2μ, which appears only below the SC transition temperature T_c. This prediction anticipated the neutron-resonance mode later discovered in the high-T_c cuprates; a detailed discussion will be given in Sec. VI.

From the toy models discussed in this section, we have learned a few very important concepts. Competition between different orders can sometimes lead to enhanced symmetries at the multicritical point. Universal properties of very different microscopic models can be described by a single quantum field theory constructed from the canonically conjugate symmetry generators and order parameters. The enhanced symmetry naturally leads to a small superfluid density near the Mott transition. The pseudogap behavior in the single-particle spectrum can be attributed to the enhanced symmetry near half filling, and new types of collective Goldstone modes can be predicted from the symmetry argument. All these behaviors are reminiscent of the experimental observations in the high-T_c cuprates. The simplicity of these models on the one hand and the richness of the phenomenology on the other inspired the $SO(5)$ theory, which we shall discuss in the following sections.

III. THE $SO(5)$ GROUP AND EFFECTIVE THEORIES

A. Order parameters and $SO(5)$ group properties

The $SO(3)$ models discussed in the previous section give a nice description of the quantum phase transition from the Mott insulating phase with CDW order to the SC phase. However, these simple models do not have enough complexity to describe the AF insulator at half filling and the d-wave SC order away from half filling. Therefore a natural step is to generalize these models so that the Mott insulating phase with the scalar CDW order parameter is replaced by a Mott insulating phase with the vector AF order parameter. The pseudospin $SO(3)$ symmetry group considered previously arises from the combination of one real scalar component of the CDW order parameter with one complex or two real components of the SC order parameter. After replacing the scalar CDW order parameter by the three components of the AF order parameter and combining them with the two components of the SC order parameters, we are led naturally to consider a five-component order-parameter vector and the $SO(5)$ symmetry group that transforms it.

In Sec. II, we introduced the crucial concepts of the order parameter and symmetry generator. Both of these concepts can be defined locally. In the case of the

Heisenberg AF model, at least two sites, for instance, $\vec{S}_1$ and $\vec{S}_2$, are needed to define the total spin $\vec{S}=\vec{S}_1+\vec{S}_2$ and the Néel vector $\vec{N}=\vec{S}_1-\vec{S}_2$. Similarly, it is simplest to define the concept of the $SO(5)$ symmetry generator and order parameter on two sites with fermion operators c_σ and d_σ, respectively, where $\sigma=1,2$ is the usual spinor index. The AF order-parameter operator can be defined naturally in terms of the difference between the spins of the c and d fermions as follows:

$$N^\alpha=\frac{1}{2}(c^\dagger\tau^\alpha c-d^\dagger\tau^\alpha d),$$
$$n_2\equiv N_1,\quad n_3\equiv N_2,\quad n_4\equiv N_3. \tag{14}$$

In view of the strong on-site repulsion in the cuprate problem, the SC order parameter should be defined on a bond connecting the c and d fermions. We introduce

$$\Delta^\dagger=\frac{-i}{2}c^\dagger\tau^y d^\dagger=\frac{1}{2}(-c_\uparrow^\dagger d_\downarrow^\dagger+c_\downarrow^\dagger d_\uparrow^\dagger),\quad n_1\equiv\frac{(\Delta^\dagger+\Delta)}{2},$$
$$n_5\equiv\frac{(\Delta^\dagger-\Delta)}{2i}. \tag{15}$$

We can group these five components together to form a single vector, $n_a=(n_1,n_2,n_3,n_4,n_5)$, called the *superspin* since it contains both superconducting and antiferromagnetic spin components. The individual components of the superspin are explicitly defined in the last parts of Eqs. (14) and (15).

The concept of the superspin is useful only if there is a natural symmetry group acting on it. In this case, since the order parameter is five dimensional, it is natural to consider the most general rotation in the five-dimensional order-parameter space spanned by n_a. In three dimensions, three Euler angles are needed to specify a general rotation. In higher dimensions, a rotation is specified by selecting a plane and an angle of rotation within this plane. Since there are $n(n-1)/2$ independent planes in n dimensions, the group $SO(n)$ is generated by $n(n-1)/2$ elements, specified in general by antisymmetric matrices $L_{ab}=-L_{ba}$, with $a=1,\ldots,n$. In particular, the $SO(5)$ group has ten generators. The total spin and the total charge operators,

$$S_\alpha=\frac{1}{2}(c^\dagger\tau^\alpha c+d^\dagger\tau^\alpha d),\quad Q=\frac{1}{2}(c^\dagger c+d^\dagger d-2), \tag{16}$$

perform the rotation of the AF and SC order parameters within each subspace. In addition, there are six so-called π operators, first introduced by Demler and Zhang (1995), defined by

$$\pi_\alpha^\dagger=-\frac{1}{2}c^\dagger\tau^\alpha\tau^y d^\dagger,\quad \pi_\alpha=(\pi_\alpha^\dagger)^\dagger. \tag{17}$$

They perform the rotation from AF to SC and vice versa. These infinitesimal rotations are defined by the commutation relations

$$[\pi_\alpha^\dagger,N_\beta]=i\delta_{\alpha\beta}\Delta^\dagger,\quad [\pi_\alpha^\dagger,\Delta]=iN_\alpha. \tag{18}$$

The total spin components S_α, the total charge Q, and the six π operators form the ten generators of the $SO(5)$ group.

The superspin order parameters n_a, the associated $SO(5)$ generators L_{ab}, and their commutation relations can be expressed compactly and elegantly in terms of the $SO(5)$ spinor and the five Dirac Γ matrices. The four-component $SO(5)$ spinor is defined by

$$\Psi_\mu=\begin{pmatrix}c_\sigma\\ d_\sigma^\dagger\end{pmatrix}. \tag{19}$$

They satisfy the usual anticommutation relations

$$\{\Psi_\mu^\dagger,\Psi_\nu\}=\delta_{\mu\nu},\quad \{\Psi_\mu,\Psi_\nu\}=\{\Psi_\mu^\dagger,\Psi_\nu^\dagger\}=0. \tag{20}$$

Using the Ψ spinor and the five Dirac Γ matrices (see Sec. IX.B), we can express n_a and L_{ab} as

$$n_a=\frac{1}{2}\Psi_\mu^\dagger\Gamma_{\mu\nu}^a\Psi_\nu,\quad L_{ab}=-\frac{1}{2}\Psi_\mu^\dagger\Gamma_{\mu\nu}^{ab}\Psi_\nu. \tag{21}$$

The L_{ab} operators form the $SO(5)$ Lie algebra and satisfy the commutation relation

$$[L_{ab},L_{cd}]=-i(\delta_{ac}L_{bd}+\delta_{bd}L_{ac}-\delta_{ad}L_{bc}-\delta_{bc}L_{ad}). \tag{22}$$

The n_a and the Ψ_μ operators form the vector and the spinor representations of the $SO(5)$ group, satisfying the equations

$$[L_{ab},n_c]=-i(\delta_{ac}n_b-\delta_{bc}n_a) \tag{23}$$

and

$$[L_{ab},\Psi_\mu]=-\tfrac{1}{2}\Gamma_{\mu\nu}^{ab}\Psi_\nu. \tag{24}$$

If we arrange the ten operators S_α, Q, and π_α into L_{ab}'s by the matrix form

$$L_{ab}=\begin{pmatrix} 0 & & & & \\ \pi_x^\dagger+\pi_x & 0 & & & \\ \pi_y^\dagger+\pi_y & -S_z & 0 & & \\ \pi_z^\dagger+\pi_z & S_y & -S_x & 0 & \\ Q & \frac{1}{i}(\pi_x^\dagger-\pi_x) & \frac{1}{i}(\pi_y^\dagger-\pi_y) & \frac{1}{i}(\pi_z^\dagger-\pi_z) & 0 \end{pmatrix} \tag{25}$$

and group n_a as in Eqs. (14) and (15), we see that Eqs. (22) and (23) compactly reproduce all the commutation relations presented previously. These equations show that L_{ab} and n_a are the symmetry generators and the order-parameter vectors of the $SO(5)$ theory. The commutation relation Eq. (23) is the $SO(5)$ generalization of the $SO(3)$ communication relation as given in Eqs. (5) and (11).

In systems where the unit cell naturally contains two sites, such as the ladder and bilayer systems, the complete set of operators L_{ab}, n_a, and Ψ_μ can be used to construct model Hamiltonians with the exact $SO(5)$ symmetry, as we shall show in Sec. V.A. In these models, local operators are coupled to each other so that only the total symmetry generators, obtained as the sum of local symmetry generators, commute with the Hamiltonian. For two-dimensional models containing only a single layer, grouping the lattice into clusters of two sites would break lattice translational and rotational symmetry. In this case, it is better to use a cluster of four sites forming a square, which does not break rotational symmetry and can lead naturally to the definition of a d-wave pairing operator (Zhang *et al.*, 1999; Altman and Auerbach, 2002). Then the L_{ab}, n_a, and Ψ_μ operators are interpreted as the effective low-energy operators defined on a plaquette, which forms the basis for an effective low-energy $SO(5)$ theory, rather than the basis of a microscopic $SO(5)$ model.

Having introduced the concept of local symmetry generators and order parameters based in real space, we shall now discuss definitions of these operators in momentum space. The AF and SC order parameters can be naturally expressed in terms of the microscopic fermion operators as

$$N^\alpha=\sum_p c_{p+\Pi}^\dagger \tau^\alpha c_p, \quad \Delta^\dagger=\frac{-i}{2}\sum_p d(p) c_p^\dagger \tau^y c_{-p}^\dagger,$$
$$d(p)\equiv \cos(p_x)-\cos(p_y), \tag{26}$$

where $\Pi\equiv(\pi,\pi)$ and $d(p)$ is the form factor for the d-wave pairing operator in two dimensions. These operators can be combined into the five-component superspin vector n_a by using the same convention as before. The total spin and total charge operators are defined microscopically as

$$S_\alpha=\sum_p c_p^\dagger \tau^\alpha c_p, \quad Q=\frac{1}{2}\sum_p (c_p^\dagger c_p-1), \tag{27}$$

and the π operators can be defined as

$$\pi_\alpha^\dagger=\sum_p g(p) c_{p+\Pi}^\dagger \tau^\alpha \tau^y c_{-p}^\dagger. \tag{28}$$

Here the form factor $g(p)$ needs to be chosen appropriately to satisfy the $SO(5)$ commutation relation (22). In the original formulation of the $SO(5)$ theory, Zhang (1997) chose $g(p)=d(p)$. In this case, the $SO(5)$ symmetry algebra (22) only closes approximately near the Fermi surface. Later, Henley (1998) proposed the choice $g(p)=\mathrm{sgn}[d(p)]$. This construction requires introducing form factors for the AF order parameter, as well. When the momentum-space operators S_α, Q, and $\pi_\alpha^\dagger$, as expressed in Eqs. (27) and (28), are grouped into L_{ab} according to Eq. (25), the symmetry algebra (22) closes exactly. However, the π operators are no longer short ranged.

The $SO(5)$ symmetry generators perform the most general rotation among the five order parameters. The quantum numbers of the π operators exactly make up the difference in quantum numbers between the AF and SC order parameters, as shown in Table I.

With the proper choice of internal form factors, the π operators rotate between the AF and SC order parameters according to Eq. (18). Analogously to the electromagnetic unification presented in the Introduction, the π operators generate an infinitesimal rotation between the AF and SC order parameters similar to the infinitesimal rotation between the electric and magnetic fields generated by the Lorentz transformation. These commutation relations play a central role in the $SO(5)$ theory and have profound implications for the relationship between the AF and SC orders—they provide a basis for unifying these two different types of order in a single framework. In the AF phase, the operator N^α acquires a nonzero expectation value, and the π and SC operators become canonically conjugate variables in the sense of Hamiltonian dynamics. Conversely, in the SC phase the operator Δ acquires a nonzero expectation value, and the π and AF operators become canonically conjugate variables. This canonical relationship is the key to understanding the collective modes in the $SO(5)$ theory and in high-T_c superconductivity.

TABLE I. Quantum numbers of the antiferromagnetic (AF) and the d-wave superconducting (SC) order parameters, and the π operator. Since the π operator rotates the AF and SC order parameters into each other, its quantum numbers make up the difference between the AF and SC order parameters.

	Charge	Spin	Momentum	Internal angular momentum
Δ, $\Delta^\dagger$ or n_1, n_5	± 2	0	0	d wave
N^α or $n_{2,3,4}$	0	1	(π,π)	s wave
π_α, $\pi_\alpha^\dagger$	± 2	1	(π,π)	d wave

The $SO(5)$ group is the minimal group to contain both AF and SC, the two dominant phases in the high-T_c cuprates. However, it is possible to generalize this construction so that it includes other forms of order. For example, Podolsky *et al.* (2004) demonstrated how one can combine AF and triplet SC states using an $SO(4)$ symmetry (Rozhkov and Millis, 2002). Such a construction is useful for quasi-one-dimensional Bechgaard salts, which undergo a transition from an AF insulating state to a triplet SC state as a function of pressure (Jerome *et al.*, 1980; Lee *et al.*, 1997, 2003; Vuletic *et al.*, 2002).

To define an $SO(4)$ symmetry for a one-dimensional electron system, we introduce the total spin, total charge, and Θ operators

$$S_\alpha = \frac{1}{2}\sum_k (c_{+,k}^\dagger \tau^\alpha c_{+,k} + c_{-,k}^\dagger \tau^\alpha c_{-,k}),$$

$$Q = \frac{1}{2}\sum_k (c_{+,k}^\dagger c_{+,k} + c_{-,k}^\dagger c_{-,k} - 2),$$

$$\Theta^\dagger = \frac{-i}{2}\sum_k (c_{+,k}^\dagger \tau^y c_{+,-k}^\dagger - c_{-,k}^\dagger \tau^y c_{-,-k}^\dagger). \tag{29}$$

Here $c_{\pm,k}^\dagger$ creates right- or left-moving electrons of momentum $\pm k_f + k$. The spin operators S_α form an $SO(3)$ algebra of spin rotations given by the second formula of Eq. (4). We can also introduce isospin $SO(3)$ algebra by combining the charge with the Θ operators,

$$I_x = \frac{1}{2}(\Theta^\dagger + \Theta), \quad I_y = \frac{1}{2i}(\Theta^\dagger - \Theta), \quad I_z = Q,$$

$$[I_a, I_b] = i\epsilon_{abc} I_c. \tag{30}$$

Spin and isospin operators together generate an $SO(4) \approx SO(3)\times SO(3)$ symmetry, which unifies triplet superconductivity and antiferromagnetism. We define the Néel vector and the high-T_c order parameter,

$$N_\alpha = \frac{1}{2}\sum_k (c_{+,k}^\dagger \tau^\alpha c_{-,k} + c_{-,k}^\dagger \tau^\alpha c_{+,k}), \tag{31}$$

$$\Psi_\alpha = \frac{1}{i}\sum_k c_{+,k}(\tau^y \tau^\alpha) c_{-,-k},$$

and combine them into a single tensor order parameter

$$\hat{Q} = \begin{pmatrix} (\mathrm{Re}\,\vec{\Psi})_x & (\mathrm{Im}\,\vec{\Psi})_x & N_x \\ (\mathrm{Re}\,\vec{\Psi})_y & (\mathrm{Im}\,\vec{\Psi})_y & N_y \\ (\mathrm{Re}\,\vec{\Psi})_z & (\mathrm{Im}\,\vec{\Psi})_z & N_z \end{pmatrix}. \tag{32}$$

One can easily verify that $Q_{a\alpha}$ transforms as a vector under both spin and isospin rotations,

$$[S_\alpha, Q_{b\beta}] = i\epsilon_{\alpha\beta\gamma} Q_{b\gamma}, \quad [I_a, Q_{b\beta}] = i\epsilon_{abc} Q_{c\beta}. \tag{33}$$

One-dimensional electron systems have been studied extensively using bosonization and renormalization-group analysis. They have a line of phase transitions between an antiferromagnetic and a triplet superconducting phase at a special ratio of the forward- and backward-scattering amplitudes. Podolsky *et al.* (2004) pointed out that anywhere on this line the Θ operator commutes with the Hamiltonian of the system. Hence one finds the $SO(4)$ symmetry at the AF/triplet SC phase boundary without any fine-tuning of the parameters. Consequences of this symmetry for Bechgaard salts are reviewed by Podolsky *et al.* (2004).

Other extensions and generalizations of $SO(5)$ are discussed by Lin *et al.* (1998); Markiewicz and Vaughn (1998); Schulz (1998); Murakami *et al.* (1999); Nayak (2000); and Wu, Guidry, *et al.* (2003).

B. The $SO(5)$ quantum nonlinear σ model

In the previous section, we presented the concepts of local $SO(5)$ order parameters and symmetry generators. These relationships are purely kinematic and do not refer to any particular Hamiltonian. In Sec. V.A, we shall discuss microscopic models with exact $SO(5)$ symmetry, constructed out of these operators. A large class of models, however, may not have $SO(5)$ symmetry at the microscopic level, but their long-distance, low-energy properties may be described in terms of an effective $SO(5)$ model. In Sec. II, we saw that many different microscopic models indeed have the $SO(3)$ nonlinear σ model as their universal low-energy description. Therefore, in order to present a general theory of the AF and SC phases in the high-T_c superconductors, we first introduce the $SO(5)$ quantum nonlinear σ model.

The $SO(5)$ quantum nonlinear σ model describes the kinetic and potential energies of coupled superspin degrees of freedom. In the case of the high-T_c cuprates, the superspin degrees of freedom are most conveniently de-

fined on a coarse-grained lattice, with $2a\times 2a$ lattice spacing in units of the original cuprate lattice spacing, where every supersite denotes a (nonoverlapping) plaquette of the original lattice (see Fig. 29). There are $4^4=256$ states on a plaquette in the original Hubbard model, but we shall retain only the six lowest-energy states, including a spin-singlet state and three spin-triplet states at half filling, and two paired states with two holes or two particles away from half filling (see Fig. 4). In Secs. V.C and V.D, we shall show, with numerical calculations, that these are indeed the lowest-energy states in each charge sector. Additionally, we shall show explicitly that the local superspin degree of freedom discussed in this section can be constructed from these six low-energy states. Proposing the *SO*(5) quantum nonlinear σ model as the low-energy effective model of the high-T_c cuprates requires the following physical assumptions: (i) the AF and SC phases and their quantum-disordered states are the only competing degrees of freedom in the underdoped regime, and (ii) fermionic degrees of freedom are mostly gapped below the pseudogap temperature. For a *d*-wave superconductor, there are also gapless fermion degrees of freedom at the gap nodes. However, they do not play a significant role in determining the phase diagram and collective modes of the system. Our approach is to solve the bosonic part of the model first, and then include gapless fermions self-consistently at a later stage (Demler and Zhang, 1999a; Altman and Auerbach, 2002).

From Eq. (23) and the discussion in Sec. III.A, we see that L_{ab} and n_a are conjugate degrees of freedom, very much similar to $[q,p]=i\hbar$ in quantum mechanics. This suggests that we can construct a Hamiltonian from these conjugate degrees of freedom. The Hamiltonian of the *SO*(5) quantum nonlinear σ model takes the following form:

$$H=\frac{1}{2\chi}\sum_{x,a<b}L_{ab}^2(x)+\frac{\rho}{2}\sum_{\langle x,x'\rangle,a}n_a(x)n_a(x')+\sum_{x,a<b}B_{ab}(x)L_{ab}(x)+\sum_x V(n(x)), \tag{34}$$

where the superspin n_a vector field is subject to the constraint

$$n_a^2=1. \tag{35}$$

This Hamiltonian is quantized by the canonical commutation relations (22) and (23). Here, the first term is the kinetic energy of the *SO*(5) rotors, where χ has the physical interpretation of the moment of inertia of the *SO*(5) rotors. The second term describes the coupling of the *SO*(5) rotors on different sites through the generalized stiffness ρ. The third term introduces the coupling of external fields to the symmetry generators, while $V(n)$ includes anisotropic terms that break the *SO*(5) symmetry to the conventional $SO(3)\times U(1)$ symmetry. The *SO*(5) quantum nonlinear σ model is a natural combination of the *SO*(3) nonlinear σ model, describing the AF Heisenberg model, and the quantum *XY* model, describing the superconductor-to-insulator transition. If we restrict the superspin to having only components $a=2,3,4$, then the first two terms describe the symmetric Heisenberg model, the third term describes the coupling to a uniform external magnetic field, while the last term can represent easy-plane or easy-axis anisotropy of the Néel vector. On the other hand, for $a=1,5$, the first term describes the Coulomb or capacitance energy, the second term is the Josephson coupling energy, while the third term describes coupling to an external chemical potential.

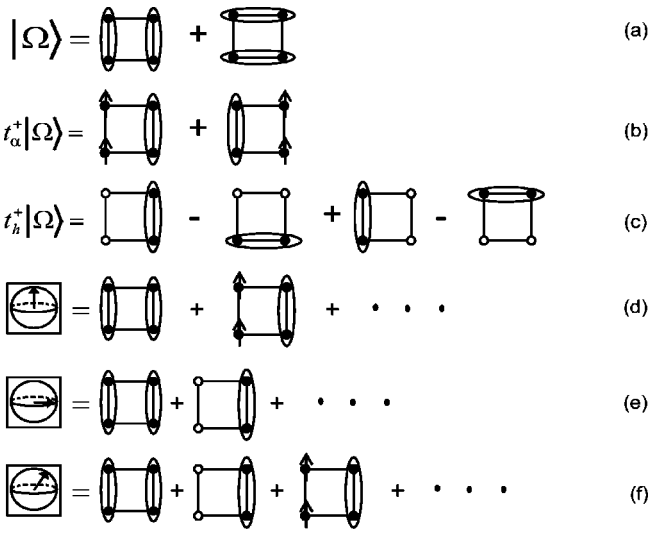

FIG. 4. Hilbert space of the projected *SO*(5) model: (a), (b), and (c) express the five bosonic states of the projected *SO*(5) model in terms of the microscopic states on a plaquette. (d), (e), and (f) represent states with well-defined superspin directions, which can be obtained from the linear combinations of (a), (b), and (c). These states are analytically defined in Eq. (55) and Table II.

The first two terms of the *SO*(5) model describe the competition between quantum disorder and classical order. In the ordered state, the last two terms describe the competition between the AF and SC orders. Let us first consider the quantum competition. The first term prefers sharp eigenstates of the angular momentum. On an isolated site, $C\equiv\Sigma L_{ab}^2$ is the Casimir operator of the *SO*(5) group in the sense that it commutes with all the *SO*(5) generators. The eigenvalues of this operator can be determined completely from group theory—they are 0, 4, 6 and 10, respectively, for the 1-dimensional *SO*(5) singlet, 5-dimensional *SO*(5) vector, 10-dimensional antisymmetric tensor, and 14-dimensional symmetric, traceless tensors, respectively. Therefore we see that this term always prefers a quantum-disordered *SO*(5) singlet ground state, which is also a total spin singlet. When the effective quantum nonlinear σ model is constructed by grouping the sites into plaquettes, the quantum-disordered ground state corresponds to a plaquette resonating valence bond state, as depicted in Figs. 4(a) and 12(a). This ground state is separated from the first excited state, the fivefold *SO*(5) vector state, by an energy

gap of $2/\chi$, which will be reduced when the different $SO(5)$ rotors are coupled to each other by the second term. The second term represents the effect of stiffness, which prefers a fixed direction of the n_a vector to a fixed angular momentum. This competition is an appropriate generalization of the competition between the number-sharp and phase-sharp states in a superconductor and the competition between the classical Néel state and the bond or plaquette singlet state in a Heisenberg antiferromagnet. The quantum phase transition occurs near $\chi\rho \simeq 1$.

In the classically ordered state, the last two anisotropy terms compete to select a ground state. To simplify the discussion, let us first consider the following simple form of the static anisotropy potential:

$$V(n) = -g(n_2^2 + n_3^2 + n_4^2). \tag{36}$$

At the particle-hole symmetric point with vanishing chemical potential $B_{15} = \mu = 0$, the AF ground state is selected by $g > 0$, while the SC ground state is selected by $g < 0$. Here $g = 0$ is the quantum phase-transition point separating the two ordered phases. This phase transition belongs to class A in the classification scheme of Sec. II and is depicted as the $A1$ transition line in Fig. 13. The transition point has the full quantum $SO(5)$ symmetry in the model described above.

It is unlikely that the high-T_c cuprates can be close to this quantum phase-transition point. In fact, we expect the anisotropy term g to be large and positive, making the AF phase strongly favored over the SC phase at half filling. However, the chemical-potential term has the opposite, competing effect and favors superconductivity. We can observe this by transforming the Hamiltonian into the Lagrangian density in the continuum limit,

$$\mathcal{L} = \frac{\chi}{2}\omega_{ab}(x,t)^2 + \frac{\rho}{2}[\partial_k n^a(x,t)]^2 - V[n(x,t)], \tag{37}$$

where

$$\omega_{ab} = n_a(\partial_t n_b - iB_{bc}n_c) - (a \leftrightarrow b) \tag{38}$$

is the angular velocity. We see that the chemical potential enters the Lagrangian as a gauge coupling in the time direction. Expanding the first term in the presence of the chemical potential $\mu = B_{15}$, we obtain an effective potential

$$V_{\text{eff}}(n) = V(n) - \frac{(2\mu)^2\chi}{2}(n_1^2 + n_5^2), \tag{39}$$

from which we see that the bare V term competes with the chemical-potential term. For $\mu < \mu_c = \sqrt{g/\chi}$, the AF ground state is selected, while for $\mu > \mu_c$, the SC ground state is realized. At the transition point—even though each term strongly breaks $SO(5)$ symmetry—the combined term gives an effective static potential that is $SO(5)$ symmetric, as we can see from Eq. (39). This quantum phase transition belongs to class B in the classification scheme of Sec. II. A typical transition of this type is depicted as the $B1$ transition line in Fig. 13. Even though the static potential is $SO(5)$ symmetric, the full quantum dynamics are not. This can be seen most easily from the time-dependent term in the Lagrangian. When we expand the square, the term quadratic in μ enters the effective static potential in Eq. (39). However, there is also a μ-dependent term involving a first-order time derivative. This term breaks the particle-hole symmetry and dominates over the second-order time derivative term in the n_1 and n_5 variables. In the absence of an external magnetic field, only second-order time derivative terms of $n_{2,3,4}$ enter the Lagrangian. Therefore, while the chemical-potential term compensates for the anisotropy potential in Eq. (39) to arrive at an $SO(5)$-symmetric static potential, its time-dependent part breaks the full quantum $SO(5)$ symmetry. This observation leads to the concept of projected or static $SO(5)$ symmetry. A model with projected or static $SO(5)$ symmetry is described by a quantum effective Lagrangian of the form

$$\mathcal{L} = \frac{\chi}{2}\sum_{\alpha=2,3,4}(\partial_t n_\alpha)^2 - \chi\mu(n_1\partial_t n_5 - n_5\partial_t n_1) - V_{\text{eff}}(n), \tag{40}$$

where the static potential V_{eff} is $SO(5)$ symmetric.

We see that a class-A transition from AF to SC occurs at a particle-hole symmetric point, and it can have a full quantum $SO(5)$ symmetry. The class-B transition from AF to SC is induced by a chemical potential; only static $SO(5)$ symmetry can be realized at the transition point. The class-A transition can occur at half filling in organic superconductors, where the charge gap at half filling is comparable to the spin-exchange energy. In this system, the AF-to-SC transition is tuned by pressure, while the doping level and the chemical potential stay fixed. The transition from the half-filled AF state to the SC state in the high-T_c cuprates is far from the class-A transition point, but static $SO(5)$ symmetry can be realized at the chemical-potential-induced transition. However, as we shall see in Sec. IV.B, there are also Mott insulating states with AF order at fractional filling factors, for instance, at doping level $x = 1/8$. The insulating gap is much smaller at these fractional Mott phases, and there is an effective particle-hole symmetry near the tip of the Mott lobes. For these reasons, a class-A transition with the full quantum $SO(5)$ symmetry can be realized again near the tip of fractional Mott phases, as in organic superconductors. Transitions near the fractional Mott insulating lobes are depicted as the $A2$ and $B2$ transitions in the global phase diagram (see Fig. 13). In this case, a transition from a fractional Mott insulating phase with AF order to the SC state can again be tuned by pressure without changing the density or the chemical potential.

The $SO(5)$ quantum nonlinear σ model is constructed from two canonically conjugate field operators L_{ab} and n_a. In fact, there is a kinematic constraint among these field operators. In the case of the Heisenberg model, the total spin operator and the AF Néel order parameter satisfy an orthogonality constraint, as expressed in Eq.

(6). The $SO(5)$ generalization of this constraint can be expressed as

$$L_{ab}n_c + L_{bc}n_a + L_{ca}n_b = 0. \tag{41}$$

This identity is valid for any triples a, b, and c, and can be easily proven by expressing $L_{ab}=n_a p_b - n_b p_a$, where p_a is the conjugate momentum of n_a. Geometrically, this identity expresses the fact that L_{ab} generates a rotation of the n_a vector. The infinitesimal rotation vector lies on the tangent plane of the four-dimensional sphere S^4, as defined by Eq. (35), and is therefore orthogonal to the n_a vector itself. Extending this geometric proof, Wegner (2000) has shown that the $SO(5)$ orthogonality relation also follows physically from maximizing the entropy. Taking the triple a,b,c to be 2, 3, 4, and recognizing that $L_{\alpha\beta}=\epsilon_{\alpha\beta\gamma}S_\gamma$, we find that this identity reduces to the $SO(3)$ orthogonality relation in Eq. (6). This $SO(5)$ identity places a powerful constraint on the expectation values of various operators. In particular, it quantitatively predicts the value of the π order parameter in a mixed state between the AF or SC states. For example, let us take the a,b,c triple to be 1, 2, 5. Equation (41) predicts that

$$L_{15}n_2 + L_{52}n_1 + L_{21}n_5 = 0 \Rightarrow \langle L_{25}\rangle = \langle \mathrm{Im}\ \pi_x\rangle = \frac{Q\langle n_2\rangle}{\langle n_1\rangle}, \tag{42}$$

where we chose the SC phase such that $\langle n_5\rangle = 0$. Here, $Q=\langle L_{15}\rangle$ measures the hole density. Since these four expectation values can easily be measured numerically and, in principle, experimentally, this relationship can be tested quantitatively. Recently, Ghosal, Kallin, and Berlinsky (Ghosal *et al.*, 2002) tested this relationship within microscopic models of the AF vortex core. In this case, AF and SC phases coexist in a finite region near the vortex core, so that both $\langle n_1\rangle$ and $\langle n_5\rangle$ are nonvanishing. They found that the $SO(5)$ orthogonality constraint is accurately satisfied in microscopic models.

In this section, we have presented the $SO(5)$ quantum nonlinear σ model as a heuristic and phenomenological model. The key ingredients of the model are introduced by observing the robust features of the phase diagram and the low-energy collective modes of the high-T_c cuprate system. This is the top-down approach discussed in the Introduction. In this sense, the model has a general validity beyond the underlying microscopic physics. However, it is also useful to derive such a model directly from microscopic electronic models. Fortunately, this bottom-up approach agrees with the phenomenological approach to a large extent. A rigorous derivation of this quantum nonlinear σ model from an $SO(5)$-symmetric microscopic model on a bilayer system will be given in Sec. V.A, while an approximate derivation from the "realistic" microscopic *t-J* and Hubbard models will be given in Sec. V.D.

C. The projected *SO*(5) model with lattice bosons

In the previous section, we presented the formulation of the $SO(5)$ quantum nonlinear σ model. This model is formulated in terms of two sets of canonically conjugate variables—the superspin vector n_a and the angular momentum L_{ab}. The two terms that break the full quantum $SO(5)$ symmetry are the anisotropy term g and the chemical-potential term μ. Therefore this model contains high-energy modes, particularly excitations of the order of the Mott insulating gap at half filling. For this reason, Greiter (1997) and Baskaran and Anderson (1998) questioned whether the effective $SO(5)$ symmetry could be implemented in the low-energy theory. In the previous section, it was shown that these two symmetry-breaking terms could cancel each other in the static potential and the resulting effective potential could still be $SO(5)$ symmetric. It was also pointed out that the chemical-potential term breaks the $SO(5)$ symmetry in the dynamic or time-dependent part of the effective Lagrangian. In response to these observations, Zhang *et al.* constructed the *projected SO*(5) *models* (Zhang *et al.*, 1999), which fully project out the high-energy modes, and obtained a low-energy effective quantum Hamiltonian, with an approximately $SO(5)$-symmetric static potential.

The first step is to perform a transformation from the n_a and L_{ab} coordinates to a set of bosonic operators. We first express the angular momentum operator as

$$L_{ab} = n_a p_b - n_b p_a, \tag{43}$$

where p_a is the canonical momentum conjugate to n_a, satisfying the Heisenberg commutation relation

$$[n_a, p_b] = i\delta_{ab}. \tag{44}$$

Furthermore, we can express the canonical coordinates and momenta in terms of the boson operators as

$$n_a = \frac{1}{\sqrt{2}}(t_a + t_a^\dagger), \quad p_a = \frac{1}{i\sqrt{2}}(t_a - t_a^\dagger), \tag{45}$$

where the boson operators satisfy the commutation relation

$$[t_a, t_b^\dagger] = \delta_{ab}, \tag{46}$$

and the (half filled) ground state is defined by $t_a|\Omega\rangle = 0$. There are five boson operators: $t_\alpha = t_2, t_3, t_4$ are the boson operators for the magnetic triplet excitations, also called the magnons, while

$$t_1 = \frac{1}{\sqrt{2}}(t_h + t_p), \quad t_5 = \frac{1}{i\sqrt{2}}(t_h - t_p) \tag{47}$$

are the linear combinations of the particle pair (t_p) and hole pair (t_h) annihilation operators. In the $SO(5)$ quantum nonlinear σ model formulation, there is an infinite number of bosonic states per site. However, due to the first term in Eq. (34) (the angular momentum term), states with higher angular momenta or, equivalently, higher boson number, are separated by higher energies. Therefore, as far as the low-energy physics is concerned,

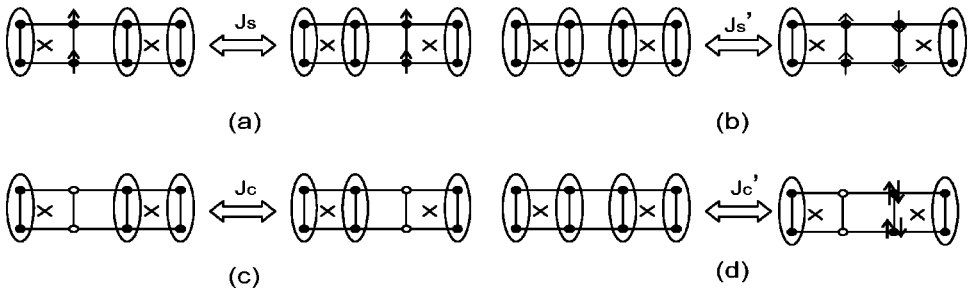

FIG. 5. Illustration of hopping processes of the magnons and the hole pairs on a ladder. The × denotes the center of a plaquette. An ellipse enclosing two sites denotes a spin singlet. (a) J_s describes the magnon hopping; (b) J_s' describes the spontaneous creation and annihilation of a magnon pair; (c) J_c describes the hopping of a hole pair; (d) J_c' describes the spontaneous creation and annihilation of a hole pair and a particle pair. In the full $SO(5)$ model, $J_s=J_s'$ and $J_c=J_c'$. In the projected $SO(5)$ model, the particle pair states are removed and $J_c'=0$.

we can restrict ourselves to the manifold of six states per site, namely, the ground state $|\Omega\rangle$ and the five bosonic states $t_a^\dagger|\Omega\rangle$. This restriction is called the *hard-core boson constraint* and can be implemented by the condition $t_a^\dagger t_b^\dagger|\Omega\rangle=0$. Within the Hilbert space of hard-core bosons, the original $SO(5)$ quantum nonlinear σ model is mapped onto the following hard-core boson model:

$$H=\Delta_s\sum_{x,\alpha=2,3,4} t_\alpha^\dagger t_\alpha(x)+\Delta_c\sum_{x,i=1,5} t_i^\dagger t_i(x)+\mu\sum_x [t_p^\dagger t_p(x) - t_h^\dagger t_h(x)]-J_s\sum_{\langle xx'\rangle} n_\alpha(x)n_\alpha(x')-J_c\sum_{\langle xx'\rangle} n_i(x)n_i(x'), \tag{48}$$

where $\Delta_c=2/\chi-2\mu^2\chi$ and $\Delta_s=2/\chi-g$ are the creation energies for the charge pairs and the triplet magnons, μ is the chemical potential, and J_c and J_s are the exchange energies for SC and AF phases, respectively. In the isotropic case, they are taken to be ρ in the second term of Eq. (34). Expressing n_i and n_α in terms of the bosonic operators, we see that the J_c and J_s terms describe not only the hopping, but also the spontaneous creation and annihilation of the charge pairs and the magnons, as depicted in Fig. 5.

When $\Delta_c=\Delta_s$, $J_c=J_s$, and $\mu=0$, the model (48) has an exact quantum $SO(5)$ symmetry. In this case, the energy to create charge excitations is the same as the energy to create spin excitations. This situation could be realized in organic and heavy-fermion superconductors near the AF phase boundary or in the high-T_c superconductors near commensurate doping fractions such as $x=1/8$, as we shall see in Sec. IV.B. However, for high-T_c systems near half filling, the energy to create charge excitations is much greater than the energy to create spin excitations, i.e., $\Delta_c\gg\Delta_s$. In this case, the full quantum $SO(5)$ symmetry is broken but, remarkably, the effective static potential can still be $SO(5)$ symmetric. This was seen in the previous section by the cancellation of the anisotropy potential g term by the chemical-potential μ term. In a hard-core boson model (48) with $\Delta_c\gg\Delta_s$, a low-energy effective model can be derived by retaining only the hole pair state while projecting out the particle pair state. One imposes the constraint

$$t_p^\dagger(x)|\Omega\rangle=0 \tag{49}$$

at every site x. The projected Hamiltonian takes the form

$$H=\Delta_s\sum_x t_\alpha^\dagger t_\alpha(x)+\tilde{\Delta}_c\sum_x t_h^\dagger t_h(x)-J_s\sum_{\langle xx'\rangle} n_\alpha(x)n_\alpha(x') - J_c\sum_{\langle xx'\rangle} n_i(x)n_i(x'), \tag{50}$$

where $\tilde{\Delta}_c=\Delta_c-\mu$. The Hamiltonian (50) has no parameters of the order of U. To achieve the static $SO(5)$ symmetry, we need $\Delta_s\sim\tilde{\Delta}_c$ and $J_s\sim J_c$. The first condition can always be met by changing the chemical potential, whereas the second one requires certain fine tuning. However, as we shall discuss in Sec. V.D (see Fig. 31), this condition emerges naturally when one derives the model (50) from the Hubbard model in the relevant regime of parameters.

The form of the projected $SO(5)$ Hamiltonian hardly changes from the unprojected model (48), but the definition of n_1 and n_5 is changed from

$$n_1=\frac{1}{\sqrt{2}}(t_1+t_1^\dagger)=\frac{1}{2}(t_h+t_p+t_h^\dagger+t_p^\dagger),$$

$$n_5=\frac{1}{\sqrt{2}}(t_5+t_5^\dagger)=\frac{1}{2i}(t_h-t_p-t_h^\dagger+t_p^\dagger) \tag{51}$$

to

$$n_1=\frac{1}{2}(t_h+t_h^\dagger),\quad n_5=\frac{1}{2i}(t_h-t_h^\dagger). \tag{52}$$

From Eq. (51), we see that n_1 and n_5 commute with each other before the projection. However, after the projection, they acquire a nontrivial commutation relation, as can be seen from Eq. (52):

$$[n_1,n_5]=i/2. \tag{53}$$

Therefore the projecting out of doubly occupied sites, commonly referred to as the *Gutzwiller projection*, can be analytically implemented in the $SO(5)$ theory by re-

taining the form of the Hamiltonian and changing only the commutation relations.

The Gutzwiller projection implemented through the modified commutation relations between n_1 and n_5 is formally similar to projection onto the lowest Landau level in the physics of the quantum Hall effect. For electrons moving in a 2D plane, the canonical description involves two coordinates, X and Y, and two momenta, P_X and P_Y. However, if the motion of the electron is fully confined in the lowest Landau level, the projected coordinate operators become noncommuting and are given by $[X,Y]=il_0^2$, where l_0 is the magnetic length. In the context of the projected $SO(5)$ Hamiltonian, the original rotors at a given site can be viewed as particles moving on a four-dimensional sphere S^4, as defined by Eq. (35), embedded in a five-dimensional Euclidean space. The angular momentum term $(1/2\chi)L_{ab}^2$ describes the kinetic motion of the particle on the sphere. The chemical potential acts as a fictitious magnetic field in the (n_1,n_5) plane. In the Gutzwiller-Hubbard limit, where $\Delta_c \gg \Delta_s$, a large chemical-potential term is required to reach the limit $\tilde{\Delta}_c \sim \Delta_s$. The particle motion in the (n_1,n_5) plane becomes quantized in this limit, as in the case of the quantum Hall effect, and the noncommutativity of the coordinates (n_1,n_5) given by Eq. (53) arises as a result of the projection. The projection does not affect the symmetry of the sphere on which the particle is moving; however, it restricts the sense of the kinetic motion to be chiral, i.e., only along one direction in the (n_1,n_5) plane (see Fig. 6). In this sense, the particle is moving on a *chiral* $SO(5)$-symmetric sphere. The noncommutativity of the (n_1,n_5) coordinates is equivalent to the effective Lagrangian [see Eq. (40) of Sec. III.B] containing only the first-order time derivative. In fact, from Eq. (40), we see that in this case the canonical momenta associated with the coordinates n_1 and n_5 are given by

$$p_1 = \frac{\delta L}{\delta \dot{n}_1} = \chi \mu n_5, \quad p_5 = \frac{\delta L}{\delta \dot{n}_5} = -\chi \mu n_1. \tag{54}$$

Applying the standard Heisenberg commutation relation for the conjugate pairs (n_1,p_1) or (n_5,p_5) gives exactly the quantization condition (53). Note that in Eq. (54) $\chi\mu$ plays the role of Planck's constant in quantum mechanics. We see that the projected $SO(5)$ Hamiltonian (50) subjected to the quantization condition (53) is fully equivalent to the effective Lagrangian (40) discussed in the last section.

Despite its apparent simplicity, the projected $SO(5)$ lattice model can describe many complex phases, most of which are seen in the high-T_c cuprates. These different phases can be described in terms of different limits of a single variational wave function of the following product form:

$$|\Psi\rangle = \prod_x \{\cos\theta(x) + \sin\theta(x)[m_\alpha(x)t_\alpha^\dagger(x) + \Delta(x)t_h^\dagger(x)]\} \times |\Omega\rangle, \tag{55}$$

where the variational parameters $m_\alpha(x)$ should be real,

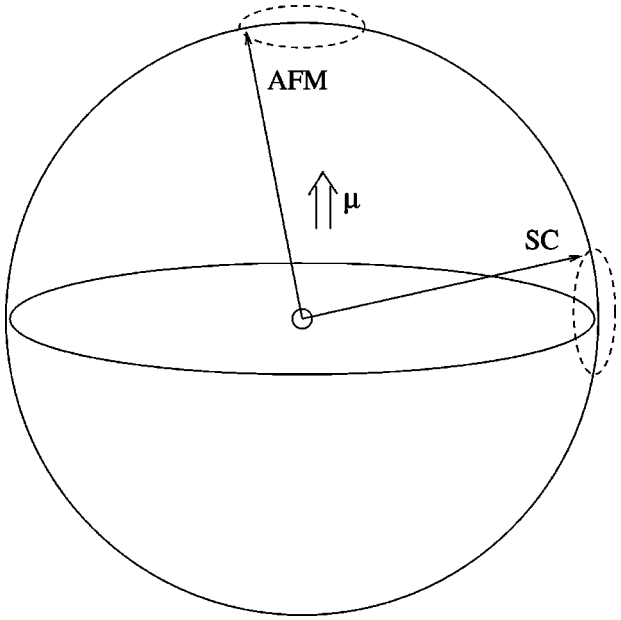

FIG. 6. The chiral $SO(5)$ sphere. This sphere has an $SO(5)$-symmetric shape but allows only one sense of the rotation in the SC plane (n_1,n_5). Small oscillations around the equator, or the π triplet resonance, are unaffected by the chiral projection. However, small oscillations around the north pole, or the π doublet mode, are strongly affected: only one of the two such modes is retained after the projection.

while $\Delta(x)$ is generally complex. The normalization of the wave function, $\langle\Psi|\Psi\rangle=1$, requires the variational parameters to satisfy

$$\sum_\alpha |m_\alpha(x)|^2 + |\Delta(x)|^2 = 1. \tag{56}$$

We can therefore parametrize them as $|m_\alpha(x)|^2 = \cos^2\phi(x)$ and $|\Delta(x)|^2 = \sin^2\phi(x)$, which is similar to the $SO(5)$ constraint introduced in Eq. (35). The expectation values of the order parameters and the symmetry generators in this variational state are given by

$$\langle\Psi|n_\alpha(x)|\Psi\rangle = \frac{1}{\sqrt{2}}\sin 2\theta(x)\,\mathrm{Re}[m_\alpha(x)],$$

$$\langle\Psi|n_1(x)|\Psi\rangle = \frac{1}{2}\sin 2\theta(x)\,\mathrm{Re}[\Delta(x)],$$

$$\langle\Psi|n_5(x)|\Psi\rangle = \frac{1}{2}\sin 2\theta(x)\,\mathrm{Im}[\Delta(x)], \tag{57}$$

and

$$\langle\Psi|Q(x)|\Psi\rangle = \langle\Psi|t_h^\dagger(x)t_h(x)|\Psi\rangle = \sin^2\theta(x)|\Delta(x)|^2,$$

$$\langle\Psi|S_\alpha|\Psi\rangle = -\langle\Psi|i\epsilon^{\alpha\beta\gamma}t_\beta^\dagger(x)t_\gamma(x)|\Psi\rangle = -i\epsilon^{\alpha\beta\gamma}\sin^2\theta m_\beta^*(x)m_\gamma(x),$$

TABLE II. Physical properties of various plaquette states classified according to the $SO(5)$ order parameters and symmetry generators.

		Charge Q	Spin S	AF order $\langle n_\alpha \rangle$	SC order $\langle n_i \rangle$	π order $\langle \pi_\alpha \rangle$
(a)	Resonating valence bond state: $\sin\theta=0$	0	0	0	0	0
(b)	Magnon state: $\cos\theta=0$ and $\sin\phi=0$	0	1	0	0	0
(c)	Hole-pair state: $\cos\theta=0$ and $\cos\phi=0$	–2	0	0	0	0
(d)	AF state: $0<\sin\theta<1$ and $\sin\phi=0$	0	indefinite	$\neq 0$	0	0
(e)	SC state: $0<\sin\theta<1$ and $\cos\phi=0$	indefinite	0	0	$\neq 0$	0
(f)	Mixed AF/SC state: $0<\sin\theta<1$ and $0<\sin\phi<0$	indefinite	indefinite	$\neq 0$	$\neq 0$	$\neq 0$
(g)	π state: $\cos\theta=0$ and $0<\cos\phi<1$	indefinite	indefinite	0	0	$\neq 0$

$$\langle\Psi|\pi_\alpha(x)|\Psi\rangle = \langle\Psi|\frac{t_\alpha^\dagger(x)t_h(x)}{i\sqrt{2}}|\Psi\rangle = \frac{\sin^2\theta m_\alpha^*(x)\Delta(x)}{i\sqrt{2}}. \tag{58}$$

Initially, we restrict our discussion to the case in which the variational parameters are uniform, describing a translationally invariant state. Evaluating different physical operators in this state gives the results summarized in Table II.

As we can see, this wave function not only describes classically ordered states with spontaneously broken symmetry, but also quantum-disordered states which are eigenstates of spin and charge. Generally, Δ_c and Δ_s favor quantum-disordered states, while J_c and J_s favor classically ordered states. Depending on the relative strength of these parameters, a rich phase diagram can be obtained.

The phase diagram of the projected $SO(5)$ model with $J_c=2J_s\equiv J$ is shown in Fig. 7. Changing the chemical potential modifies $\tilde{\Delta}_c$ and traces out a one-dimensional path on the phase diagram. Along this path the system goes from the AF state to the uniform AF/SC mixed phase and then to the SC state. The mixed phase corresponds to only one point on this trajectory (i.e., a single value of the chemical potential μ_c), although it covers a whole range of densities $0<\rho<\rho_c$. This suggests that the transition may be thought of as a first-order transition between the AF and SC phases, with a jump in the density at μ_c. The spectrum of collective excitations shown in Fig. 8, however, shows that this phase diagram also has important features of two second-order phase transitions. The energy gap to $S=1$ excitations inside the SC phase vanishes when the chemical potential reaches the critical value μ_c. Such a softening should not occur for the first-order transition but is required for a continuous transition into a state with broken spin symmetry. This shows that models with the $SO(5)$ symmetry have intrinsic fine tuning to be exactly at the border between a single first-order transition and two second-order transitions; in subsequent sections this type of transition will be classified as a type-1.5 transition. Further discussion of the phase diagram of the projected $SO(5)$ model is given in Sec. V.C. Note that effective bosonic Hamiltonians similar to Eq. (50) have also been considered by van Duin and Zaanen (2000) and Park and Sachdev (2001).

IV. THE GLOBAL PHASE DIAGRAM OF $SO(5)$ MODELS

A. Phase diagram of the classical model

The two robust ordered phases in the high-T_c cuprates are the AF phase at half filling and the SC phase away from half filling. It is important to ask how these two phases are connected in the global phase diagram as different tuning parameters, such as temperature, doping level, external magnetic field, etc., are varied. Analyzing the $SO(5)$ quantum nonlinear σ model, Zhang has classified four generic types of phase diagrams, presented as Figs. (1A)–(1D) in Zhang (1997). In the next section we are going to investigate the zero-temperature phase diagram in which the AF and the SC phases are connected by various quantum-disordered states, often possessing charge order. In this section, we first focus on the simplest possibility, in which AF and SC are the only two competing phases in the problem, and discuss the phase diagram in the plane of temperature and chemical potential, or doping level.

Let us first discuss the general properties of the transition between two phases, each characterized by its own order parameter. In particular, we shall focus on the phenomenon of enhanced symmetry at the multicritical point, at which physically different static correlation functions show identical asymptotic behavior. In the case of the CDW-to-SC transition discussed in Sec. II, the CDW is characterized by an Ising-like Z_2 order parameter, while the SC is characterized by a $U(1)$ order parameter. In the case of AF-to-SC transition, the order-parameter symmetries are $SO(3)$ and $U(1)$, respectively. Generically, the phase transition between two ordered phases can be either a single direct first-order transition or two second-order phase transitions with a uniform mixed phase in between, in which both order parameters are nonzero. This situation can be understood easily by describing the competition in terms of a Landau-Ginzburg functional of two competing order parameters (Kosterlitz *et al.*, 1976), which is given by

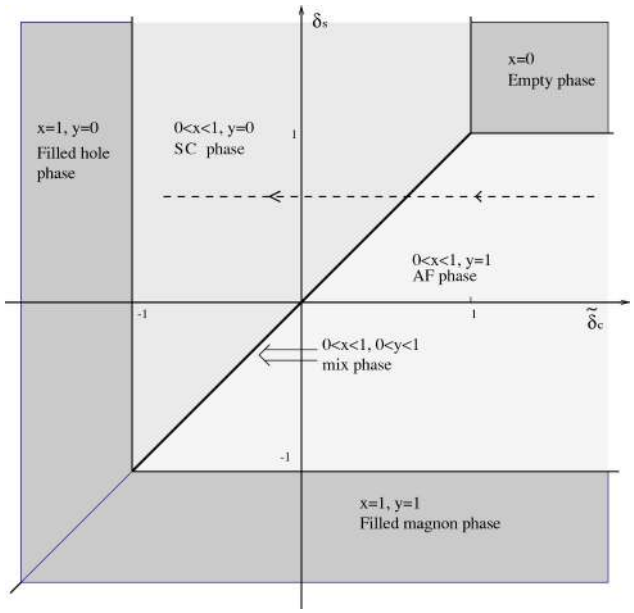

FIG. 7. Phase diagram of the projected $SO(5)$ model (50) (for the case $J_c=2J_s\equiv J$) as a function of $\delta_s=\Delta_S/4J$ and $\tilde{\delta}_c=\tilde{\Delta}_c/4J$. Variation of the chemical potential changes $\tilde{\Delta}_c$ and traces out a one-dimensional trajectory as shown by the dotted line. $x=\sin^2\theta$ and $y=\cos^2\phi$.

$$F=r_1\phi_1^2+r_2\phi_2^2+u_1\phi_1^4+u_2\phi_2^4+2u_{12}\phi_1^2\phi_2^2. \tag{59}$$

Here, ϕ_1 and ϕ_2 are vector order parameters with N_1 and N_2 components, respectively. In the case of current interest, $N_1=2$ and $N_2=3$ and we can view $\phi_1^2=n_1^2+n_5^2$ as the SC component of the superspin vector, and $\phi_2^2=n_2^2+n_3^2+n_4^2$ as the AF component of the superspin vector. These order parameters are determined by minimizing the free energy F, and are given by the solutions of

$$2u_1\phi_1^2+2u_{12}\phi_2^2+r_1=0,\quad 2u_{12}\phi_1^2+2u_2\phi_2^2+r_2=0. \tag{60}$$

These equations determine the order parameters uniquely, except in the case when the determinant of the linear equations vanishes. At the point when

$$u_1u_2=u_{12}^2 \tag{61}$$

and

$$\frac{r_1}{\sqrt{u_1}}=\frac{r_2}{\sqrt{u_2}}, \tag{62}$$

the order parameters satisfy the relation

$$\frac{\phi_1^2}{\sqrt{u_2}}+\frac{\phi_2^2}{\sqrt{u_1}}=\text{const}, \tag{63}$$

but they are not individually determined. In fact, with the rescaling $\tilde{\phi}_1^2=\phi_1^2/\sqrt{u_2}$ and $\tilde{\phi}_2^2=\phi_2^2/\sqrt{u_1}$, the free energy is exactly $SO(5)$ symmetric with respect to the scaled variables, and Eq. (63) becomes identical to Eq. (35) in the $SO(5)$ case. Since the free energy depends only on the combination $\tilde{\phi}_2^1+\tilde{\phi}_2^2$, one order parameter can be smoothly rotated into the other without any energy cost. Equation (61) is the most important condition for the enhanced symmetry. We shall discuss extensively in this paper whether this condition is satisfied microscopically or close to some multicritical points in the high-T_c cuprates. On the other hand, Eq. (62) can always be tuned. In the case of the AF-to-SC transition, the chemical potential couples to the square of the SC order

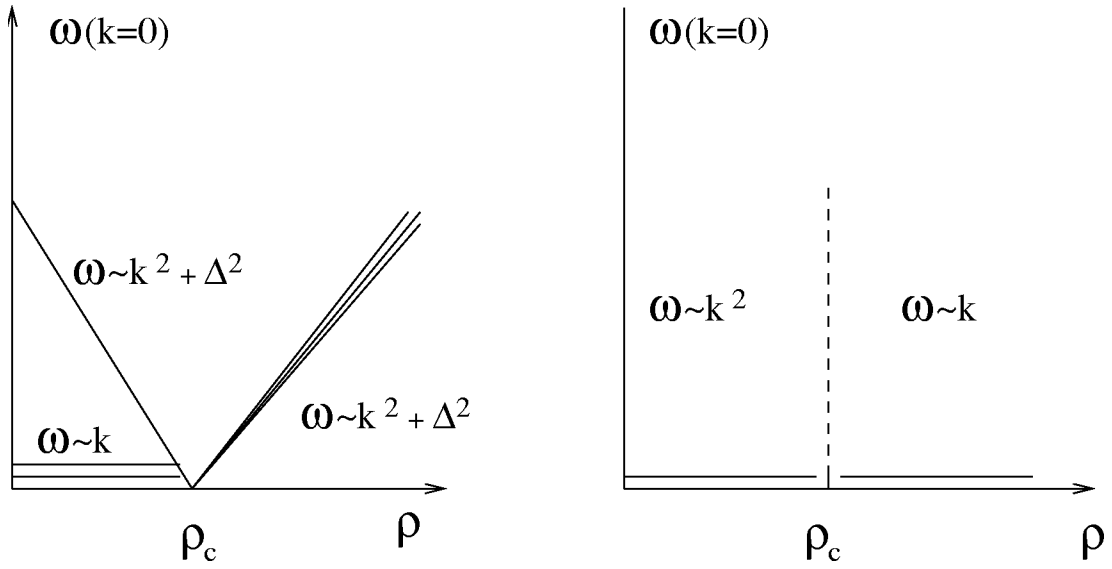

FIG. 8. Spectra of the collective excitations of the projected $SO(5)$ model as a function of density. The region $0<\rho<\rho_c$ corresponds to the uniform mixed phase of superconductivity (SC) and antiferromagnetism (AF). Region $\rho>\rho_c$ corresponds to the SC phase. The left panel shows the spectra of the spin excitations. For $\rho<\rho_c$, there are two gapless spin-wave modes and one gapped spin-amplitude mode. For $\rho>\rho_c$, there is a spin-triplet π-resonance mode. The right panel shows the spectra of the gapless charge excitations (in the absence of long-range interactions). For $\rho<\rho_c$ the charge mode has quadratic dispersion. The dispersion relation changes from $\omega\propto k^2$ to $\omega\propto k$ for the $\rho>\rho_c$ regime.

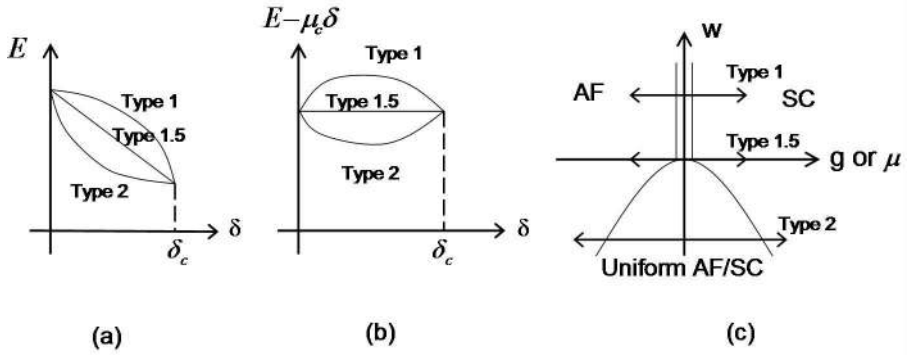

FIG. 9. The three types of phase state in the *SO*(5) model: The energy (a) and the free energy (b) can depend on the density of a uniform AF/SC mixed state with a negative curvature when $u_{12}>\sqrt{u_1u_2}$ (classified as type 1) or a positive curvature when $u_{12}<\sqrt{u_1u_2}$ (classified as type 2). The *SO*(5)-symmetric limiting case of zero curvature, classified as type 1.5, is realized when $u_{12}=\sqrt{u_1u_2}$. (c) The type-1 phase transition from the AF to SC state is a direct first-order transition. There are two second-order transitions from the AF to SC state in the type-2 case. *SO*(5) symmetry is realized at the intermediate case of type 1.5.

parameter, as we can see from Eq. (39). Therefore r_1 can be tuned by the chemical potential, and Eq. (62) defines the critical value of the chemical potential μ_c at which the phase transition between AF and SC occurs. At this point, the chemical potential is held fixed, but the SC order parameter and the charge density can change continuously according to Eq. (63). Since the free energy is independent of the density at this point, the energy, which differs from the grand canonical free energy by a chemical-potential term $\mu\delta$, can depend only *linearly* on the density. The linear dependence of the energy on doping is a very special, limiting case. Generally, the energy-versus-doping curve would either have a negative curvature, classified as type 1, or a positive curvature, classified as type 2 [see Fig. 9(a)]. The special limiting case of "type 1.5" with zero curvature is only realized at the *SO*(5)-symmetric point. The linear dependence of the ground-state energy of a uniform AF/SC mixed state on the density is a crucial test of the *SO*(5) symmetry, which can be performed numerically, as we shall see in Secs. V.B and V.C. The constancy of the chemical potential and the constancy of the length of the *SO*(5) superspin vector (63) as a function of density can be tested experimentally as well, as we shall discuss in Sec. V.B.

The constancy of the chemical potential as a function of the density in a uniform system is a very special situation which only follows from the enhanced symmetry at the phase-transition point. In a system with phase separation, the chemical potential is also independent of the total density, but the local density is nonuniform. The two phases are generally separated by a domain wall. The *SO*(5)-symmetric case can be obtained from the phase separation case in the limit where the width of the domain wall goes to infinity and a uniform state is obtained. This situation can be studied analytically by solving Eq. (60). Defining the parameters that characterize the deviation from the symmetric point as $w=u_{12}-\sqrt{u_1u_2}$ and $g=(r_1/\sqrt{u_1}-r_2/\sqrt{u_2})/2$, it is obvious that the phase transition between the two forms of order is tuned by g, while w determines the nature of the phase transition. The phase diagram in the (g,w) plane is shown in Fig. 9(c). For $w>0$, the two ordered phases are separated by a first-order line. This type of transition is classified as type 1. On the other hand, when $w<0$, the two ordered phases are separated by two second-order phase-transition lines with an intermediate mixed phase where two orders coexist, i.e., $\langle\phi_1\rangle\neq 0$ and $\langle\phi_2\rangle\neq 0$. This type of transition is classified as type 2. The limiting "type 1.5" behavior corresponds to the symmetric point $w=0$. Approaching this point from $w>0$, the first-order transition becomes weaker and weaker and the latent heat associated with the first-order transition becomes smaller and smaller. Therefore the symmetric point can be viewed as the end point of a first-order transition. On the other hand, approaching the symmetric point from $w<0$, the width of the intermediate mixed phase becomes smaller and smaller, until the two second-order transition lines merge into a single transition at $w=0$. From the above discussion, we learn an important lesson: the phase transition between two ordered phases can be either a direct first-order transition or two second-order transitions with an intermediate mixed phase. Furthermore, the symmetric point realizes a limiting behavior which separates these two scenarios. Balents, Fisher, and Nayak (1998) and Lee and Kivelson (2003) pointed out that the type-1 and type-2 transitions of a Mott insulator induced by varying the chemical potential are analogous to the two types of superconductor-to-normal-state transitions induced by a magnetic field. The magnetic field induces a direct first-order transition from the SC state to the normal state in type-1 superconductors, while it induces two second-order transitions with an intermediate mixed state in the type-2 superconductors. Indeed, the limiting "type-1.5" behavior separating the type-1 and the type-2 superconductors also has a special symmetry, in which Bogomol'nyi's bound for the vortex is satisfied as an

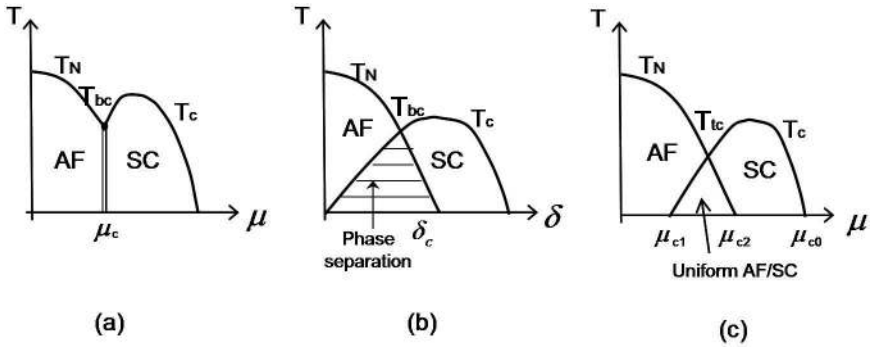

FIG. 10. The finite-temperature phase diagram in $D=3$ for the class-B1 transition shown in Fig. 13. (a) Direct first-order phase transition between AF and SC, as a function of the chemical potential; (b) first-order AF-to-SC transition as a function of doping, classified as the type-1 transition; (c) two second-order phase transitions with a uniform AF/SC mix phase in between, classified as a type-2 transition. The AF and SC transition temperatures T_N and T_c merge into either a bicritical T_{bc} or a tetracritical point T_{tc}.

equality. We note that recent work of Senthil *et al.* discussed an alternative scenario for a direct second-order transition between two phases with different order parameters and without a higher symmetry at the transition point. This was achieved by having fractionalized excitations at the quantum critical point (Senthil *et al.*, 2004).

Let us now turn to the finite-temperature phase transitions. In $D=3$, finite-temperature phase transitions associated with continuous symmetry breaking are possible. The order parameters ϕ_1 and ϕ_2 can therefore each have their own phase-transition temperatures, T_c and T_N. The interesting question is how these two second-order lines merge as one changes the parameter g or, equivalently, the chemical potential μ, which interchanges the relative stability of the two ordered phases. There are two generic possibilities. The type-1 phase diagram is shown in Fig. 10(a), where the two second-order phase-transition lines intersect at a bicritical point, T_{bc}, which is also the termination point of the first-order transition line separating the two ordered phases. This type of phase diagram is realized for $u_{12}>\sqrt{u_1u_2}$. The first-order transition at μ_c separates the AF and SC states with different densities; therefore the T-vs-δ phase diagram shown in Fig. 10(b) contains a region of phase separation extending over the doping range $0<\delta<\delta_c$. The type-2 phase diagram is shown in Fig. 10(c), where T_c and T_N intersect at a tetracritical point, below which a uniform AF/SC mixed phase separates the two pure phases by two second-order transition lines. This type of phase diagram is realized for $u_{12}<\sqrt{u_1u_2}$.

In contrast to the conventional superconductors with a long coherence length, the high-T_c cuprates have a short coherence length and a large Ginzburg region. Thus one has the possibility of observing nontrivial critical behaviors. An interesting point concerns the symmetry at the multicritical point where T_N and T_c (or, more generally, T_1 and T_2) intersect. At the multicritical point defined by $r_1=r_2=0$, the critical fluctuations of the order parameters couple to each other and renormalize the coefficients of the fourth-order terms u_1, u_2, and u_{12}. There are several possible fixed points. The *symmetric fixed point*, also known as the Heisenberg fixed point, is characterized by $u_1^*=u_2^*=u_{12}^*$. The $O(N_1)\times O(N_2)$ symmetry is enhanced at this point to the higher $O(N_1+N_2)$ symmetry. Another fixed point, called the *biconical tetracritical* point in the literature, has nonvanishing values of u_1^*, u_2^*, and u_{12}^* at the fixed point, which deviates from the $O(N_1+N_2)$ symmetry. The third possible fixed point is the *decoupled fixed point*, where $u_{12}^*=0$ and the two order parameters decouple from each other.

The relative stability of these three fixed points can be studied analytically and numerically. The general picture is that there are two critical values, N_c and N_c'. For $N_1+N_2<N_c$, the symmetric bicritical point is stable, for $N_c<N_1+N_2<N_c'$, the biconical point is stable, while for $N_1+N_2>N_c'$, the decoupled point becomes stable. Renormalization-group (RG) calculations based on the $4-\epsilon$ expansion (Kosterlitz *et al.*, 1976) place the value of N_c close to 4 and the value of N_c' close to 11. The RG flow diagram is shown in Fig. 11 for the cases of $N_1=3$ and $N_2=2$. Initially, all RG trajectories flow towards the symmetric fixed point. The manner in which the trajectories diverge close to the symmetric point depends on the values of the initial parameters. The trajectories flow to the symmetric point when $u_{12}^2=u_1u_2$, they flow to the biconical point when $u_{12}^2<u_1u_2$, and they flow outside of the regime of weak-coupling RG analysis when $u_{12}^2>u_1u_2$. In the case of competition between AF and SC, $N=N_1+N_2=5$ is very close to N_c, leading to two important consequences. First, the biconical point breaks the $SO(5)$ symmetry weakly. The value of the interaction parameters at the biconical fixed point is given by $(u_1^*;u_2^*;u_{12}^*)=2\pi^2\epsilon(0.0905;0.0847;0.0536)$. Extrapolating to $\epsilon=1$ gives the root-mean-square deviation from the symmetric $SO(5)$ point to about 26%, indicating weak $SO(5)$ symmetry breaking. The second consequence is that the critical exponent associated with the flow away from the symmetric $SO(5)$ point is extremely slow. The first loop $4-\epsilon$ expansion gives the value of $1/13$ for the exponent associated with the flow away from the symmetric point. To get an estimate of the order of magnitude, we take the initial value of the scaling

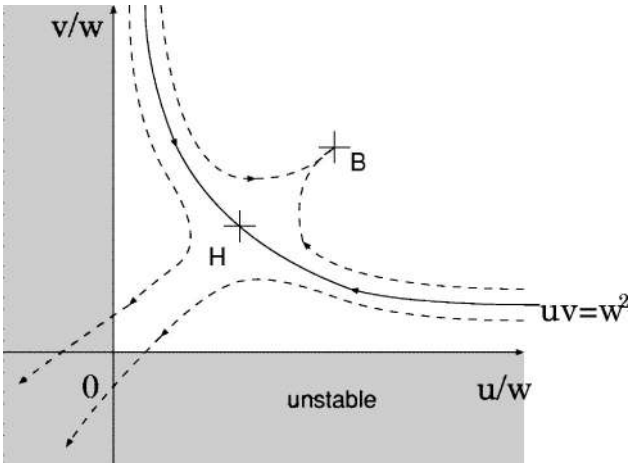

FIG. 11. Renormalization-group flow in the $(u_1/u_{12}, u_2/u_{12})$ plane. (In this figure, $u=u_1$, $v=u_2$ and $w=u_{12}$.) The renormalization-group flow is initially attracted towards the symmetric Heisenberg point labeled by H. The RG trajectories diverge near the Heisenberg model, with a very small exponent. From Murakami and Nagaosa, 2000.

variable taking the flow away from the $SO(5)$ fixed point to be 0.04. This value is obtained by considering the quantum corrections associated with a projected $SO(5)$ model (Arrigoni and Hanke, 2000). In this case, a significant deviation away from the symmetric point can only be observed when the reduced temperature is $t=(T-T_{bc})/T_{bc}\approx 10^{-11}$, making the departure from the $SO(5)$-symmetric point practically unobservable. Indeed, numerical simulations of the $SO(5)$ models presented in Sec. IV.C are consistent with $SO(5)$-symmetric behavior over a wide range of temperatures and in very large systems. However, it should be noted that these models do not prove the ultimate stability of the symmetric point.

The question of the stability of the $SO(5)$-symmetric bicritical point has been raised and discussed extensively in the literature (Burgess *et al.*, 1998; Arrigoni and Hanke, 2000; Hu and Zhang, 2000; Murakami and Nagaosa, 2000; Hu, 2001; Aharony, 2002; Calabrese *et al.*, 2003; Jöstingmeier *et al.*, 2003). Because the possible flow away from the bicritical point is extremely slow, experimental and numerical observation of the $SO(5)$-symmetric bicritical behavior should be possible over a wide range of temperatures, if the starting microscopic parameters are already close to the symmetric point $u_{12}=\sqrt{u_1u_2}$. The $SO(5)$-symmetric bicritical point has a distinct set of critical exponents, summarized by Hu and Zhang (2000), which can be distinguished experimentally from the usual $SO(3)$ and $U(1)$ behavior. In this sense, the experimental observation of the bicritical behavior would demonstrate that the microscopic model of the high-T_c cuprates is close to the $SO(5)$ symmetry. In Sec. VII.D we shall discuss the analysis of Murakami and Nagaosa (2000) showing bicritical scaling behavior in the κ-BEDT organic superconductors. If the microscopic parameters are far from the symmetric point $u_{12}=\sqrt{u_1u_2}$, other critical behaviors could be observed. Aharony (2002) proposed the decoupled tetracritical fixed point with $u_{12}^*=0$. As previously discussed, this critical point can be observed in experiments only if the microscopic value of u_{12}^* is already close to zero (due to the extremely slow flows of parameters). For the high-T_c cuprates, the AF vortex core experiments discussed in Sec. VII.A clearly show that the AF and SC order parameters are strongly and repulsively coupled with $u_{12}^*>0$. Therefore the decoupled fixed point is unlikely to be relevant for these materials. However, this behavior could be realized in some heavy-fermion systems where different bands are responsible for the AF and SC phases separately. Kivelson *et al.* (2001) and Calabrese *et al.* (2003) also considered the possibility of tricritical points, where some of the quartic terms u_1, u_2, u_{12} become negative and the sixth-order terms become important. In this case, the phase diagram could have topologies different from those listed here. The reader is referred to the more extensive discussions of Kivelson *et al.* (2001), especially Figs. 1(c) and 1(d) of that reference. Negative values of the quartic coefficient in the free-energy equation (59) may come from the runaway flows shown in Fig. 11. A multicritical point most closely related to the bicritical point is the biconical tetracritical point. Its relevance to the high-T_c cuprates has been discussed by Zhang (1997; Zhang *et al.*, 2002).

B. Phase diagram of the quantum model

Having discussed the finite-temperature phase diagram of the classical model, we now present the global phase diagram of the quantum model at zero temperature. The quantum phase transitions in the $SO(5)$ model were discussed in Figs. (1C) and (1D) of the article of Zhang (1997). The quantum critical behavior of the $SO(5)$ models has also been studied extensively by Zaleski and Kopec (2000a, 2000b) and Kopec and Zaleski (2001, 2003). This section extends the original analysis to include quantum-disordered states with inhomogeneous charge distributions. The analysis carried out in this section is based on the bosonic projected $SO(5)$ model, which bears great similarities to the phase diagrams of the hard-core boson model studied extensively in the literature (Fisher *et al.*, 1989; Bruder *et al.*, 1993; Scalettar *et al.*, 1995; van Otterlo *et al.*, 1995; Pich and Frey, 1998; Bernardet *et al.*, 2002; Hebert *et al.*, 2002). The iterative construction of the global phase diagram of the $SO(5)$ model is also inspired by the global phase diagram of the quantum Hall effect constructed by Kivelson, Lee, and Zhang (1992).

The projected $SO(5)$ model given in Eq. (50) contains the creation energy and the hopping process of the magnons and hole pairs. The variational wave function for this model has the general form given in Eq. (55), with variational parameters $\theta(x)$, $m_\alpha(x)$, and $\Delta(x)=m_1(x)+im_5(x)$. The expectation value of the energy in this state is given by

$$\langle\Psi|H|\Psi\rangle = E(\theta(x), m_a(x))$$
$$= -\frac{J_s}{2}\sum_{xx';\alpha=2,3,4}\sin 2\theta(x)\sin 2\theta(x')m_\alpha(x)m_\alpha(x')$$
$$-\frac{J_c}{4}\sum_{xx';i=1,5}\sin 2\theta(x)\sin 2\theta(x')m_i(x)m_i(x')$$
$$+\Delta_s\sum_{x;\alpha=2,3,4}\sin^2\theta(x)m_\alpha^2(x)$$
$$+\tilde{\Delta}_c\sum_{x;i=1,5}\sin^2\theta(x)m_i^2(x). \quad (64)$$

The variational minimum is taken with respect to the normalization condition (56). In the regime when the quantum fluctuations are small, $\theta(x)$ can be taken to be fixed and uniform. In this case, the variational energy is nothing but the energy functional of a classical, generally anisotropic $SO(5)$ rotor model, which has been studied extensively numerically (Hu, 2001). At the point $J_c = 2J_s$ and $\tilde{\Delta}_c = \Delta_s$ in parameter space, this rotor model is $SO(5)$ symmetric at the classical level. However, unlike the classical $SO(5)$ rotor, the projected $SO(5)$ model also contains quantum fluctuations and quantum-disordered phases. The phase diagram of the projected $SO(5)$ model has been studied extensively by quantum Monte Carlo simulations (Dorneich *et al.*, 2002b; Riera, 2002a, 2002b; Chen, Capponi, *et al.*, 2003; Jöstingmeier *et al.*, 2003), and the results will be reviewed in detail in Sec. IV.C. When the quantum fluctuations are not strong enough to destroy classical order, the general topology of the phase diagram is similar to that classified in Sec. IV.A.

In this section, we discuss the regime in which quantum fluctuations are non-negligible and focus on the global phase diagram when classical order competes with quantum disorder and uniform states compete with nonuniform states. In Fig. 4 and Table II, we see that the classically ordered states are obtained from the linear superpositions of quantum-disordered states. The quantum-disordered states are realized in the regime where the kinetic energy of the superspins Δ_s and Δ_c overwhelm the coupling energy of the superspins J_s and J_c, and the superspin vector becomes disordered in the temporal domain. In this sense, the quantum description of the superspin goes far beyond the classical Landau-Ginzburg theory discussed in the previous section.

By arranging the six elementary states from Fig. 4 into spatially nonuniform patterns, we have infinitely many possibilities. In addition to the classically ordered AF and SC states, in Fig. 12 we illustrate some of the basic nonuniform states and their associated wave functions, expressed in terms of $\theta(x)$, $m_\alpha(x)$, and $\Delta(x)$. Striped order was theoretically predicted and experimentally observed in the high-T_c cuprates (Zaanen and Gunnarsson, 1989; Tranquada *et al.*, 1995; Kivelson *et al.*, 1998; White and Scalapino, 1998). In a typical striped phase, a magnetic stripe of width $2a$ is separated by a charge stripe of width $2a$, where a is the lattice constant. The stripe state comes in two forms. For in-phase stripes, both the charge and the spin periodicity are $4a$ in the direction transverse to the stripe direction. For out-of-phase stripes, the charge periodicity is $4a$, while the spin periodicity is $8a$. A charge stripe can either be insulating or superconducting. The SC stripes are defined by their phase angle; the two nearby SC stripes can be either in or out of phase. The case when both the insulasting and the SC stripes are out of phase can be viewed as a *superspin spiral*, in which the superspin direction rotates continuously along the direction transverse to the stripes. [See Fig. 12(c).] Both types of stripes discussed here have both AF and SC orders. Another possibility is the checkerboard pair density wave (PDW; Chen *et al.*, 2002), depicted in Fig. 12(d). It can be obtained from the in-phase stripe by quantum-disordering the hole pairs in the SC stripe. This state is insulating with AF and charge orders. We stress that all insulating states in the $SO(5)$ theory are obtained from the quantum-disordered states of the hole pairs. Therefore they are paired insulators, in contrast to ordinary band insulators or a Wigner crystal state of the electrons.

Some of the inhomogeneous states observed in the high-T_c cuprates can be described naturally in terms of the temporal and spatial ordering of the superspin. The key question is how they are energetically stabilized in the projected $SO(5)$ model. These spatially nonuniform states are usually realized when extended interactions are considered, which take the form

$$H_{ext} = \left(V_c\sum_{\langle xx'\rangle} + V_c'\sum_{\langle\langle xx'\rangle\rangle}\right)n_h(x)n_h(x')$$
$$+\left(V_s(S_T)\sum_{\langle xx'\rangle} + V_s'(S_T)\sum_{\langle\langle xx'\rangle\rangle}\right)$$
$$\times\sum_{S_T=0,1,2}[t^\dagger(x)t^\dagger(x')]_{S_T}[t(x)t(x')]_{S_T}$$
$$+J_\pi\sum_{\langle xx'\rangle}[t_\alpha^\dagger(x)t_\alpha(x')t_h^\dagger(x')t_h(x) + \text{H.c.}]$$
$$+V_\pi\sum_{\langle xx'\rangle}[n_h(x)n_t(x') + n_h(x')n_t(x)] + \cdots. \quad (65)$$

Here $\langle xx'\rangle$ and $\langle\langle xx'\rangle\rangle$ denote the summation over the nearest neighbor and the next-nearest neighbor on a square lattice. $[t(x)t(x')]_{S_T}$ refers to the total spin $S_T = 0,1,2$ combinations of two magnons on sites $\langle xx'\rangle$. The V_c and V_c' terms describe the interaction of the hole pairs, the V_s and V_s' terms describe the interaction of the magnons, and the J_π and V_π terms describe the mutual interaction of the hole pair and the magnon. Since the projected $SO(5)$ model is defined on a coarse-grained lattice, the density of the hole pairs, n_h, is related to the hole-doping density by $n_h = 2\delta$. The model Hamiltonian given by $H + H_{ext}$ has been studied extensively by Chen, Capponi, *et al.* (2003) by using both quantum Monte Carlo methods and mean-field theory. Here we summarize the basic qualitative results. In order to study the phase diagram of this model, we first focus on the charge

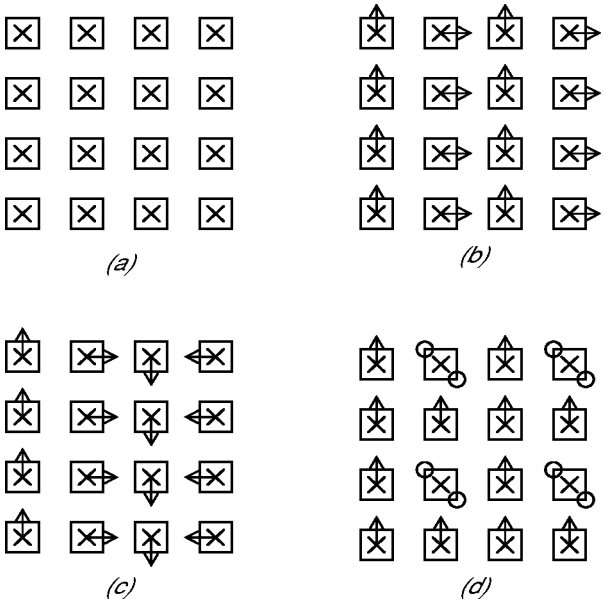

FIG. 12. Some possible ground states of the projected $SO(5)$ model (see also Fig. 4). The $\times$ depicts a resonating-valence-bond (RVB) -like spin-singlet state on a plaquette, the arrow denotes the direction of the superspin, and the open circles depict hole pairs. (a) A plaquette RVB state, described by $\theta(x)=0$ on every plaquette; (b) an in-phase SC stripe with $\alpha(x)=0,\pi/2,0,\pi/2$, on each stripe; (c) a superspin spiral with $\alpha(x)=0,\pi/2,\pi,3\pi/2$ on each stripe; (d) a hole-pair checkerboard state with $\alpha(x)=0$ everywhere, except on the hole-pair plaquettes, where $\theta=\pi/2$ and $\alpha=\pi/2$.

sector. The charge sector of the projected $SO(5)$ model is the same as the hard-core boson model introduced in Eq. (7) of Sec. II. This model has been much studied in the context of superfluid-to-insulator transition (Bruder *et al.*, 1993; Scalettar *et al.*, 1995; van Otterlo *et al.*, 1995; Pich and Frey, 1998; Bernardet *et al.*, 2002; Hebert *et al.*, 2002). Without the extended interactions $V(x,x')$ in Eq. (3), the phase diagram of the hard-core boson is given in Fig. 3(a). Half filling of the original electron systems in the cuprates corresponds to the vacuum state of the hole pairs, or phase III in Fig. 3(a). The chemical potential μ induces a transition into the SC state, labeled as phase II. Further increase of the chemical potential induces a transition into a checkerboard-ordered state, labeled as phase I. This is the class-B transition shown in Fig. 3(a). Phase I corresponds to $n_h=1/2$ of the hole-pair bosons, or $\delta=1/4$ of the original electrons. When extended interactions in $V(x,x')$ are included, a new insulating phase develops near the overlapping region of phase I and phase III, with boson density of $n_h=1/4$ of the hole-pair bosons, or $\delta=1/8$ of the original electrons [see, for instance, Fig. 2 of Bruder *et al.* (1993)]. This insulating phase can have either striped or checkerboardlike charge order. Generally, the stripe type of insulating order is favored for $V_c' \gg V_c$, and the checkerboard-type order is favored in the opposite limit (Pich and Frey, 1998; Hebert *et al.*, 2002). With even more extended interactions, additional phases develop at lower rational densities. These Mott insulating phases at various rational densities are shown in Fig. 13. The phase boundary between the insulating phases with charge order and the SC phases can be generally classified into types 1, 1.5, and 2, according to the terminology developed in Sec. IV.A and Fig. 9. In the last two cases, a mixed phase, called the *supersolid phase*, develops near the phase boundary. After understanding the generic phase diagram of the hard-core lattice boson model, we are now in a position to discuss the full global phase diagram of the $SO(5)$ model $H+H_{ext}$, depicted in Fig. 13. Here the ordinate denotes the typical ratio of J_c/V_c, but it can obviously be replaced by other similar parameters. The $n_h=0$ phase corresponds to the AF state at half filling, where magnons condense into the singlet ground state. For large values of J/V, a pure SC state is obtained where the hole pairs condense into the singlet ground state. However, besides these two robust, classically ordered phases, we also see new insulating phases at $n_h=1/4$, $n_h=1/8$, and $n_h=3/8$ which correspond to $\delta=1/8$, $\delta=1/16$, and $\delta=3/16$ in the real system. These new insulating states are stabilized by the extended interactions and have both AF and PDW order [see, for example, Fig. 12(d)]. As the chemical potential or the doping level is varied, a given system traces out a one-dimensional slice in this phase diagram, with typical slices $B1$, $B2$, and $B3$ depicted in Fig. 13 (we expect the quantum parameter J/V to be independent of μ for a given family of materials). The nature of the phase transition $B1$ is similar to that of the classical model already discussed in Sec. IV.A. In this case, the phase transition from the AF to SC state can be further classified into types 1, 1.5, and 2, as discussed in Sec. IV.A, with the two latter cases leading to an AF/SC mixed phase at the phase-transition boundary. For lower values of J/V, the trace $B3$ encounters the $\delta=1/8$ insulating phase. The key signature of this type of phase transition is that the SC T_c will display a pronounced minimum as the doping variation traces through the $\delta=1/8$ insulating state. At the same time, the AF ordering [possibly at a wave vector shifted from (π,π)] will show reentrant behavior as doping is varied. The phase transition around the fractional insulating phases can again be classified into types 1, 1.5, and 2, with possible AF/SC, AF/PDW, SC/PDW, and AF/PDW/SC mixed phases.

So far we have classified all quantum phase transitions in the $SO(5)$ models according to two broad classes. Class A describes transitions at a fixed chemical potential, typically at an effectively particle-hole symmetric point. Class B describes transitions in which the chemical potential or the density is varied. Each broad class is further classified into three types, 1, 2, and 1.5, depending on whether the transition is a direct first-order transition, two second-order transitions, or an intermediate symmetric point in between. The full quantum $SO(5)$ symmetry can only be realized in the class-A, type-1.5 quantum phase transition. The Heisenberg point in the hard-core boson problem discussed in Sec. II is one such example. The $g=0$ point in the $SO(5)$ quantum nonlin-

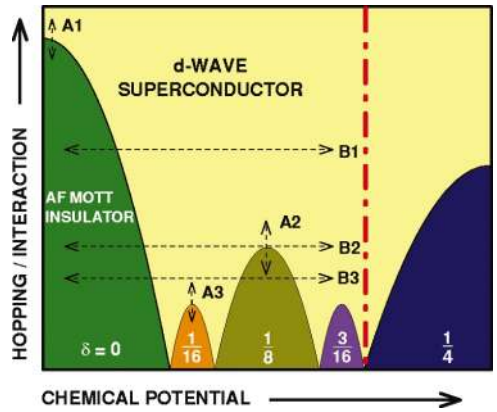

FIG. 13. (Color) A typical global phase diagram of the extended *SO*(5) model in the parameter space of chemical potential and the ratio of boson hopping energy over interaction energy (see Chen, Capponi, *et al.*, 2003 for details). This phase diagram shows self-similarity among the insulating states at half filling and other rational filling fractions. There are two types of superfluid-insulator transition. The quantum phase transition of class *A* can be approached by varying the hopping energy, for example, by applying a pressure and magnetic field at constant doping. The quantum phase transition of class *B* can be realized by changing the chemical potential or doping. This theoretical phase diagram can be compared with the global phase diagram of the high-T_c cuprates. Different families of cuprates correspond to different traces of class *B*. For example, we believe YBCO is *B*1-like, BSCO may be close to *B*2-like, and LSCO is *B*3-like. The vertical dash-dotted line denotes a boundary in the overdoped region beyond which our pure bosonic model becomes less accurate. All the phase boundaries in this figure can be classified into direct first-order transitions (type 1), two second-order transitions (type 2), or a marginal case with enhanced symmetry (type 1.5). Type-2 transitions between CDW lobes and the superconducting state lead to intermediate supersolid phases.

ear σ model [Eq. (34)] is another example. On the other hand, the static, or projected *SO*(5) symmetry can be realized in class-*B*, type-1.5 transitions. We believe that the AF-to-SC transitions in the YBCO, BCCO, and NCCO systems correspond to class-*B*1 transitions. These systems have only an AF-to-SC transition, which can be further subdivided into types 1, 1.5, and 2, but they do not encounter additional statically ordered fractional insulating phases. On the other hand, the phase transition in the LSCO system, where T_c displays a pronounced dip at $\delta=1/8$, corresponds to the class-*B*3 transition (see Fig. 13). In the high-T_c cuprates, the charge gap at half filling is very large, of the order of $U \sim 6$ eV; it is not possible to induce the class-*A*1 transition from the AF to the SC state by conventional means. However, the charge gap at the fractional insulating states is much smaller, of the order of *J*, and it is possible to induce the class-*A*2 insulator-to-superconductor transition by applying pressure (Locquet *et al.*, 1998; Sato *et al.*, 2000; Arumugam *et al.*, 2002; Takeshita *et al.*, 2003). It would be interesting to determine whether this transition point could have the full quantum *SO*(5) symmetry.

We can see that the concept of the *SO*(5) superspin indeed gives a simple and unified organizational principle for understanding the rich phase diagram of the cuprates and other related systems. This construction of the global phase diagram can obviously be iterated *ad infinitum* to give a beautiful fractal structure of self-similar phases and phase transitions. All of this complexity can be simply reduced to the five elementary quantum states of the superspin.

C. Numerical simulations of the classical and quantum models

In this section, we review essentially exact numerical studies of the classical *SO*(5) model and the quantum projected *SO*(5) model on a lattice (Hu, 1999b, 2001; Dorneich *et al.*, 2002b; Riera, 2002a, 2002b; Chen, Capponi, *et al.*, 2003; Jöstingmeier *et al.*, 2003). In Sec. V.D we shall discuss the transformation from the microscopic models into the effective *SO*(5) models and determine the effective parameters. Once this is accomplished, the phase diagram of the model can be determined reliably by bosonic quantum Monte Carlo simulations. These calculations can be carried out for system sizes up to two orders of magnitude larger than fermionic quantum Monte Carlo simulations, the latter being plagued, in the physically interesting regime—i.e., close to half filling—by the minus-sign problem (van der Linden, 1992). The effective models can also be studied numerically in three dimensions, a significant advantage, since there exists no AF-ordered phase in two dimensions at finite temperature (nor long-range SC order). Thus we are forced to study the 3D case in order to determine the phase diagram and to show that the scaling behavior is consistent with an *SO*(5)-symmetric critical behavior within the parameter regime studied (temperature and system size). The study of microscopic models in three dimensions was made possible due to a major step forward in the numerically accessible system sizes (Sandvik, 1997, 1999; Dorneich and Troyer, 2001): in the bosonic projected *SO*(5) model ~10 000 sites were included, in contrast to just ~100 sites in fermionic quantum Monte Carlo calculations (Dopf *et al.*, 1992; Dagotto, 1994; Imada *et al.*, 1998). The numerical results, obtained by the technique of stochastic series expansion (Sandvik, 1997, 1999) and reviewed here, show that the projected *SO*(5) model can give a realistic description of the global phase diagram of the high-T_c cuprates and accounts for many of their physical properties.

The form of the projected *SO*(5) Hamiltonian is given in Eq. (50). The extended *SO*(5) model also includes the interactions expressed in Eq. (65). We shall discuss the simple *SO*(5) model first. Zhang *et al.* (1999) studied this Hamiltonian analytically within a mean-field approach. At the special point $J_c=2J_s\equiv J$ and $\Delta_s=\tilde{\Delta}_c$, the mean-field level of the ground-state energy of Hamiltonian (50) depends on the AF and SC order parameters $x=\langle t_x^\dagger\rangle$ and $y=\langle t_h^\dagger\rangle$ only via their combination x^2+y^2, which reflects the *SO*(5) invariance of the mean-field approxi-

mation. In the full model, however, quantum fluctuations modify the zero-point energy of the bosons in Eq. (50), thereby, giving a correction to the ground-state energy, which depends on x and y separately, and destroying $SO(5)$ symmetry (Zhang *et al.*, 1999). Hence it is essential to study the full quantum-mechanical model (50), including all quantum fluctuations, which can only be done by means of numerical simulations. After considering the single $SO(5)$ model, we then compare the properties of the projected $SO(5)$ model first in two dimensions with a variety of salient features of high-temperature superconductivity such as the global phase diagram and the neutron-scattering resonance. Finally, we review an extension of these studies to the 3D projected $SO(5)$ model. In particular, we show that the scaling behavior near the multicritical point, within the parameter regime studied (system size and temperature), is consistent with an $SO(5)$-symmetrical behavior. The departure away from $SO(5)$-symmetric scaling can only occur in a narrow parameter regime that is hardly accessible either experimentally or numerically.

After numerically solving the projected $SO(5)$ model, we obtain Fig. 14(a), which gives the mean hole-pair and magnon densities as a function of the chemical potential for $T/J=0.03$ and their $T\to 0$ extrapolations (Dorneich *et al.*, 2002b). Similar to the mean-field results, a jump in the densities can be clearly seen at $\mu_c=-0.175$, with a shift in respect to the mean-field value due to the stronger fluctuations of hole pairs, as can be seen in the Gaussian contributions (Zhang *et al.*, 1999). The nature of the phase transition at $\mu=\mu_c$ can be determined by studying histograms of the hole-pair distribution for fixed $\mu=\mu_c$. While in a homogeneous phase the density peaks at its mean value, at $\mu=\mu_c$ we obtain two peaks, which indicates a first-order transition with a phase separation between (almost) hole-free regions and regions with high hole-pair density. From Fig. 14(b) we see that the transition is of first order for $T<T_P=(0.20\pm0.01)J$ at $\mu=\mu_P=(-0.168\pm0.002)J$. Above T_P, the histograms show strongly fluctuating hole-pair densities, suggesting the presence of critical behavior.

Based on these results, the phase diagram of the 2D projected $SO(5)$ model is obtained in Fig. 15. Unlike the generic three-dimensional phase diagrams presented in Fig. 10, there can be no finite-temperature Néel transition in $D=2$ because of the Mermin-Wagner theorem. On the other hand, a continuous transition of the Kosterlitz-Thouless type is possible for the SC-to-normal-state transition at finite temperature. The 3D phase diagram shown in Fig. 10(a) takes the form of Fig. 15 in $D=2$, where the first-order line separating the AF and SC phases merges into the continuous Kosterlitz-Thouless transition at a tricritical point P. The SC phase with finite superfluid density ρ_s is identified by the power-law decay of the SC correlation function:

$$C_h(r)=[t_h^\dagger(r)+t_h(r)][t_h^\dagger(0)+t_h(0)].$$

The Kosterlitz-Thouless transition line in Fig. 15(a) separates the power-law $[C_h(r)\propto r^{-\alpha}]$ from rapid exponential decay $[C_h(r)\propto e^{-\lambda r}]$. A reliable and accurate distinction between these two decay behaviors requires a finite-size scaling with large system sizes, as well as an efficient quantum Monte Carlo estimator for the Green's functions appearing in the correlation function. With its nonlocal update scheme and with our new estimators for arbitrary Green's functions, stochastic series expansion provides both (for details, see Dorneich and Troyer, 2001). An alternative method for detecting a Kosterlitz-Thouless transition exploits the fact that the superfluid density jumps from zero to a finite value at the Kosterlitz-Thouless temperature T_{KT} (Nelson and Kosterlitz, 1977). Within stochastic series expansion, the superfluid density can be measured quite easily by counting winding numbers (Harada and Kawashima, 1997). Numerically, this criterion is preferable to the arduous process of direct determination of decay coefficients. Figure 15(a) plots the phase diagram obtained by applying both criteria independently. The figure shows that the projected $SO(5)$ model indeed has a Kosterlitz-Thouless phase with quasi-long-range order whose domelike form in μ-T space looks like that of the high-T_c cuprates. Both criteria produce the same clearly pronounced phase separation line. It is well known that a similar transition cannot occur for antiferromagnets (Chakravarty *et al.*, 1988) and that the finite-T AF correlation length ξ is always finite and behaves like $\xi\propto e^{2\pi\rho_s/k_BT}$, with ρ_s being the spin stiffness. This fact is confirmed by our numerical results.

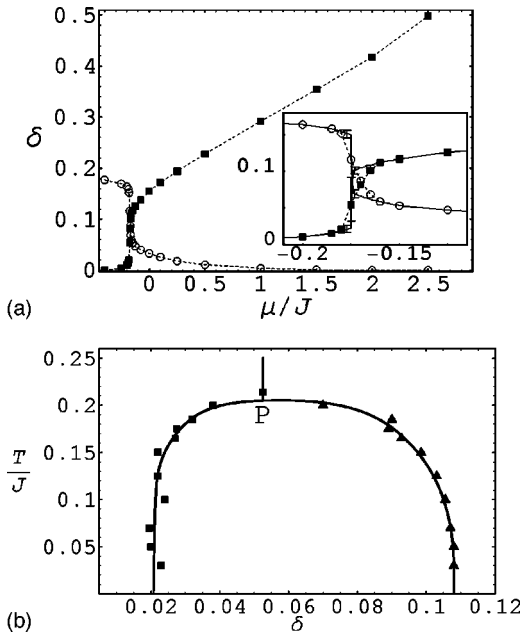

FIG. 14. Effect of the chemical potential and of temperature on hole density: (a) ■, hole concentration $\delta=\rho/2=\frac{1}{2}\langle t_h^\dagger t_h\rangle$ and ○, magnon density $\Sigma_\alpha\frac{1}{2}\langle t_\alpha^\dagger t_\alpha\rangle$ as a function of the chemical potential μ at $T/J=0.03$. The small inset shows a detailed view of the μ region in which the hole-pair density jumps to a finite value; (b) hole densities of the coexisting phases on the first-order transition line from (almost) zero to finite hole density at $\mu=\mu_c$ as a function of temperature.

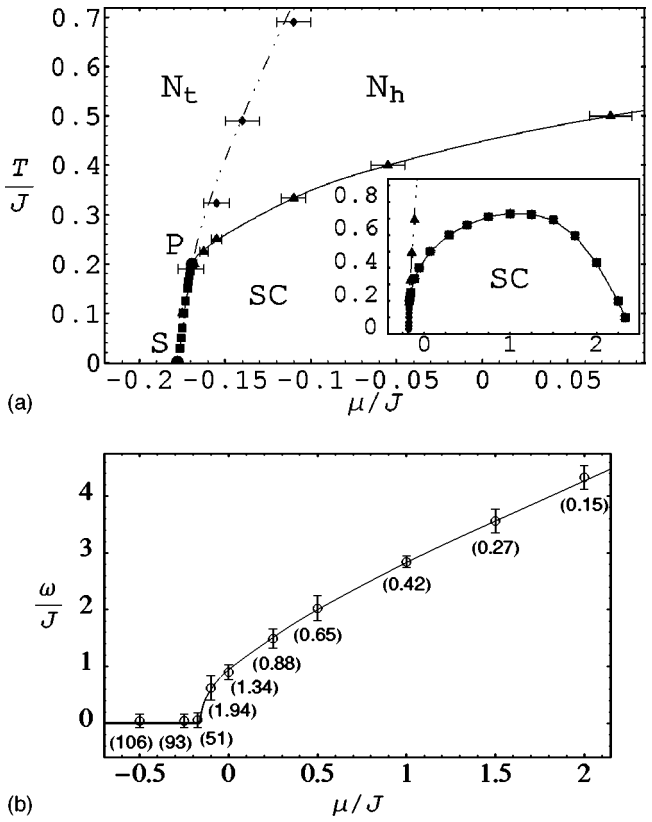

FIG. 15. Quantum Monte Carlo simulations for the projected $SO(5)$ model in $D=2$: (a) Phase diagram [see Eq. (50) with $J_c=J_S$] in $D=2$: The squares between S and the tricritical point P trace the first-order line of phase separation. The solid line from P to the right edge of the plot traces the Kosterlitz-Thouless transition between the SC and normal states. The dashed line separating N_t (triplet-dominated region) and N_h (hole-pair-dominated region) describes the line of equal AF and SC correlation lengths. The small inset shows the same phase diagram on a larger μ scale, covering the whole KT phase. The tricritical point P appears as a result of the Mermin-Wagner theorem, which does not allow spin ordering in $D=2$ at finite temperature. (b) Energy of a single-magnon excitation in the projected $SO(5)$ model as a function of the chemical potential. This corresponds to the resonance energy of the (π,π) peak of the spin correlations in the fermionic model (magnons are defined to carry the momentum of the AF order). The numbers in parentheses indicate the peak weights, i.e., the area under the peak. (20×20 lattice at temperature $T/J=0.1$.) From Jöstingmeier *et al.*, 2003.

One condition required for an $SO(5)$-symmetric point is that the formation energies of hole-pair bosons and of magnons be identical. This condition is fulfilled along the line from S to the tricritical point P in Fig. 15. Another necessary condition is that hole pairs and magnons behave in the same way at long distances. This condition is fulfilled on the dashed line in Fig. 15, where the AF and SC correlation lengths ξ become equal. Interestingly, these two conditions are met (within error-bar accuracy) at the tricritical point P. Of course, the correlation length is still finite here; however, we find relatively large ξ values of order 10 to 15 in the immediate vicinity of point P, demonstrating the importance of $SO(5)$ critical fluctuations in this region.

In addition, in realistic electron systems, the long-range part of the Coulomb repulsion between the doubly charged hole pairs disfavors phase separation, while extended short-ranged interactions described by Eq. (65) could lead to the formation of stripes and checkerboard types of states, as discussed in Sec. IV.B. To study the effect of off-site Coulomb interaction, we have added additional nearest-neighbor and next-nearest-neighbor Coulomb repulsions V_c and $V_c'=0.67V_c$ to the projected $SO(5)$ model. Indeed, a relatively modest Coulomb repulsion of $V_c/J\approx0.2$ is enough to completely destroy the phase separation. One interesting effect of Coulomb interaction in two dimensions is thus to push down the tricritical point into a quantum-critical point at $T=0$. In Sec. IV.A and in Fig. 9(c), we showed that the $SO(5)$-symmetric behavior is recovered at the special point when a direct first-order transition changes into two second order transitions. Therefore the extended Coulomb interaction plays the role of the w parameter in Fig. 9(c) and could restore the $SO(5)$ symmetry at the quantum critical point.

When larger values of extended interaction parameters in Eq. (65) are considered, new insulating phases are expected, following from the general discussions in Sec. IV.B and Fig. 13. Indeed, Chen, Capponi, *et al.* (2003) have performed extensive quantum Monte Carlo simulations of the $SO(5)$ model and have determined its generic phase diagram, as shown in Fig. 16. In addition to the AF and SC phases, there is an insulating pair-density-wave state around a doping range of $x=1/8$, where hole pairs form a checkerboard state in the AF-ordered background, as depicted in Fig. 12(d). Near the phase boundaries between the AF, PDW, and SC phases, there are mixed phases with coexisting order. The topology of the phase diagram obtained from the simulation agrees well with the mean-field theory of the extended $SO(5)$ model. One of the main features of the $SO(5)$ theory is that it provides an elegant explanation for the neutron resonance peak observed in some high-T_c cuprates at $q=(\pi,\pi)$ (Demler and Zhang, 1995; Zhang, 1997). We refer the reader to the detailed discussion of the resonance mode in Sec. VI. Experiments show that the resonance energy $\omega_{\rm res}$ is an increasing function of T_c, i.e., $\omega_{\rm res}$ increases as a function of doping in the underdoped region and decreases in the overdoped region (Fong *et al.*, 2000). Figure 15(b) plots the resonance frequency determined from the spin-correlation spectrum obtained for the projected $SO(5)$ model. As illustrated in Fig. 8, the spin-wave excitations are massless Goldstone modes in the AF phase at $\mu<\mu_c$ (and $T=0$) and become massive when entering into the SC phase. $\omega_{\rm res}$ increases monotonically up to the optimal doping $\mu_{\rm opt}\approx1$. In the overdoped range of the simple $SO(5)$ model, however, $\omega_{\rm res}$ is increasing more, in contrast to what happens in the cuprates. The resonance peak continuously loses weight as μ increases, which is consistent with experimental observations (Fong *et al.*, 2000).

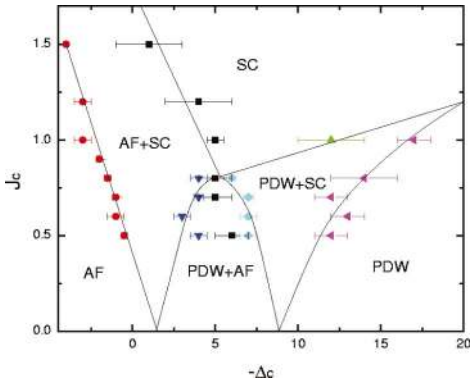

FIG. 16. (Color) The phase diagram of the extended *SO*(5) model obtained by quantum Monte Carlo simulation. The parameters used in simulation are $\Delta_s=4.8$, $V_c=4.1010$, $V_c'=3.6329$, and $J_\pi=V_\pi=0$. The lines are guides to the eye only. The overall topology of the phase diagram agrees well with the global phase diagram presented in Fig. 13.

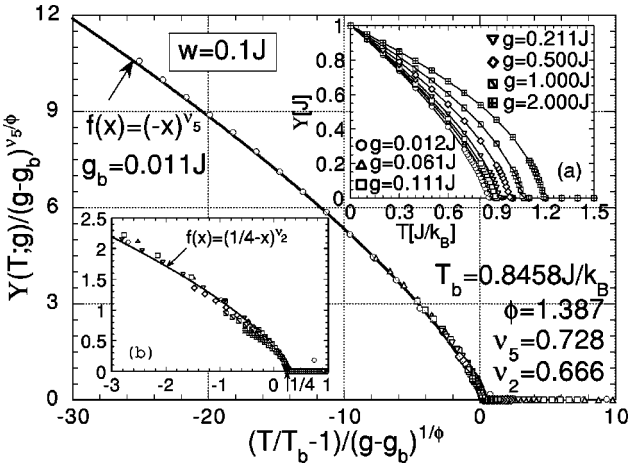

FIG. 17. Scaling of the superfluid density near the *SO*(5) bicritical point obtained by classical Monte Carlo simulations. The critical behaviors of the superfluid density for various g fit into a single scaling curve, from which *SO*(5) scaling exponents were obtained. From Hu, 2001.

A comparison of the critical temperature T_c obtained from Fig. 15 and the resonance frequency $\omega_{\rm res}$ at optimal doping yields the ratio $T_c/\omega_{\rm res,opt}=0.23$. Again, this is in qualitative accord with the corresponding ratio for $YBa_2Cu_3O_{6+x}$, for which the experimentally determined values $T_c=93$ K (thus $k_BT_C=8.02$ meV) and $\omega_{\rm res,opt}=41$ meV yield $T_c/\omega_{\rm res,opt}=0.20$.

Now we turn to the numerical simulations of the *SO*(5) models in $D=3$. Two aims motivate our studies of the projected *SO*(5) model in three dimensions. First, we expect to find both AF and SC phases with real long-range order. We need to determine which of the two types of phase diagram introduced in Sec. IV.A (see Fig. 10) is realized in the numerical simulations. Second, we would like to determine whether the projected *SO*(5) model has a certain multicritical point at which the *SO*(5) symmetry is asymptotically restored. Since the cuprates have a pronounced 2D layer structure with relatively weak couplings between adjacent CuO_2 planes, the 2D and the isotropic 3D model (discussed here) should be two extreme poles for the possible range of properties of real high-T_c materials. Most numerical data reviewed here have been obtained by a finite-size scaling with lattice sites up to 10 000 (Dorneich and Troyer, 2001; Dorneich *et al.*, 2002a, 2002b; Jöstingmeier *et al.* 2003).

The phase diagram and the scaling behavior of the classical *SO*(5) model have been studied in detail by Hu (2001) by means of classical Monte Carlo simulations. Classical simulations are by orders of magnitude easier to perform and less demanding of resources than quantum Monte Carlo simulations; hence very large system sizes can be simulated and highly accurate data can be obtained. The classical *SO*(5) model can be obtained directly from the quantum *SO*(5) model by taking the expectation value of the Hamiltonian in the variational state, as given by Eq. (64) and assuming a constant value of $\theta(x)$. This takes the form

$$H=-J\sum_{\langle x,x'\rangle} m_a(x)m_a(x')+g\sum_x m_\alpha^2(x)+w\sum_x m_\alpha^2(x)m_i^2(x), \tag{66}$$

where $g=\Delta_s-\tilde{\Delta}_c$ is the quadratic symmetry-breaking term, and w is an additional quartic symmetry-breaking term. Hu established the $T(g)$ phase diagram, which is of the type illustrated in Fig. 10(a). The model has an AF and a SC phase which meet at a bicritical point $(T_{bc},g_{bc}=0)$. The boundary lines between the disordered and AF phases and between the disordered and SC phases merge tangentially at the bicritical point, which is an important characteristic of *SO*(5) symmetry (Hu, 2001). The following scaling properties were determined by Hu and will be used to study the restoration of *SO*(5) symmetry in the projected *SO*(5) model.

For an analysis of the crossover phenomenon, an ansatz for the behavior of the helicity modulus Υ in the range $T<T_c(g)$ and $g>0$ is used, which is suggested by scaling theory (Hu, 2001):

$$\Upsilon(T,g)\propto(g-g_{bc})^{\nu_5/\phi}\times f[(T/T_{bc}-1)/(g-g_{bc})^{1/\phi}]. \tag{67}$$

Here, ν_5 is the critical exponent for correlation length at $n=5$ and ϕ the crossover exponent. Using Eq. (67), the values of ν_5 and ϕ can be determined in two steps. First, performing a g scan of $\Upsilon(T=T_{bc},g)$ returns the ratio ν_5/ϕ:

$$\Upsilon(T_{bc},g)/\Upsilon(T_{bc},g')=[(g-g_{bc})/(g'-g_{bc})]^{\nu_5/\phi}. \tag{68}$$

Then, ϕ is obtained from the slopes $(\partial/\partial T)[\Upsilon(T,g)/\Upsilon(T,g')]$ via

$$\phi = \ln\left(\frac{g_2 - g_{bc}}{g_1 - g_{bc}}\right) \Bigg/ \ln\left(\frac{\partial}{\partial T}\ \frac{\Upsilon(T,g_1)}{\Upsilon(T,g_1')}\bigg|_{T=T_{bc}} \Bigg/ \frac{\partial}{\partial T}\ \frac{\Upsilon(T,g_2)}{\Upsilon(T,g_2')}\bigg|_{T=T_{bc}}\right) \tag{69}$$

if g_1, g_1', g_2, and g_2' are related by $(g_1-g_{bc})/(g_1'-g_{bc}) = (g_2-g_{bc})/(g_2'-g_{bc})>0$. From the scaling plots presented in Fig. 17, Hu finds the values $\nu_5/\phi = 0.523\pm0.002$ and $\phi = 1.387\pm0.030$.

According to the scaling ansatz in Eq. (67), the transition lines between the disordered and AF phases, and between the disordered and SC phases near the bicritical point, should be of the form

$$B_2(g - g_{bc})^{1/\phi} = \frac{T_c(g)}{T_{bc}} - 1$$

and

$$B_3(g_{bc} - g)^{1/\phi} = \frac{T_N(g)}{T_{bc}} - 1. \tag{70}$$

The ratio B_2/B_3 should be given by the inverse ratio between the AF and SC degrees of freedom, i.e.,

$$B_2/B_3 = 3/2. \tag{71}$$

The values numerically determined by Hu indeed have the correct ratio: $B_2=1/4$ and $B_3=1/6$.

We now proceed to the phase diagram of the 3D quantum $SO(5)$ model (Jöstingmeier *et al.*, 2003). Figure 18 shows the AF and SC phases, as expected. Furthermore, the two phase transition lines merge tangentially into a multicritical point (at $T_{bc}=0.960\pm0.005$ and $g_{bc} = -0.098\pm0.001$) just as in the classical $SO(5)$ system (Hu, 2001). The line of equal correlation decay of hole pairs and triplet bosons also merges into this bicritical point P—a necessary condition at this point for the restoration of $SO(5)$ symmetry. Unlike the corresponding phase in the classical model (Hu, 2001), the SC phase only extends over a finite g range due to the hard-core constraint of the hole-pair bosons and agrees with experimentally determined phase diagrams of the cuprates. Obviously, the quantum-mechanical $SO(5)$ model is "more physical" in this respect than the classical $SO(5)$ model. In real cuprates the ratio between the maximum temperatures T_c and T_N is about 0.17–0.25, whereas in the projected $SO(5)$ model we obtain the values $T_c/J=1.465\pm0.008$ at $\mu_{opt}/J\approx1.7$ and $T_N/J = 1.29\pm0.01$ at $\mu\to\infty$. Hence T_c is slightly larger than T_N. In order to obtain realistic ratio for the transition temperatures, it is necessary to relax the strict condition $J_s = J_c/2$, where $SO(5)$ symmetry is restored on a mean field level. Choosing $J_c/2=0.225J_s$ yields the correct ratio. However, the static symmetry may still be recovered at the bicritical point, as discussed in Sec. IV.A. At this point we are primarily concerned with the multicritical behavior, so we stay with the simple $SO(5)$ model.

A closer look at the phase transition line between the points S and P (see Fig. 18) reveals that this line is slightly inclined, unlike the vertical line seen in the classical $SO(5)$ model. This indicates that a finite latent heat is connected with the AF-SC phase transition. In addition, this means that μ is not a scaling variable for the bicritical point P, as it is in the classical model. The result in Fig. 18 shows a phase separation regime at $\mu = \mu_c$ on the entire transition line from S to P.

We now review the results of a scaling analysis for the 3D quantum $SO(5)$ model, similar to the one performed by Hu (2001) in a classical $SO(5)$ system (Jöstingmeier *et al.*, 2003). From this analysis we also find that the $SO(5)$ symmetry is restored in the region around the bicritical point ($T_{bc}=0.96$, $\mu=-0.098$).

We have determined the critical exponents for the onset of AF and SC orders for various chemical potentials as a function of temperature. Far into the SC range, at $\mu=1.5$, we find that the SC helicity modulus follows the scaling form (Fisher *et al.*, 1973)

$$\Upsilon \propto (1 - T/T_c)^{\nu} \quad \text{with} \quad \nu = 0.66 \pm 0.02,$$

which agrees with the values obtained by both the ϵ expansion and numerical analysis of a 3D XY model. On the AF side, the error bars are larger. For $\mu=-2.25$,

$$C_{AF}(\infty) \propto (1 - T/T_c)^{\beta_3} \quad \text{with} \quad \beta_3 = 0.35 \pm 0.03,$$

as expected for a 3D classical Heisenberg model.

To determine ν and ϕ, we use Eqs. (68) and (69), which express the scaling behavior in the crossover regime (cf. Hu, 2001). We obtain the ratio

$$\nu_5/\phi = 0.52 \pm 0.01,$$

which matches the results of the ϵ expansion (Kosterlitz *et al.*, 1976; Hu and Zhang, 2000). ϕ is then obtained by using Eq. (69). The result is

$$\phi = 1.43 \pm 0.05,$$

which also agrees with the ϵ expansion for an $SO(5)$ bicritical point (see Fig. 19) and with the results of Hu (2001).

Let us finally return to the comment by Aharony (2002), who, via a rigorous argument, demonstrated that the decoupled fixed point is stable, as opposed to the biconical and $SO(5)$ fixed points. However, he also commented that the unstable flow is extremely slow for the $SO(5)$ case due to the small crossover exponent.

The scaling analysis of the 3D projected $SO(5)$ model has produced a crossover exponent which matches the value obtained from a classical $SO(5)$ model and from the ϵ expansion. This provides strong evidence that the static correlation functions at the $SO(5)$ multicritical point are controlled by a fully $SO(5)$-symmetric point, at least in a large transient region. However, the isotropic

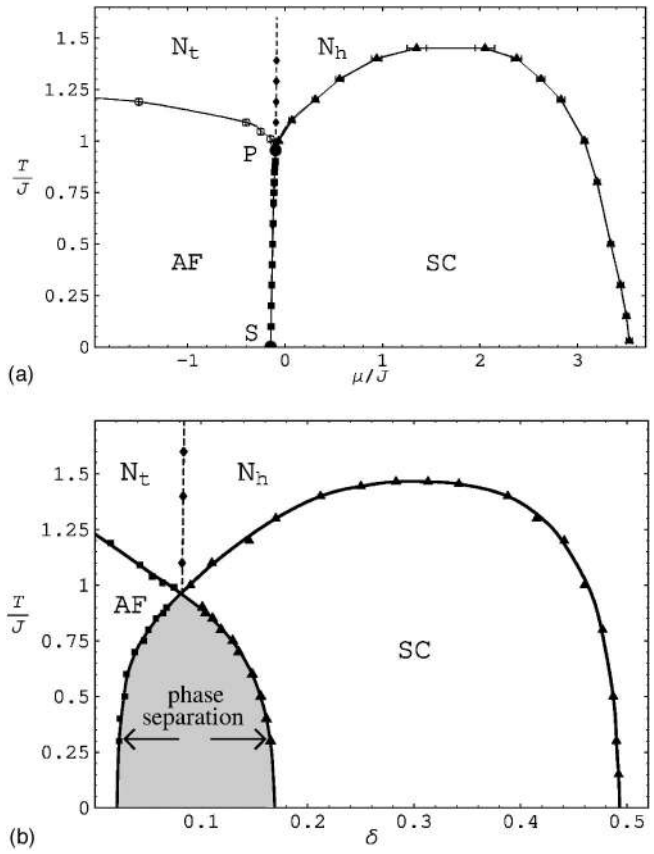

FIG. 18. Quantum Monte Carlo simulations for the projected $SO(5)$ model in $D=3$: (a) $T(\mu)$ phase diagram with $J_s=J_c/2$ and $\Delta_s=\Delta_c=J$. N_h is the hole-pair-dominated part, N_t the triplet-dominated part of the high-temperature phase without long-range order. The separation line between N_h and N_t is the line of equal spatial correlation decay of hole-pairs and bosons. (b) $T(\delta)$ phase diagram as a function of hole doping $\delta=n_h/2$. The first-order transition line from S to P in the $T(\mu)$ diagram becomes a forbidden region due to phase separation. These two phase diagrams are consistent with those presented in Figs. 10(a) and 10(b) based on general arguments.

$SO(5)$ and biconical fixed points have very similar critical exponents. Thus, given the statistical and finite-size errors, as well as the errors due to the extrapolation of the ϵ-expansion value to $\epsilon=1$, we cannot exclude the possibility that the multicritical point on the phase diagram is actually the biconical one. On the other hand, the biconical fixed point should be accompanied by a uniform AF/SC mixed region (as a function of chemical potential), which was not observed. The decoupled fixed point appears to be the least compatible with the numerical results presented above. Even if the bicritical point were fundamentally unstable, as suggested by Aharony (2002), one would have to come unrealistically close to T_{bc} to observe this. For example, for the projected $SO(5)$ models, Arrigoni and Hanke (1999) estimated that deviations from the $SO(5)$ behavior might be observed only when the reduced temperature becomes smaller than $|T-T_{bc}|/T_{bc}<10^{-11}$. On the other hand, the other scaling variables, although initially of the order of 1, rapidly scale to zero due to large, negative exponents. Therefore the $SO(5)$ regime starts to become important as soon as the AF and SC correlation lengths become large and basically continues to affect the scaling behavior of the system over the whole accessible region.

Summarizing, accurate quantum Monte Carlo calculations show that the projected $SO(5)$ model, which combines the idea of $SO(5)$ symmetry with a realistic treatment of the Hubbard gap, is characterized by an $SO(5)$-symmetric bicritical point, at least within a large transient region. Possible flow away from this symmetric fixed point occurs only within a narrow region in reduced temperature, making it impossible to observe either experimentally or numerically. This situation is common to many systems in condensed-matter physics. For example, due to the well-known Kohn-Luttinger effect (Kohn and Luttinger, 1965), the Fermi-liquid fixed point is always unstable towards a SC state. However, this effect is experimentally irrelevant for most metals since it only works at extremely low temperatures. Another example is the "ordinary" superconductor-to-normal-state transition at T_c. Strictly speaking, due to the coupling to the electromagnetic field, this fixed point is always unstable (Halperin *et al.*, 1974). However, this effect is experimentally irrelevant since the associated critical region is extremely small. Similarly, irrespective of the question of ultimate stability, the $SO(5)$ fixed point is a robust one in a large transient regime, and it can control the physics near the AF and SC transitions. For all practical purposes, the multicritical point is dominated by the initial flow toward the $SO(5)$-symmetric behavior.

V. MICROSCOPIC ORIGIN OF THE *SO*(5) SYMMETRY

A. Quantum lattice models with exact *SO*(5) symmetry

Soon after the general $SO(5)$ theory was proposed, a class of microscopic fermion models with exact $SO(5)$ symmetry was constructed (Burgess *et al.*, 1998; Henley, 1998; Rabello *et al.*, 1998; Scalapino *et al.*, 1998; Wu, Hu, and Zhang, 2003). These models fall into three general classes. The first class contains models with two sites per unit cell, such as the ladder and the bilayer models. In these models, a simple condition among the local interaction parameters ensures full quantum $SO(5)$ symmetry. The second class contains models with only one site in the unit cell but with longer-ranged interactions. The third class contains higher-spin fermion models, in particular the spin-3/2 Hubbard model. Remarkably, in this case the models are always $SO(5)$ symmetric without any fine-tuning of the local interaction parameters and doping level.

The microscopic $SO(5)$-symmetric models in the ladder or bilayer models were first constructed by Scalapino, Zhang, and Hanke (Scalapino *et al.*, 1998) and have been studied extensively both analytically and

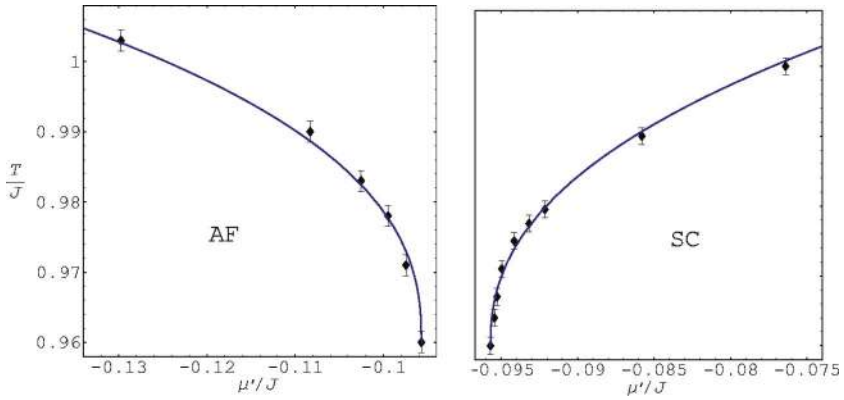

FIG. 19. (Color) Scaling of T_N and T_c near the $SO(5)$ bicritical point. Both T_N and T_c merge into the bicritical point tangentially, with the crossover exponent of $\phi=1.43\pm0.05$.

numerically.[3] In these models, there are two sites and $4^2=16$ states in the unit cell. In Sec. III.A we discussed the construction of $SO(5)$ symmetry operators in terms of the fermion operators for two sites in the unit cell. Here we shall address the question of whether the microscopic Hamiltonian commutes with the $SO(5)$ symmetry generators. Three interaction parameters, U, V, and J, fully characterize the most general local interactions on the two sites, which take the form

$$H(x) = U\left(n_{c\uparrow} - \frac{1}{2}\right)\left(n_{c\downarrow} - \frac{1}{2}\right) + (c \to d) + V(n_c - 1)(n_d - 1) + J\vec{S}_c\vec{S}_d - \mu(n_c + n_d). \quad (72)$$

This Hamiltonian can be solved easily for the 16 states on two sites, and the six energy levels are given in Fig. 20. Since the $SO(5)$ symmetry generators can be expressed in terms of the microscopic fermion operators, we can easily determine the transformation properties of these states under the $SO(5)$ group. There are three $SO(5)$ singlet states and two fermionic quartet states, which form the fundamental spinor representations of $SO(5)$. We see that the four fermionic states in each group are always degenerate, without any fine-tuning of the interaction parameters. The three spin-triplet states at half filling and the two paired states away from half filling form the five-dimensional vector representation, but they are only degenerate if we specify one condition, namely,

$$J = 4(U + V). \quad (73)$$

This condition ensures local $SO(5)$ symmetry within the unit cell. Remarkably, under this condition, a global $SO(5)$ symmetry is also obtained for a bipartite lattice including nearest-neighbor hopping. This is best demonstrated when we write the model in a manifestly $SO(5)$-covariant manner. On a bipartite lattice, we introduce the four-component spinor operator

$$\Psi_\alpha(x \in even) = \begin{pmatrix} c_\sigma(x) \\ d_\sigma^\dagger(x) \end{pmatrix}, \quad \Psi_\alpha(x \in odd) = \begin{pmatrix} d_\sigma(x) \\ c_\sigma^\dagger(x) \end{pmatrix}. \quad (74)$$

The microscopic Hamiltonian including intra-rung hopping $t_\perp$ and inter-rung hopping $t_\parallel$ is given by

$$H = -2t_\parallel \sum_{\langle x,x'\rangle} [c_\sigma^\dagger(x)c_\sigma(x') + d_\sigma^\dagger(x)d_\sigma(x')] - 2t_\perp \sum_x [c_\sigma^\dagger(x)d_\sigma(x) + \text{H.c.}] + \sum_x H(x). \quad (75)$$

Under condition (73), this Hamiltonian can be expressed in a manifestly $SO(5)$-invariant manner:

$$H = 2t_\parallel \sum_{\langle x,x'\rangle} [\Psi_\alpha(x)R^{\alpha\beta}\Psi_\beta(x') + \text{H.c.}] + t_\perp(\Psi_\alpha R^{\alpha\beta}\Psi_\beta + \text{H.c.}) + \sum_x \frac{J}{4}L_{ab}^2(x) + \left(\frac{J}{8} + \frac{U}{2}\right)(\Psi_\alpha^\dagger\Psi_\alpha - 2)^2, \quad (76)$$

where the R matrix is defined in Sec. IX.B. This model was originally constructed for the two-legged ladder system, but it works equally well for a two-dimensional bilayer system.

The phase diagram of this $SO(5)$-symmetric model has been studied extensively in the literature. This simple model has a rich and rather complex phase diagram, depending on the coupling strength and doping. However, because of the constraints imposed by the $SO(5)$ symmetry, the phase diagram is much better understood compared to other related models. In the strong-coupling limit, three phase boundary lines are determined from the level crossing of the bosonic states on two sites. At $V=-2U$, the E_0 state becomes degenerate with the E_3 states; at $V=-U$, the E_0 state becomes degenerate with the E_1 states; finally, at $V=0$ the E_1 states become degenerate with the E_3 states. The strong-coupling phase diagram at half filling is shown in Fig. 20(b).

[3]Such studies include Duffy *et al.*, 1998; Lin *et al.*, 1998; Schulz, 1998; Shelton and Senechal, 1998; Arrigoni and Hanke, 1999; Bouwknegt and Schoutens, 1999; Eder *et al.*, 1999; Furusaki and Zhang, 1999; Hong and Salk, 1999; Frahm and Stahlsmeier, 2001).

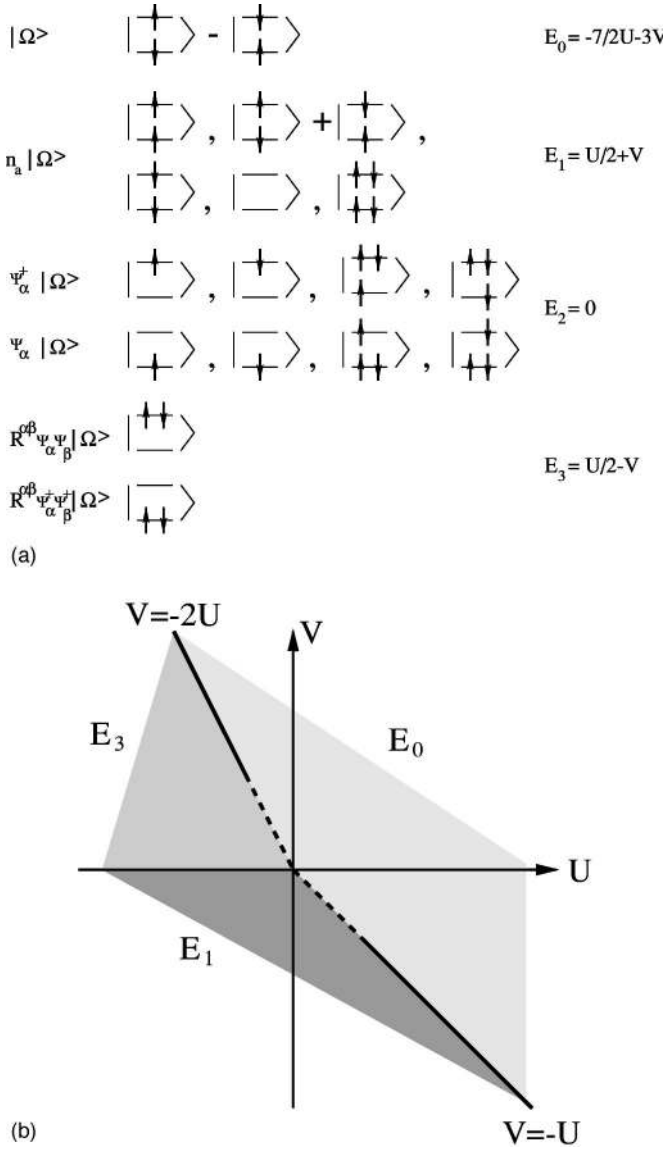

FIG. 20. Quantum lattice model with exact *SO*(5) symmetry: (a) Under the condition specified by Eq. (73), the 16 states on a rung are classified into six groups, each transforming irreducibly under the *SO*(5) group. $|\Omega\rangle$ is an *SO*(5) singlet state; $n_a|\Omega\rangle$ describes five states that transform as *SO*(5) vectors; $\Psi_\alpha^\dagger|\Omega\rangle$ are four states that form an *SO*(5) spinor; four states $\Psi_\alpha|\Omega\rangle$ also correspond to a spinor; $R_{\alpha\beta}\Psi_\alpha\Psi_\beta|\Omega\rangle$ and $R_{\alpha\beta}\Psi_\alpha^\dagger\Psi_\beta^\dagger|\Omega\rangle$ are two *SO*(5) singlet states. The figure also gives energies of all multiplets for the *SO*(5)-symmetric ladder model described by Eqs. (72) and (73). (b) Strong-coupling phase diagram of the *SO*(5)-symmetric ladder model in the (U,V) space. The E_0, E_1, and E_3 phases are regions in parameter space where the respective states have the lowest energy.

In the strong-coupling E_0 phase, a robust ground state is obtained as a product of *SO*(5) singlets on the rungs. This type of insulating state does not break any lattice translational or internal rotational symmetry. Since there are two electrons per unit cell, this insulating state is also adiabatically connected to the band insulator state. This state is separated from the excited *SO*(5) quintet vector states by a finite energy gap, $\Delta=E_1-E_0=J$. In this regime, we consider the low-energy manifold consisting of six states, namely, one E_0 state $|\Omega\rangle$ and five E_1 states $n_a|\Omega\rangle$ per rung. The low-energy effective Hamiltonian can be obtained easily by a second-order strong-coupling expansion and is exactly given by the *SO*(5) quantum nonlinear σ model Hamiltonian given in Eq. (34), with $\chi^{-1}=J$ and $\rho=J_\parallel=t_\parallel^2/(U+J/2)$. The operators L_{ab} and n_a act on the six states in the following way:

$$L_{ab}(x)|\Omega(x)\rangle=0,$$

$$L_{ab}(x)|n_c(x)\rangle=i\delta_{bc}|n_a(x)\rangle-i\delta_{ac}|n_b(x)\rangle,$$

$$n_a(x)|\Omega(x)\rangle=|n_a(x)\rangle,\quad n_a(x)|n_b(x)\rangle=\delta_{ab}|\Omega(x)\rangle. \quad (77)$$

Since the quantum model is exactly *SO*(5) symmetric, the anisotropy term $V(n)$ vanishes identically. Therefore we see that the *SO*(5) quantum nonlinear σ model, phenomenologically introduced in Sec. III.B, can indeed be rigorously derived from the microscopic Scalapino-Zhang-Hanke model defined on a ladder and on a bilayer.

In the E_0 regime, the Scalapino-Zhang-Hanke model on the half-filled ladder has an *SO*(5) rung singlet ground state with a finite gap towards the *SO*(5) quintet excitations. A chemical-potential term of the order of the gap induces a second-order quantum phase transition into the SC phase. On the other hand, the Scalapino-Zhang-Hanke model on the bilayer has a quantum phase transition even at half filling, when $J_\parallel/J\sim1$. For $J>J_\parallel$, the ground state is a Mott insulator without any symmetry breaking, with a finite gap towards the quintet excitations. For $J<J_\parallel$, the ground state is classically ordered and breaks the *SO*(5) symmetry spontaneously by aligning the superspin in a particular direction, which can be either AF or SC. Since the residual symmetry is *SO*(4), the Goldstone manifold of the σ model is a four-dimensional sphere $SO(5)/SO(4)=S^4$. Away from half filling, the *SO*(5) symmetry is broken by the chemical-potential term. According to Table I, the π operators carry charge ±2, and we have $[H,\pi_\alpha^\dagger]=2\mu\pi_\alpha^\dagger$. However, although the Hamiltonian does not commute with all the *SO*(5) generators, it still commutes with the Casimir operator L_{ab}^2. For this reason, all states are still classified by *SO*(5) quantum numbers and the *SO*(5) symmetry makes powerful predictions despite a broken symmetry away from half filling. The phase diagram for the two-dimensional Scalapino-Zhang-Hanke bilayer model is shown in Fig. 21. For $J_\parallel\gg J$, the ground state is classically ordered. The chemical potential induces a quantum phase transition from the *SO*(5) uniform mixed AF/SC state to the SC state at $\mu=0$. This transition is exactly the superspin flop transition discussed in Sec. III.B. For $J_\parallel\ll J$, the ground state is quantum disordered at half filling. A second-order quantum phase transition from the singlet Mott insulator state to the SC state is induced at finite $\mu=\mu_c$. The exact *SO*(5) bilayer model offers an ideal theoretical laboratory for studying the collective modes, especially the π-resonance mode dis-

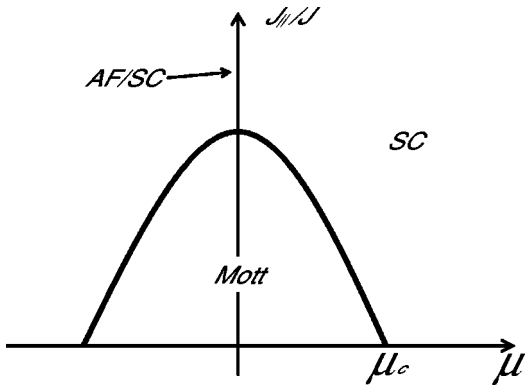

FIG. 21. Phase diagram of the bilayer *SO*(5) model plotted as $J_\parallel/J$ vs μ. The entire phase-transition line from the Mott phase into any of the ordered phases is a second-order quantum phase transition. The Mott insulating state has five massive collective modes. The *SO*(5)-symmetric AF/SC uniform mixed state at half filling has four gapless collective modes. The SC state has a spin-triplet π-resonance mode and one massless charge Goldstone mode.

cussed in Sec. VI, since their sharpness is protected by the exact *SO*(5) symmetry. The Mott phase has five massive collective modes, a doublet of charge modes, and a triplet of spin modes. The energy of the two charge modes splits at finite chemical potential, and the energy of one of the charge modes vanishes at the second-order phase-transition boundary. This charge mode continues into the SC phase as the phase Goldstone mode. The spin-triplet mode of the Mott phase continues smoothly into the SC phase and becomes the pseudo-Goldstone mode, or the π-resonance mode of the SC phase. The ordered phase at half filling has four Goldstone modes. The direction of the order parameter can be smoothly rotated from AF to SC at half filling. When the order parameter points in the AF direction, the four Goldstone modes decompose into two spin-wave modes and two charge modes. When the order parameter is rotated into the SC direction, the four Goldstone modes decompose into a spin triplet and a Goldstone phase mode. The energy of the triplet Goldstone mode (the massive π mode) increases continuously with the chemical potential, while the Goldstone phase mode remains gapless.

Having discussed the E_0 regime at length, let us now turn to the E_1 regime, in which the *SO*(5) quintet state has the lowest energy. In this case, we can restrict ourselves to the low-energy manifold of five states on each rung. The effective theory within this low-energy manifold can again be obtained by the strong-coupling second-order perturbation theory, and is given by

$$H = K \sum_{\langle x,x' \rangle} L_{ab}(x) L_{ab}(x'), \tag{78}$$

where $K = t_\parallel^2/(U/2 - J/4)$. This effective Hamiltonian is the *SO*(5) generalization of the AF spin-1 Heisenberg model. Here we must distinguish between the one-dimensional ladder model and the two-dimensional bilayer model. In one-dimensional models, the ground state is separated from the *SO*(5) vector excitation by a finite-energy gap. In fact, an exact ground state can be constructed for the *SO*(5) vector model by generalizing the AKLT model for the spin-1 chain. Such a state also preserves the lattice translational and internal rotational symmetry. However, in two-dimensional bilayer models, the effective exchange coupling between the *SO*(5) vectors will lead to a state with spontaneously broken *SO*(5) symmetry, with the *SO*(5) adjoint order parameter $\langle L_{ab} \rangle \neq 0$. This order parameter is formed by the linear superposition of two *SO*(5) vector states, n_a and n_b. Without loss of generality, let us consider the case where $\langle L_{15} \rangle \neq 0$. In this case, the *SO*(5) generators L_{15}, $\{L_{23}, L_{24}, L_{34}\}$ leave the state invariant. These set of generators form a $U(1) \times SU(2)$ symmetry group. Therefore the Goldstone manifold is the coset space

$$SO(5)/[U(1) \times SU(2)] = CP_3, \tag{79}$$

where CP_3 is the six (real) dimensional complex projective space, which can be described by the complex coordinates (z_1, z_2, z_3, z_4), satisfying $|z_1|^2 + |z_2|^2 + |z_3|^2 + |z_4|^2 = 1$ and with the points related by a $U(1)$ gauge transformation $z_i \rightarrow e^{i\alpha} z_i$ identified. Since the CP_3 manifold is six dimensional, there are six Goldstone bosons in this case. Here we see that there is an important difference between the *SO*(5)-symmetric Scalapino-Zhang-Hanke model and the *SO*(3)-symmetric Heisenberg model. In the Heisenberg model, the vector representation is identical for the adjoint representation: there is only one type of classically ordered AF state. In the *SO*(5) case, the symmetry breaking can occur either in the vector or the adjoint representations of the *SO*(5) group, which are inequivalent, and the resulting Goldstone manifolds are S^4 and CP_3, respectively. The adjoint symmetry-breaking pattern has been used by Murakami, Nagaosa, and Sigrist to unify *p*-wave superconductivity with ferromagnetism (Murakami *et al.*, 1999).

In the weak-coupling limit, powerful renormalization-group analysis has been applied to study the *SO*(5) symmetry in ladder models. The main conclusions are similar to the strong-coupling analysis; therefore we shall review only the most remarkable and distinct results. Lin, Balents, and Fisher (Lin *et al.*, 1998), Arrigoni and Hanke (1999), Schulz (1998), and Shelton and Senechal (1998) carried out detailed RG analyses and showed that RG transformation always scales the most generic ladder model towards an *SO*(5)-symmetric ladder model. This is a remarkable result and shows that the quantum *SO*(5) symmetry does not need to be postulated at the microscopic level but could emerge as a result of scaling in the long-wavelength and low-energy limit. Moreover, Lin *et al.* (1998) showed that even the *SO*(8) symmetry could emerge at half filling. Another interesting and remarkable result was obtained recently. In the transition region between the singlet E_0 phase and the charge-ordered E_3 phase, RG analysis of the weak-coupling limit showed the existence of a new phase, called the *staggered-flux phase*, or the DDW (*d*-density-wave)

phase, which has staggered circulating current on the plaquettes (Fjaerstad and Marston, 2002; Marston *et al.*, 2002; Schollwoeck *et al.*, 2003; Wu, Liu, and Fradkin, 2003). This phase has been proposed to explain the pseudogap behavior in the high-T_c cuprates (Affleck and Marston, 1988; Chakravarty *et al.*, 2001).

Exactly $SO(5)$-symmetric models can also be constructed for the single-layer model (Burgess *et al.*, 1998; Henley, 1998; Rabello *et al.*, 1998). In this case, there is no natural way to group two sites to form a local, four-component $SO(5)$ spinor. However, one can introduce a $SO(5)$ spinor in momentum space by defining

$$^{t}\Psi_{\mathbf{p}} = \{c_{\mathbf{p}\uparrow}, c_{\mathbf{p}\downarrow}, g(\mathbf{p})c^{\dagger}_{-\mathbf{p}+\mathbf{\Pi},\uparrow}, g(\mathbf{p})c^{\dagger}_{-\mathbf{p}+\mathbf{\Pi},\downarrow}\}, \tag{80}$$

where $g(\mathbf{p}) = \mathrm{sgn}(\cos p_x - \cos p_y) = \pm 1$ is the form factor introduced by Henley (1998). As discussed in Sec. III.A, this factor is needed to ensure the closure of the $SO(5)$ algebra. Indeed, with this choice, the Ψ spinors form the canonical commutation relation

$$\{\Psi^{\dagger}_{\mathbf{p}\alpha}, \Psi_{\mathbf{p}'\beta}\} = \delta_{\alpha\beta}\delta_{\mathbf{p},\mathbf{p}'}, \tag{81}$$

$$\{\Psi^{\dagger}_{\mathbf{p}\alpha}, \Psi^{\dagger}_{\mathbf{p}'\beta}\} = \{\Psi_{\mathbf{p}\alpha}, \Psi_{\mathbf{p}'\beta}\} = -g(\mathbf{p})R_{\alpha\beta}\delta_{\mathbf{p}+\mathbf{p}',\mathbf{\Pi}}. \tag{82}$$

If we restrict both $\mathbf{p}$ and $\mathbf{p}'$ to be inside the magnetic Brillouin zone, the right-hand side of the second equation vanishes and the $\Psi_{\mathbf{p}\alpha}$ spinors commute in the same way as the $c_{\mathbf{p}\sigma}$ spinors. Any Hamiltonian constructed by forming singlets of the basic spinors would be manifestly $SO(5)$ symmetric.

Because of the nonanalyticity associated with the function $g(\mathbf{p})$, this class of $SO(5)$-symmetric models contains long-ranged interactions in real space. However, similar kinds of long-ranged interactions are also present in the original BCS model due to the truncation of interactions in momentum space. Therefore this class of $SO(5)$ models can be best viewed as a group of low-energy effective models resulting from integrating out states far from the Fermi surface. These models may address an important issue in the field of high-temperature superconductivity, which concerns the nature of the quasiparticle spectrum at the d-wave SC-to-AF transition. In the pure d-wave SC state, the SC order parameter is described by the form factor $d(p) = (\cos p_x - \cos p_y)$. When the system is rotated into a uniform mixed AF/SC state, the form factor of the resulting AF order parameter is given by $g(p)d(p) = |\cos p_x - \cos p_y|$, which contains nodes at the same positions as in the pure d-wave SC state. When doping is further reduced, a uniform component of the AF gap develops across the Fermi surface, filling the d-wave nodes. This uniform AF gap gradually evolves into the AF Mott insulating gap at half filling (see Fig. 22). Based on this scenario, Zacher *et al.* (2000) explained the d-wave-like dispersion of the quasiparticle in the insulating state (Ronning *et al.*, 1998). Filling the d nodes with the uniform AF gap also naturally explains the small gap observed in photoemission experiments in the lightly doped cuprates (Shen *et al.*, 2004). This theory of quasiparticle evolution is also similar to the scenario of quantum disordering the nodal quasiparticles developed by Balents *et al.* (1998, 1999), Franz, Tesanovic, and Vafek (2002), and Herbut (2002). Recent studies have found that the generalized Hubbard model for spin-3/2 fermions enjoys an exact and generic $SO(5)$ symmetry without any fine-tuning of model parameters and filling factors (Wu, Hu, and Zhang, 2003). Such a model can be accurately realized in systems of ultracold atoms on optical lattices, where the interaction is local and s-wave scattering dominates (Jaksch *et al.*, 1998; Greiner, 2002; Hofstetter *et al.*, 2002). In the Hubbard model with spin-1/2 fermions, two fermions on the same site can only form a total spin $S_T=0$ state; the $S_T=1$ state is forbidden by the Pauli principle. Therefore only one local interaction parameter specifies the on-site interaction. By a similar argument, two spin-3/2 fermions on the same site can only form the total spin $S_T=0,2$ states; the $S_T=1,3$ states are forbidden by the Pauli principle. Therefore the generalized Hubbard model for spin-3/2 fermions is given by

$$H = -t\sum_{\langle ij\rangle,\sigma}\{c^{\dagger}_{i\sigma}c_{j\sigma} + \mathrm{H.c.}\} - \mu\sum_{i\sigma} c^{\dagger}_{i\sigma}c_{i\sigma} + U_0\sum_i P^{\dagger}_0(i)P_0(i) + U_2\sum_{i,m=\pm2,\pm1,0} P^{\dagger}_{2m}(i)P_{2m}(i), \tag{83}$$

where t is the hopping integral, μ is the chemical potential, and $P^{\dagger}_0, P^{\dagger}_{2m}$ are the singlet ($S_T=0$) and quintet ($S_T=2$) pairing operators, defined as

$$P^{\dagger}_0(i)[P^{\dagger}_{20}(i)] = \frac{1}{\sqrt{2}}\{c^{\dagger}_{3/2}c^{\dagger}_{-3/2} \mp c^{\dagger}_{1/2}c^{\dagger}_{-1/2}\},$$

$$P^{\dagger}_{2,2}(i) = c^{\dagger}_{3/2}c^{\dagger}_{1/2}, \quad P^{\dagger}_{2,1}(i) = c^{\dagger}_{3/2}c^{\dagger}_{-1/2},$$

$$P^{\dagger}_{2,-1}(i) = c^{\dagger}_{1/2}c^{\dagger}_{-3/2}, \quad P^{\dagger}_{2,-2}(i) = c^{\dagger}_{-1/2}c^{\dagger}_{-3/2}. \tag{84}$$

Remarkably, this generalized Hubbard model for spin-3/2 fermions is always $SO(5)$ symmetric, without any fine-tuning of parameters and filling factors. This can be seen easily from the energy-level diagram of a single site, which contains 16 states and six energy levels for spin-3/2 fermions, as depicted in Fig. 23. The $E_{1,4,6}$ levels are nondegenerate, the degeneracy of the $E_{2,5}$ levels is fourfold, and the degeneracy of the E_3 level is fivefold. We see that, without any fine-tuning of interaction parameters, this pattern of degeneracy exactly matches the singlet, the quartet (fundamental spinor), and the quintet (fundamental vector) representations of the $SO(5)$ group. It can also be easily verified that the hopping term preserves the global $SO(5)$ symmetry. In fact, it preserves an even larger symmetry group, namely, $SO(8)$. The $SO(8)$ symmetry is always broken by interactions; however, under special circumstances, its subgroups, $SO(7)$, $SO(6)$, and $SO(5)\times SU(2)$ can be realized in addition to the generic $SO(5)$ symmetry. In this paper we focus mainly on application of the $SO(5)$ theory to the AF/SC systems. However, from the above discus-

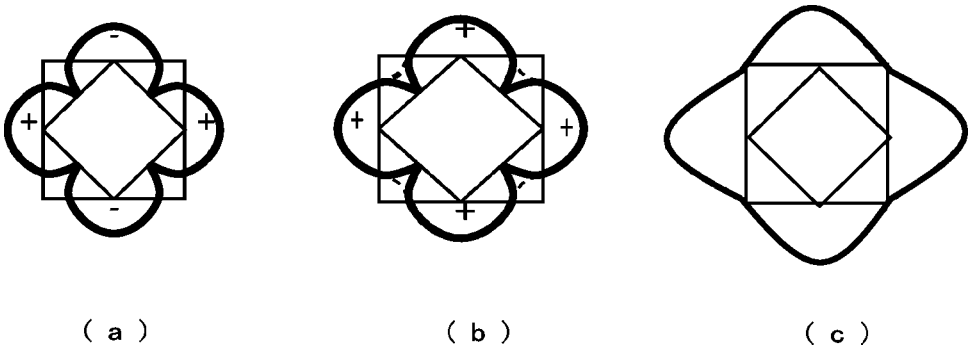

FIG. 22. Evolution of the quasiparticle states when doping is reduced: (a) pure d-wave SC gap with nodal quasiparticles; (b) the pure d-wave SC gap is rotated into an AF gap of the form $|\cos p_x - \cos p_y|$; (c) a large uniform component of the AF/Mott insulating gap is developed on top of the $|\cos p_x - \cos p_y|$ gap when doping is reduced close to zero.

sions, we can see that ultracold atoms on optical lattices also provide a fertile ground for investigating higher symmetries in strongly correlated systems, because of the higher spins of the atoms and the accuracy of the local-interaction approximation. In the case of the spin-3/2 systems, the generic $SO(5)$ symmetry makes powerful predictions on the symmetries at quantum phase-transition lines, spectrum degeneracies, topology of the ground-state manifolds, and low-energy effective theories of the Goldstone bosons. With the emerging convergence between the atomic and condensed-matter physics, we expect symmetry concepts and their multiple manifestations to play an ever-increasing role in these fields.

Fermions in exact $SO(5)$ models have a non-Abelian holonomy associated with them (Demler and Zhang, 1999a). The four components of an $SO(5)$ spinor represent four states but only two energy levels, each being doubly degenerate. As one varies some adiabatic parameters and returns to the same starting value, the states inside a doublet can be rotated into each other by a unitary transformation. This interesting mathematical property has been used to predict $SO(5)$ generalization of the Andreev effect and the non-Abelian Aharonov-Bohm effect (Demler and Zhang, 1999a).

B. Variational wave functions

In this section we shall discuss a crucial test of the $SO(5)$ symmetry by investigating the microscopic wave functions of the t-J model. In Sec. IV.A, we showed that the transition from the AF state at half filling to a pure d-wave SC state away from half filling can generally be classified into three types. Within the general form of the static potential as given in Eq. (59), the type-1 first-order transition is realized for $u_{12}^2 > u_1 u_2$. For $u_{12}^2 < u_1 u_2$, the type-2 transition involves two second-order transitions with an intermediate mixed phase in which the AF and the d-wave SC order coexist uniformly. Only for $u_{12}^2 = u_1 u_2$ is an intermediate type-1.5 transition realized, in which the potential can be rescaled to take an $SO(5)$-symmetric form and a smooth rotation between the AF and the d-wave SC states is possible. If we investigate only states with uniform densities, these three possibilities can be distinguished easily by the curvature in the plot of the ground-state energy as a function of doping δ. The curvature would be negative (concave), positive (convex), or zero (flat) for these three possibilities, as shown in Fig. 9. In the concave case, the uniform phase would be thermodynamically unstable, and a Maxwell's construction leads to a phase-separated ground state, in which each phase has a distinct density.

This interesting prediction can be tested numerically in the t-J model. At this moment, exact diagonalization of the t-J model with large system size is not possible due to the exponential growth of the Hilbert space, and reliable Monte Carlo simulation cannot be carried out due to the fermion minus-sign problem. A successful method employs the variational quantum Monte Carlo method (see, in particular, Gros, 1989; Himeda and Ogata, 1999; Calandra and Sorella, 2000; Anderson *et al.*, 2003, and references therein). Historically, the variational quantum Monte Carlo method was first used to investigate the resonating valence bond type of variational wave function proposed by Anderson (1987). By

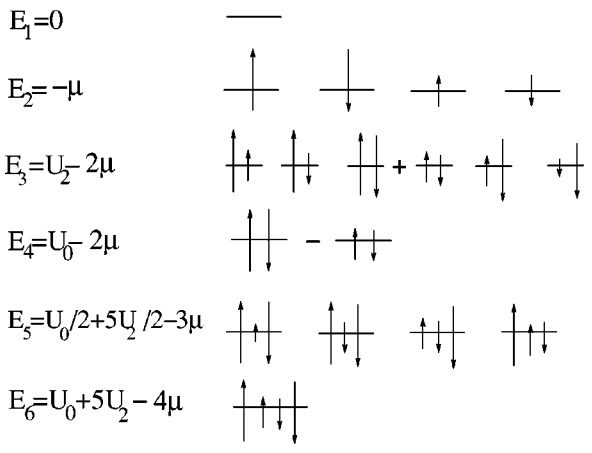

FIG. 23. Eigenstates of the spin 3/2 problem on a single site. The longer (shorter) arrows denote $S_z = 3/2$ (1/2) and the up (down) directions denote the + (−) sign. The $E1,4,6$ (singlet), $E2,5$ (quartet), and $E3$ (quintet) sets can also be classified as $SO(5)$ singlet, spinor, and vector representations.

investigating various variational wave functions, this method can address the issue of d-wave pairing in the ground state and the possibility of a uniform mixed phase with AF and d-wave SC order for the 2D t-J model.

The first question is whether the uniform mixed state has a lower energy than the pure d-wave SC or AF state near half filling. In earlier work by Zhang *et al.* (1988) and by Yokoyama and Ogata (1996), it was shown that the Gutzwiller approximation gives a reliable estimate for the variational energies for the pure d-wave SC state. However, if the AF order parameter is taken into account in the Gutzwiller approximation, there exists no region in the phase diagram where the AF state is stabilized. On the other hand, Himeda and Ogata (1999) showed that when the variational parameters Δ_d, Δ_{AF}, and μ were determined from a variational Monte Carlo simulation, in which the double occupancy prohibition is rigorously treated, then the Gutzwiller-projected trial wave function of the uniform mixed state has a lower energy than the pure d-wave SC state with $\Delta_{\mathrm{AF}}=0$, in the doping range $0<\delta<10\%$. Using Green's-function Monte Carlo with stochastic reconfiguration, Calandra and Sorella (2000) also concluded that the AF correlation coexists with SC and persists up to $\delta=10\%$. Himeda and Ogata used the following Gutzwiller projected trial wave function:

$$|\psi\rangle = P_G|\psi_0(\Delta_d,\Delta_{\mathrm{AF}},\mu)\rangle, \tag{85}$$

where Δ_d, Δ_{AF}, and μ are the variational parameters relating to d-wave SC and AF orders and μ is the chemical potential. $P_G=\Pi_i(1-\hat{n}_{i\uparrow}\hat{n}_{i\downarrow})$ stands for the Gutzwiller projection operator. The wave function $|\psi_0(\Delta_d,\Delta_{\mathrm{AF}},\mu)\rangle$ is a mixed BCS/spin-density-wave function, i.e.,

$$|\psi_0(\Delta_d,\Delta_{\mathrm{AF}},\mu)\rangle = \prod_{k,s(=\pm)} (u_k^{(s)} + v_k^{(s)} d_{k\uparrow}^{(s)\dagger} d_{-k\downarrow}^{(s)\dagger})|0\rangle, \tag{86}$$

where the index $s=\{\pm\}$ takes care of the electron operators acting on the $A(B)$ sublattice in the AF state. The u_k's and v_k's contain the variational parameters Δ_d, Δ_{AF}, and μ and are defined in detail by Himeda and Ogata (1999). Figure 24 is reproduced from their paper and plots the ground-state energy and the staggered magnetization as a function of doping δ.

We see that in the Himeda and Ogata variational quantum Monte Carlo work the uniform mixed phase of the AF and d-wave SC phases has a lower energy than the pure d-wave SC state up to a doping of about 10%. At half filling, the energy was found to be close to the best estimated value in the Green's-function Monte Carlo method (−0.1994 to −0.200 76), which provides support for the wave-function ansatz equation (86).

The second point of interest is that, according to the Himada and Ogata results in Fig. 24, the ground-state energy is a linear function of doping δ in this region, with essentially zero curvature. This implies that the chemical potential μ is constant. Since the wave function of Himada and Ogata describes a mixed state with uniform density, the energy-versus-doping plot can generally have three distinct possibilities, as enumerated in Fig. 9. Therefore, from the fact that the curvature is nearly flat, we determine that the condition $u_{12}^2=u_1u_2$ is fulfilled, which places the t-J model at $J/t=0.3$ into the domain of attraction of the $SO(5)$ fixed point (Arrigoni and Hanke, 2000; Murakami and Nagaosa, 2000).

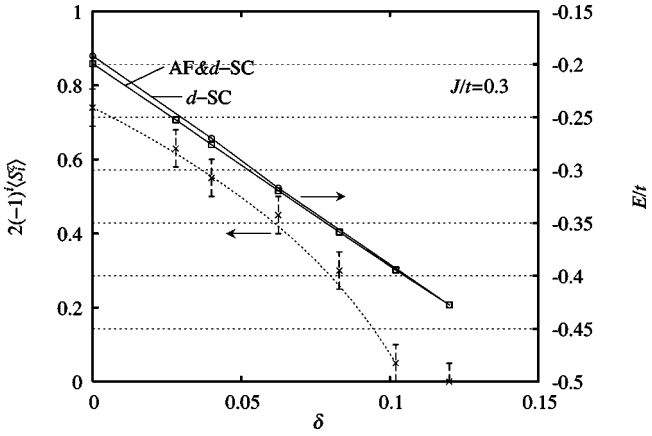

FIG. 24. Doping dependence of the ground-state energy (two upper curves) and staggered magnetization (lower curve) for the t-J model with $J/t=0.3$. The state with uniform AF and d-wave SC order has lower energy than the pure d-wave SC state for $0<\delta<10\%$; furthermore, the energy of the uniform AF/SC mixed state depends linearly on δ, fitting into the $SO(5)$-symmetric type-1.5 transition classified in Fig. 9. From Himeda and Ogata, 1999.

C. Exact diagonalization of the *t*-*J* and Hubbard models

In the previous section we discussed the test of the $SO(5)$ symmetry through the variational wave functions in the t-J model. In this section, we shall describe numerical calculations of the dynamic correlation functions and the exact diagonalization of the spectrum, which also tests the $SO(5)$ symmetry of the microscopic t-J and Hubbard models. A microscopic model has a symmetry if its generators G commute with the Hamiltonian H, i.e., $[H,G]=0$. In the $SO(5)$ theory, the π_α operators are the nontrivial generators of the symmetry. In models constructed in Sec. V.A, the π_α operators indeed commute with the Hamiltonian. However, there are models in which the symmetry generators do not commute with the Hamiltonian but satisfy a weaker condition, $[H,G^\pm]=\pm\lambda G^\pm$, where λ is a c-number eigenvalue [see, e.g., Eq. (13) in Sec. II]. These operators are called eigenoperators of the Hamiltonian. In this case, from one eigenstate of the Hamiltonian, one can still generate a multiplet of eigenstates by the repeated actions of $G^\pm$. However, the eigenstates within a multiplet are not degenerate, but their energies are equally spaced by λ. A classic example is the precession of a spin in a magnetic field, where

$$H=\omega_0 S_z; \quad [H,S_\pm]=\pm\omega_0 S_\pm \tag{87}$$

and ω_0 is the Lamor frequency of the spin precession. Although in this case the spin rotational symmetry is broken explicitly by the magnetic field in the z direction and the eigenstates within the multiplets are no longer degenerate, the multiplet structure of the symmetry is still visible in the spectrum and can be sampled by the ladder operators. If one calculates the dynamical response function of $S_\pm$, only a single δ peak is present at $\omega=\omega_0$.

The π_α operators defined in Eq. (28) do not commute with the Hubbard or *t-J* model Hamiltonian, but analytical and numerical calculations show that they are approximate eigenoperators of these model, in the sense that

$$[H,\pi_\alpha^\dagger]\approx\omega_\pi\pi_\alpha^\dagger \tag{88}$$

is satisfied in the low-energy sector. This means that the dynamic autocorrelation function of the π_α operators contains a sharp pole at ω_π, with broad spectral weight possibly distributed at higher energies. Using a *T*-matrix approximation, Demler and Zhang (1995) verified this approximate equation with $\omega_\pi=J(1-n)/2-2\mu$. This calculation will be reviewed in Sec. VI.D. The first numerical test for a low-energy *SO*(5) symmetry in a microscopic model has been performed by Meixner *et al.* (1997) using the Lanczos (1950) exact diagonalization technique. The analysis presented in their paper showed that the dynamical correlation function of the π operator,

$$\pi_\alpha^\dagger(\omega)=-\frac{1}{\pi}\,\mathrm{Im}\langle\Psi_0^N|\pi_\alpha\frac{1}{\omega-H+E_0^{N+2}+i\eta}\pi_\alpha^\dagger|\Psi_0^N\rangle, \tag{89}$$

where H is the standard Hubbard Hamiltonian, $|\Psi_0^N\rangle$ its ground state with N electrons, and E_0^N the corresponding ground-state energy, yielded a single sharp excitation peak at low-energy ω_π, accompanied by an incoherent background at higher energies. The large separation between the peak and the continuum and the large relative spectral weight of the peak demonstrated that indeed the π operator is an *approximate* eigenoperator of the Hamiltonian (see Fig. 25). Also in accordance with the perturbative result of Demler and Zhang (1995), the precession frequency ω_π decreases for decreased doping. Furthermore, a comparison with a bubble approximation for this correlation function showed that the sharp peak near ω_π originated solely from vertex corrections (i.e., collective behavior).

Not only can the dynamic correlation function of the π_α operators (89) be measured numerically for microscopic models, thus providing a test of the approximate *SO*(5) symmetry, but they can also be directly measured in neutron-scattering experiments in the SC state. We shall discuss these experiments in Sec. VI.

Exact numerical diagonalization of the *t-J* and Hubbard models gives eigenstates and eigenvalues on a finite-size cluster, whose degeneracy pattern can be used directly to test the *SO*(5) symmetry. In order to explain the main idea, let us first examine the variational wave function of the projected *SO*(5) model given in Eq. (55). This wave function describes a broken-symmetry state formed by a linear superposition of states with different spin or charge quantum numbers. This type of state can only be realized in infinite systems. On a finite-size system, all eigenstates must have definite spin and charge quantum numbers. Denoting $t^\dagger(x)=m_\alpha(x)t_\alpha^\dagger(x)+\Delta(x)t_h^\dagger(x)$, we can expand the coherent state described by Eq. (55) as

$$|\Psi\rangle=\Big(\cos\theta^N+\cos\theta^{N-1}\sin\theta\sum_x t^\dagger(x)+\cos\theta^{N-2}\sin\theta^2\sum_{x\neq y}t^\dagger(x)t^\dagger(y)+\cos\theta^{N-3}\sin\theta^3\sum_{x\neq y\neq z}t^\dagger(x)t^\dagger(y)t^\dagger(z)+\cdots\Big). \tag{90}$$

For $\Delta(x)=0$, we see that the AF-ordered state can be expressed as a linear superposition of states with different numbers of magnons, forming states with different total spins. While states with different total spins are separated by finite energy gaps in a finite-size system, these energy gaps could vanish in the thermodynamic limit, allowing magnons to "condense" into the ground state. For $m_\alpha(x)=0$, we see that the SC state can be expressed as a linear superposition of states with different numbers of hole pairs, with different total charge. A

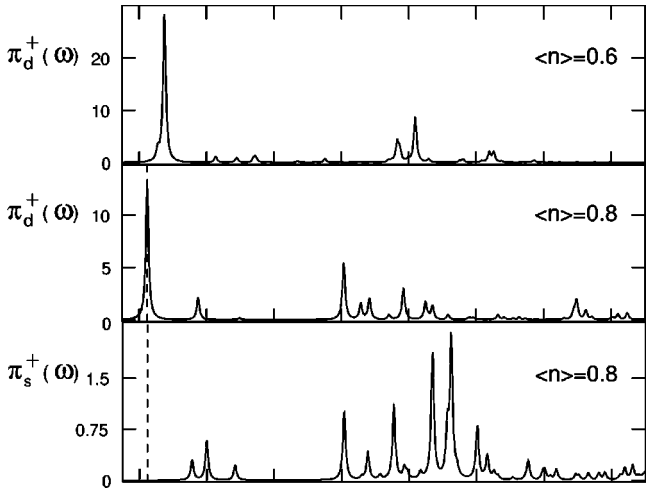

FIG. 25. Exact diagonalization results for the dynamical correlation function of the π operator on a 10-site Hubbard system with $U=8t$. A single δ-function-like peak with pronounced weight is visible near $\omega=0$ for the π operator, proving the eigenoperator relation (88) in the low-energy regime. This precession frequency ω_π decreases with decreasing doping. An alternatively constructed *s*-wave π operator, with $g(p)$ in Eq. (28) given by $g(p)=\cos p_x+\cos p_y$, shown in the bottom graph exhibits only incoherent behavior and hardly any weight (note the difference in the y scale). Here $\langle n\rangle$ denotes average electron density, with $\langle n\rangle=1$ being at half filling. From Meixner *et al.*, 1997.

smooth rotation from the AF state to the SC state becomes possible if one can freely replace each magnon by a hole pair without energy cost. This places a powerful requirement on the spectrum. The $\Sigma_x t^\dagger(x)|\Omega\rangle$ term in Eq. (90) contains a single magnon state with $(S=1, Q=0)$ or a single hole-pair state with $(S=0, Q=-1)$. $SO(5)$ symmetry requires them to be degenerate. This can be easily achieved by tuning the chemical potential, which changes the energy of the hole-pair state without changing the energy of the magnon state. Once the chemical potential is fixed, there are no additional tuning parameters. The $\Sigma_{x\neq y} t^\dagger(x)t^\dagger(y)|\Omega\rangle$ term in Eq. (90) contains a two-magnon state with $(S=2, Q=0)$, a one-magnon/one-hole-pair state with $(S=1, Q=-1)$, and a two-hole-pair state with $(S=0, Q=-2)$. $SO(5)$ symmetry again requires them to be degenerate, which is a highly nontrivial test. We can easily perform this analysis for states with different numbers of magnons and hole pairs.

This pattern of the energy levels has been tested directly in the exact diagonalization of the t-J model by Eder, Hanke, and Zhang (1998). The t-J model, because of its more limited Hilbert space (no double occupancies), allows the exact diagonalization of larger systems (18, 20, and more sites). Since the t-J model explicitly projects out the states in the upper Hubbard band, some of the questions about the compatibility between the Mott-Hubbard gap and $SO(5)$ symmetry can also be answered explicitly. In exact diagonalization studies, total energy, momentum, angular momentum, spin, and the charge quantum numbers of the low-energy states can be determined explicitly. These quantum numbers are summarized in Fig. 26(a).

Eigenstates obtained from the t-J or Hubbard Hamiltonian can always be interpreted as multiparticle states of the underlying electron. However, it would be highly nontrivial if the low-energy states could also be interpreted as multiparticle states formed from the collective degrees of freedom such as the magnons and the hole pairs. The first finding of Eder *et al.* (1998) is that this is indeed the case. Figure 27 shows the first four ($\nu=0$ to $\nu=3$) sets of low-lying states of an 18-site t-J model (Eder *et al.*, 1998). We see that the lowest-energy state in the $S=1$, $Q=0$ sector indeed has s-wave-like rotational symmetry and total momentum (π,π), as expected from a magnon; the lowest-energy state in the $S=0$, $Q=-1$ sector indeed has a d-wave-like rotational symmetry and total momentum 0. Similarly, states with higher S and Q have quantum numbers expected from multiple magnons and hole pairs. This finding confirms the basic assumption of the $SO(5)$ theory, that the low-energy collective degrees of freedom can be described by the superspin alone.

At the next level, the pattern of symmetry can itself be tested. The level ν of a given multiplet indicates the total number of magnons and hole pairs. If $SO(5)$ symmetry is realized at a given chemical potential μ_c, we would expect the free energy to depend only on ν, the total number of magnons and hole pairs, but not on the difference between the number of magnons and hole pairs. As shown in Fig. 26, the energy can depend on Q with three generic possibilities, as in the discussions we presented in Sec. IV.A and Fig. 9. Only when the energy depends linearly on Q can the free energy be independent of Q at a given critical value of the chemical potential. From Eq. (27) we see that the energy levels indeed have this remarkable structure: states whose total charges differ by $\Delta Q=-1$ have nearly the same difference in energy. Therefore the energy is approximately a linear function of Q or doping, similar to the situation discussed in Sec. V.B. To be more precise, the mean level spacing within each multiplet (up to $Q=-2$) is -2.9886 with a standard deviation of 0.0769. This standard deviation is much smaller ($\sim J/8$) than the natural energy scale J of the t-J model and comparable to or even smaller than the average SC gap. If one now adds the chemical-potential term $H_\mu=-2\mu Q$ and chooses $\mu=\mu_c$ equal to the mean level spacing, the superspin multiplets are nearly degenerate. At $\mu=\mu_c$, magnons can be smoothly converted into hole pairs without free-energy cost. This means that in each term of the expansion in Eq. (90) one can freely substitute $t_\alpha^\dagger$ or $t_h^\dagger$ for $t^\dagger$, and the direction of the superspin vector can be freely rotated from the AF to the SC direction. The smallness of the standard deviation indicates the flatness in the energy-versus-doping plot discussed in the previous section. If the standard deviation were significantly different from zero, this would indicate significant curvature in the energy-versus-doping plot. Therefore the smallness of the standard deviation obtained by the exact diagonalization is consistent with the flatness of the energy-versus-doping plot obtained from the variational wave function discussed in the previous section.

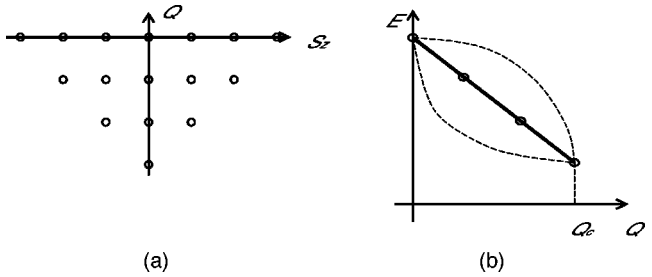

FIG. 26. The magnon and hole-pair states obtained at level ν, which is the total number of magnons and hole pairs, after expanding out the coherent state (55). These states are classified by their (S_z, Q) quantum numbers in (a). The energy is independent of the S_z quantum number because of the $SO(3)$ spin rotation symmetry. The energy can depend on Q with three generic possibilities, as depicted in (b). (Compare with Fig. 9.) If the energy depends linearly on Q, there is no free-energy cost to rotate magnons and hole pairs into each other, and the potential energy is $SO(5)$ symmetric. This multiplet structure was tested in the t-J model and is shown in Fig. 27.

Another important aspect of the $SO(5)$ symmetry is the Wigner-Eckart theorem (Georgi, 1982). This theorem provides a selection rule for the matrix elements of the operators based on the $SO(5)$ symmetry of the system. It implies, for example, that the π operators [see

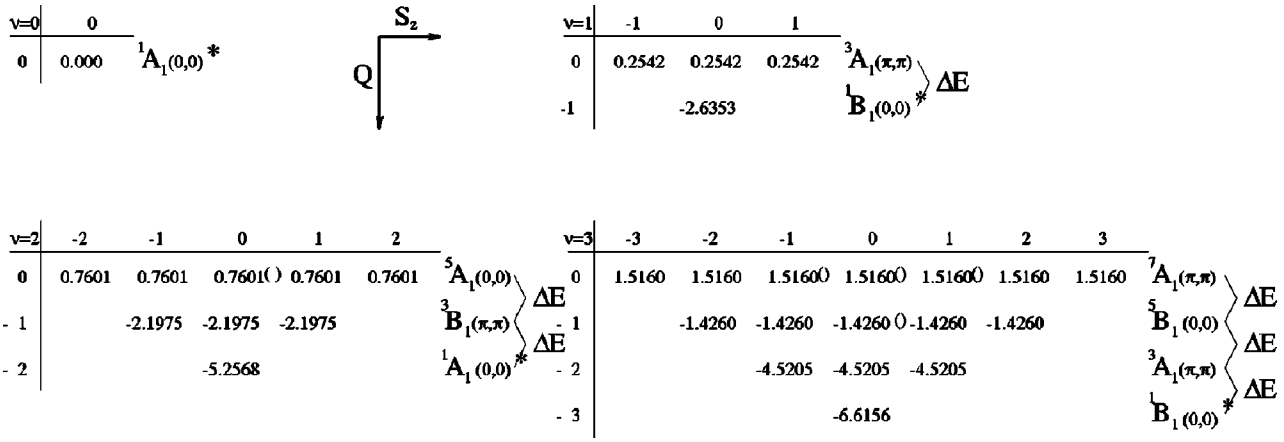

FIG. 27. The low-energy states within each total spin and charge sector (S_z, Q) of the 18-site cluster t-J model with $J/t=0.5$. The states are grouped into different multiplets and are labeled by spin, charge, point-group symmetry, and total momentum. A_1 denotes the totally symmetric representation and B_1 the $d_{x^2-y^2}$-like representation of the C_{4v} symmetry group. The quantum numbers of these states match those of the magnon and hole-pair states shown in Fig. 26. Furthermore, the energy depends approximately linearly on Q, demonstrating the $SO(5)$ symmetry of the interaction potential among the magnons and hole pairs.

Eq. (28)] can only move us within a given multiplet, since they are symmetry generators. On the other hand, AF and d-wave SC order parameters [see Eq. (26)] should move us between different multiplets. Both features have been verified in the numerical calculations of Eder *et al.* (1998).

We conclude this subsection with a general remark. Exact diagonalizations (e.g., those of Dagotto, 1994) commonly study ground-state correlations, but their spatial decay is often inconclusive as a test of order due to small system size. Discussions in this section show that it is possible that the (excited) eigenstates reveal a well-defined structure characteristic of a particular symmetry. Our strategy is to use the finite-size calculations as input for effective models describing the collective degrees of freedom such as the superspin, or the magnons and the hole pairs. Since quantum Monte Carlo calculations can be performed for these models in a large-size system, the question of long-range order and their competition can be firmly established.

D. Transformation from the microscopic model to effective *SO*(5) models

From the two previous sections we have learned that both the variational wave function and the exact diagonalization of the t-J model show that the ground state and low-lying excited states in the low-doping range can be completely described in terms of the superspin degree of freedom, with an approximate $SO(5)$ symmetry. Altman and Auerbach (2002) pioneered a systematic procedure in which they derived the effective bosonic $SO(5)$ model directly from the microscopic Hubbard and t-J models through a renormalization-group transformation called the contractor renormalization (CORE) method (Morningstar and Weinstein, 1996). This mapping has several distinct advantages. First, this approach helps to visualize clearly which processes and which excitations dominate the low-energy physics of the system. Second, it directly determines the parameters of the effective models defined in Eqs. (50) and (65) in terms of the microscopic parameters. The bosonic systems are often much easier to analyze numerically, as one does not have to worry about Pauli principles, Slater determinants, and the infamous sign problem in the quantum Monte Carlo algorithms. In this section, we shall describe the work of Altman and Auerbach.

Since we want to construct *bosonic* quasiparticles, we have to divide the lattice into effective sites containing an even number of elementary sites (with one electron per site). In order to conserve the symmetry between the x and y directions in the system, the original projected $SO(5)$ model is formulated on a plaquette of 2×2 elementary sites. First we begin with the low-energy eigenstates of the Heisenberg plaquette, which are determined easily. We find the nondegenerate ground state $|\Omega\rangle$ (see Fig. 6 for a real-space representation in terms of the microscopic states on a plaquette) with energy $E_0=-2J$ and total spin $S=0$. This singlet state will be the vacuum state of the effective bosonic projected $SO(5)$ model. The next energy eigenstates are three triplet states $t_\alpha^\dagger|\Omega\rangle$ with energy $E_t=-J$ and spin quantum numbers of $S=1$. All other energy eigenstates of the Heisenberg plaquette have higher energies and can be neglected in the low-energy effective model. It should be noted that the quasiparticles t_α, which carry spin 1 and charge 0, are hard-core bosons because one cannot create more than one of them simultaneously on a single plaquette.

In their CORE study of the 2D Hubbard model, Altman and Auerbach (2000) started from the spectrum of lowest-energy eigenstates of the 2×2 plaquette for 0, 1, and 2 holes, respectively. The corresponding lowest spectrum of the triplet $(t_\alpha^\dagger)$, pair boson $(t_h^\dagger)$, and fermionic excitations is presented in Fig. 28. The ground state of two holes, also depicted in Fig. 6, is described by

$$t_h^\dagger|\Omega\rangle = \frac{1}{\sqrt{Z_b}}\left(\sum_{ij} d_{ij} c_{i\uparrow} c_{j\downarrow} + \cdots\right)|\Omega\rangle, \tag{91}$$

where d_{ji} is +1 (−1) on vertical (horizontal) bonds within a plaquette and "⋯" stands for higher-order (U/t) operators. Z_b is the wave-function normalization. We note that $t_h^\dagger$ creates a Cooper-like hole pair with internal d-wave symmetry with respect to the vacuum. The crucial point here is that while there is no hole-pair binding for the Hubbard model on a dimer, there is binding in the range of $U/t \in (0,5)$ for a plaquette, a rather well-known fact (see, for instance, Hirsch *et al.*, 1988). However, this does not guarantee the integrity of the pair binding on the infinite lattice, documented by the fact that the hopping energy t is much larger than the pair binding energy, nor does it guarantee long-range SC order. To gain more insight into these questions, one has to construct H_{eff} via a CORE procedure (see Fig. 29).

In order to understand how the triplets and pair bosons behave on an infinite lattice, we must determine the boson hopping energies and the corresponding effective Hamiltonian. A suitable approach for this has been suggested by Morningstar and Weinstein on the basis of the CORE technique, which has been shown for the 2D Hubbard model (Altman and Auerbach, 2002), *t-J* ladders (Capponi and Poilblanc, 2002), and earlier for Heisenberg chains and ladders (Morningstar and Weinstein, 1996) to be extremely accurate. For example, Morningstar and Weinstein obtained a very accurate 1D Heisenberg-model ground-state energy. This is even more impressive considering the latter model has long-range, power-law decaying spin correlations.

In order to implement the CORE technique, the lattice is decomposed into small block units, as shown in Fig. 30, where H_0 is the intrablock Hamiltonian and V is the part describing the coupling between the two neighboring blocks. The M low-energy states $\{|\alpha^0\rangle\}_i^M$ are kept in each block i (here $M=4$ in the 2×2 plaquette i) to define a reduced Hilbert space. The full Hamiltonian is then diagonalized on N connected units (in our example in Fig. 30, $N=2$), i.e., for the (superblock) Hamiltonian H_S. The M^N (in our case, $M^N=4^2$) lowest-energy states $|\Psi_n\rangle$ with energy ϵ_n, $n=1\cdots M^N$ are retained. These true eigenstates of the $N(=2)$ block problem, $\{|\Psi_n\rangle\}$, are then projected onto the reduced Hilbert space spanned by the tensorial product $|\alpha_1^0\cdots\alpha_N^0\rangle$ of the $M(=4)$ states of each block, i.e.,

$$|\Psi_n'\rangle = \sum_{\alpha_1\cdots\alpha_N} \langle\alpha_1^0\cdots\alpha_N^0\,|\Psi_n\rangle|\alpha_1^0\cdots\alpha_N^0\rangle, \tag{92}$$

and Gram-Schmidt orthonormalized, finally yielding the states $\{|\tilde{\Psi}_n\rangle\}$. Then, the new superblock (renormalized) Hamiltonian is defined as

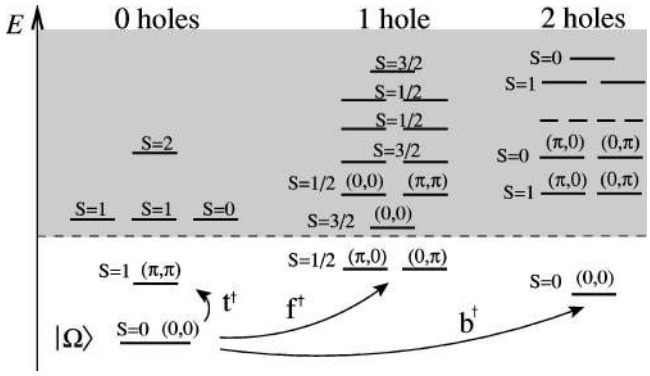

FIG. 28. Low-energy spectrum of the Hubbard model on a plaquette. Eigenstates are labeled by total spin S and plaquette momentum $q_x,q_y=0,\pi$. Truncated high-energy states are shaded. The vacuum is defined as $|\Omega\rangle$, and quantized operators connect the vacuum to the lowest eigenstates as shown. (In this figure, $t^\dagger$ denotes the magnon creation operator $t_\alpha^\dagger$, and $b^\dagger$ denotes the hole-pair creation operator $t_h^\dagger$.)

$$\tilde{H}_S = \sum_n^{M^N} \epsilon_n |\tilde{\Psi}_n\rangle\langle\tilde{\Psi}_n|. \tag{93}$$

By construction $\tilde{H}_S$ has the same eigenvalues ϵ_n as H_S for $n=1,\ldots,M^N$. Having constructed the new superblock or renormalized Hamitonian $\tilde{H}_S$, one can write (in our $N=2$ example)

$$\tilde{H}_S = \tilde{H}_0 \otimes \mathrm{I} + \mathrm{I} \otimes \tilde{H}_0 + \tilde{V}, \tag{94}$$

where $\tilde{H}_0$ is simply the projected block Hamiltonian:

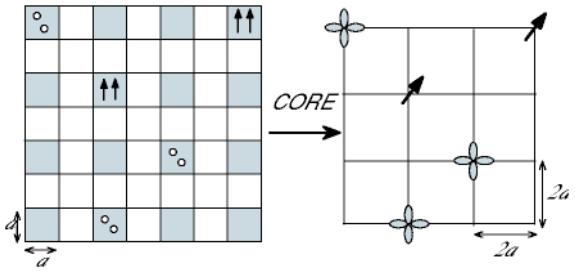

FIG. 29. Illustration of the basic idea of the contractor renormalization-group (CORE) method. To implement this method, one first decomposes the original lattice in plaquettes, and then truncates the spectrum of a given plaquette to the five lowest states, i.e., singlet, hole-pair, and three magnon states. An effective Hamiltonian for these bosons can then be calculated using the CORE method. Left: local bosons in the original lattice. Gray rectangle denotes the singlet RVB vacua, circles denote holes, and the sets of two parallel vertical arrows denote magnons. Right: local bosons on the lattice of the plaquette. Leaf-like pattern denotes a local d-wave hole pair on a plaquette. Canted arrows denote local magnons on the plaquette. The singlet RVB vacuum is denoted by an empty site.

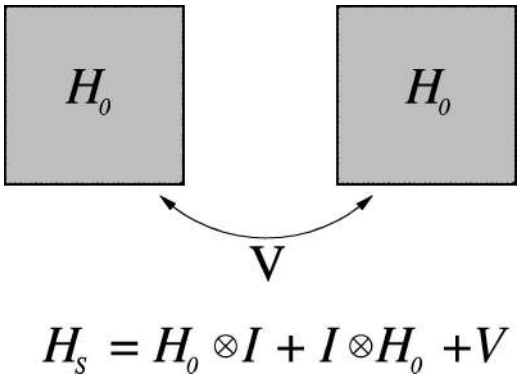

FIG. 30. This figure illustrates the construction of a "superblock" and its Hamiltonian H_s out of two neighboring blocks, with intrablock Hamiltonian H_0 and interblock coupling V (in the block basis: $(H_0)_{n,n'}=\langle\alpha_n^o|H|\alpha_{n'}^o\rangle=\epsilon_n^o\delta_{n,n'}$ and $(V_0)_{nm,n'm'}=\langle\alpha_n^o\alpha_m^o|V|\alpha_{n'}^o,\alpha_{m'}^o\rangle$).

$$\tilde{H}_0=\sum_{n=1}^{M}\epsilon_n|\alpha_n^0\rangle\langle\alpha_n^0|. \tag{95}$$

The above equation (94) gives the new renormalized interblock coupling $\tilde{V}$, restricted to the reduced Hilbert space. In the next step, one repeats the above procedure, replacing H_0 and V in the original superblock Hamiltonian H_S by $\tilde{H}_0$ and $\tilde{V}$, and so on.

The projection onto the original plaquette product basis in Eq. (92) expresses, of course, the above-discussed proliferation and possibly spatial decay of the block excitations. More generally, this is incorporated within the CORE method, in a superblock consisting of N blocks and a corresponding Hamiltonian containing N-body interactions. The construction to obtain $\tilde{V}$ [Eq. (94)] is different and, obviously, one also obtains $\tilde{V}$ terms, connecting N clusters instead of just $N=2$ (called the *range-N approximation*). It has been shown in the above-cited various applications that the above range-2 approximation ($N=2$) and at most $N=3$ interactions already yield very accurate results. Thus, with a proper and physically motivated choice of the truncated basis, range-N interactions decay rapidly with N.

Altman and Auerbach (2002) limited their CORE calculation to range-2 boson interactions (triplets, hole-pair boson) leaving out the fermion state. From Fig. 30, it is clear that this amounts to diagonalizing two coupled (2×2) plaquettes, for instance, an eight-site Hubbard cluster, which is very straightforward by the Lanczos technique. The resulting effective Hamiltonian for this range-2 four-boson model is exactly the projected $SO(5)$ model defined in Eq. (50) plus more extended interactions defined in Eq. (65). Following Altman and Auerbach, we compare in Fig. 31 the magnitudes of the magnon hopping J_s (denoted as $J_t/2\simeq J_{tt}/2$ by Altman and Auerbach, 2002) and the hole-pair hopping J_c (denoted as J_b by Altman and Auerbach) for a range of (U/t) values.

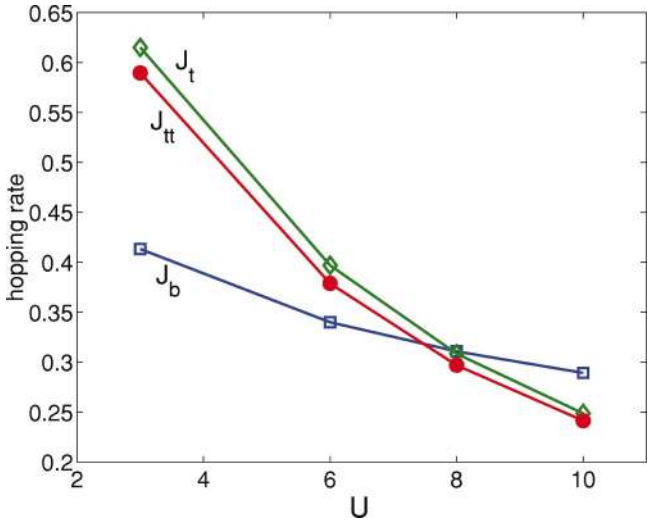

FIG. 31. (Color) Boson hopping energies vs Hubbard U. The intersection region near $U=8$ is close to the projected $SO(5)$ symmetry point. All energies are in units of t.

The first observation is that $J_t\sim J_{tt}\sim 0.6J$; therefore the triplet terms have a similar magnitude to those obtained previously (Sachdev and Bhatt, 1990; Gopalan *et al.*, 1994).

The second finding is crucial. The region of equal J_t (J_{tt}) and J_b, equal magnon and pair-boson hopping, occurs very close to $U/t=8$. Thus the value of the projected $SO(5)$ model with $J_t=J_b$ occurs in the physically relevant regime. It is known from a large body of numerically essentially exact evaluations of the 2D Hubbard model that it reproduces the salient features of the high-T_c cuprates precisely in this regime (see, for example, Dagotto, 1994; Imada *et al.*, 1998). This gives yet another piece of evidence, in addition to those discussed in Secs. V.B and V.C, that realistic microscopic models can be described effectively by the projected $SO(5)$ model close to the symmetric point.

Altman and Auerbach (2002) and Capponi and Poilblanc (2002) also calculated the coefficient and terms on H^{int} in Eq. (65), which contains triplet-triplet, pair-pair, and pair-triplet interactions. These interaction terms were found to be small compared to H^b and H^t, but their influence has yet to be studied in detail. They also estimated the truncation error of discarding range-3 terms, which, for physically relevant U values, was found to be very small (1%).

An issue still left open is the role of fermions. Altman and Auerbach have extended the above four-boson model to a boson-fermion model by augmenting the bosons with single-hole fermions "by hand." This is certainly a first step. However, a consistent low-energy theory has to treat bosons and fermions within the CORE procedure on an equal footing. It should be noted that the short-range effects of the fermions on the effective boson couplings were included in the above range-2 calculation. Altman and Auerbach estimated the fermion-boson interaction by including the hole fermions dispersion *ad hoc*, i.e., using the single-hole band

structure extracted previously by various groups for large clusters (Dagotto, 1994).

In summary, the application of the CORE algorithm to the Hubbard model has demonstrated two features that are of immediate relevance for the $SO(5)$ theory: the d-wave hole pairs already present in the 2D Hubbard model on a single 2×2 plaquette maintain their integrity in the infinite square lattice. The low-energy degrees of freedom are indeed described solely by the superspin. Second, the hole-pair and magnon (triplet) hopping fulfills the projected $SO(5)$ condition in the physically relevant (U/t) range.

VI. PHYSICS OF THE π RESONANCE AND THE MICROSCOPIC MECHANISM OF SUPERCONDUCTIVITY

A key experimental manifestation of a higher symmetry is the emergence of new particles or new collective modes. Historically, this line of reasoning has led to important discoveries in particle physics. For example, Gell-Mann used the $SU(3)$ symmetry of the strong interaction to predict the Ω^- resonance. Similarly, the electroweak unification based on the $SU(2)\times U(1)$ symmetry led to the prediction of the $W^{\pm}$ and the Z bosons. In a strongly interacting system, whether in particle physics or in condensed-matter physics, typical excitations have short lifetimes and broad line shapes. However, if higher symmetries are present, the selection rules associated with the symmetry prevent the excitation from decaying. The $SO(5)$ symmetry of antiferromagnetism and superconductivity naturally predicts a new class of collective excitations, called the π resonance or π mode for short, which are the (pseudo-)Goldstone modes of spontaneous symmetry breaking. The π resonance can be identified naturally with the neutron resonance observed in the high-T_c cuprates (Rossat-Mignod, Regnault, Vettier, Bourges, *et al.*, 1991; Mook *et al.*, 1993; Fong *et al.*, 1995). In this section we shall review basic experimental facts about such resonances and discuss a theoretical scenario in which they originate from the pseudo-Goldstone modes associated with the $SO(5)$ symmetry. The operator of the π mode is a symmetry generator of the $SO(5)$ symmetry, so the appearance of a low-lying resonance signals a small energy difference between the d-wave SC and AF ground states of the doped cuprates. The idea of the near degeneracy of the d-wave SC and AF states lies at the heart of the $SO(5)$ approach, which assumes that fluctuations between these two states exhaust the low-energy sector of the system. Hence experimental observation of the low-lying resonances provide a key foundation to the $SO(5)$ approach to competing AF and SC in the cuprates. In this section we provide several perspectives on the π excitations. First, we use the $SO(5)$ nonlinear sigma model to describe them as pseudo-Goldstone modes of the approximate $SO(5)$ symmetry of the system. Second, we show that Fermi-liquid analysis of the weakly interacting electron gas in a two-dimensional tight-binding lattice produces the π mode as a sharp collective mode and gives a simple picture of this excitation as an antibound state of two electrons with the total spin $S=1$ and with the center of mass momentum $\Pi=(\pi,\pi)$. Such excitation contributes to the spin-fluctuation spectrum, measured by the inelastic neutron scattering, only in the SC state when there is a condensate of Cooper pairs. Finally, we discuss an important role that the π resonance plays in stabilizing the SC state.

A. Key experimental facts

A resonant peak in the SC state of the cuprates was first observed in optimally doped $YBa_2Cu_3O_7$ (Rossat-Mignod, Regnault, Vettier, Bourges, *et al.*, 1991; Rossat-Mignod, Regnault, Vettier, Burlet, *et al.*, 1991; Rossat-Mignod *et al.*, 1992). Further experiments (Mook *et al.*, 1993; Fong *et al.*, 1995) established that this is a magnetic resonance (spin $S=1$) at the AF wave vector $\Pi=(\pi,\pi)$, which appears in the SC state. It has a constant energy $\omega_0=41$ meV at all temperatures and an intensity that is strongly temperature dependent and vanishes at T_c. Similar resonances were then found in underdoped $YBa_2Cu_3O_{6+x}$ (Dai *et al.*, 1996, 1998; Fong *et al.*, 1996, 2000; Mook *et al.*, 1998; Stock *et al.*, 2003), in $Bi_2Sr_2CaCu_2O_{8+\delta}$ (Fong *et al.*, 1999; He *et al.*, 2001), and $Tl_2Ba_2CuO_{6+\delta}$ (He *et al.*, 2002).

An important feature of magnetic scattering in underdoped $YBa_2Cu_3O_{6+x}$ (Dai *et al.*, 1996, 1998; Mook *et al.*, 1998; Fong *et al.*, 2000) is that the resonance precursors are detectable above T_c. Magnetic correlations, however, are strongly enhanced in the SC state, and there is a cusp in the temperature dependence of the resonant scattering intensity at T_c (Fong *et al.*, 2000). The doping dependence of the resonance energy and intensity indicates a strong enhancement of magnetic fluctuations as we approach half filling: for underdoped $YBa_2Cu_3O_{6+x}$ the resonance energy decreases with decreasing doping, and the intensity increases (Fong *et al.*, 2000). For overdoped $Bi_2Sr_2CaCu_2O_{8+\delta}$ it was found that the energy decreased (He *et al.*, 2001, 2002), which led to the suggestion that the resonance energy follows the SC transition temperature (He *et al.*, 2001).

The presence of a magnetic resonance in the SC states of many cuprates suggests that it is closely related to SC pairing. This idea was reenforced by the experiments of Dai *et al.* (2000), in which the SC coherence in $YBa_2Cu_3O_{6.6}$ was suppressed by applying a magnetic field. It was found that the resonance intensity decreased without any noticeable change in the resonance energy. Finally, Dai *et al.* (1996) demonstrated that the exchange energy associated with the resonance has the right magnitude, temperature, and doping dependences to describe the SC condensation energy of $YBa_2Cu_3O_{6+x}$ materials.

B. Contribution of π resonance to the spin-correlation function

Resonance that appears in the SC state suggests that what gets scattered is Cooper pairs, which are only

present below T_c. Based on this idea Demler and Zhang (1995) proposed that the resonance observed in inelastic neutron-scattering experiments is due to the presence of the π mode, a sharp collective mode in the particle-particle channel at momentum $\Pi=(\pi,\pi)$ with spin $S=1$. In the normal state such an excitation does not contribute to the magnetic spectrum, since the latter is determined by fluctuations in the particle-hole channel. Below T_c, on the other hand, condensed Cooper pairs couple the particle-hole and particle-particle channels (Demler and Zhang, 1995; Demler, Kohno, and Zhang, 1998) and cause the π excitation to appear as a sharp resonance in the magnetic spectrum with intensity set by the strength of mixing of the two channels, $|\Delta(T)|^2$, where $\Delta(T)$ is the amplitude of the SC order parameter. Such a scenario provides a natural explanation for the key properties of the observed resonance: its energy is essentially the energy of the π mode in the normal state and is temperature independent (Demler, Kohno, and Zhang, 1998), whereas the intensity of the resonance is set by $|\Delta(T)|^2$ and vanishes at T_c.

Coupling of the particle-particle π channel and the particle-hole AF channel may be understood using the commutation relations between the operators π_α and N_β given in Eq. (18). In the SC state, the d-wave SC order parameter that enters the right-hand side of Eq. (18) can be replaced by its expectation value in the ground state. Hence the commutator of π and N becomes a c number, and the two fields become conjugate variables, just as coordinate and momentum are conjugate to each other in elementary quantum mechanics. The result of such coupling is that the π mode appears as a sharp resonance in the spin-fluctuation spectrum. To demonstrate this we consider the spin-spin correlation function at wave vector Π,

$$\chi(\Pi,\omega) = -i\int e^{-i\omega t}\langle TN_\alpha(t)N_\alpha(0)\rangle dt = \sum_n |\langle n|N_\alpha|0\rangle|^2\left\{\frac{1}{\omega-E_n+i0}-\frac{1}{\omega+E_n-i0}\right\}. \tag{96}$$

Here $|0\rangle$ is the ground state and n summation goes over all excited states of the system. One of the excited states is created by the π operator defined in Eq. (28),

$$|\pi_\alpha\rangle = \frac{1}{\mathcal{N}}\pi_\alpha^\dagger|0\rangle, \tag{97}$$

where $\mathcal{N}$ is the normalization factor.

It is useful to realize that if $\pi^\dagger$ acting on the ground state creates an excited state, then π should annihilate it [otherwise it would create a state of lower energy than the ground state (Pines and Nozieres, 1966)]. Then we have

$$1=\langle\pi_\alpha|\ \pi_\alpha\rangle = \frac{1}{\mathcal{N}^2}\langle 0|\pi_\alpha\pi_\alpha^\dagger|0\rangle = \frac{1}{\mathcal{N}^2}\langle 0|[\pi_\alpha,\pi_\alpha^\dagger]|0\rangle \approx \frac{(1-n)}{\mathcal{N}^2}, \tag{98}$$

where n is the filling fraction ($n=1$ corresponds to half filling). In writing the last equality we assumed $\langle[g(p)]^2\rangle=1$ when averaged around the Fermi surface.

If we separate the contribution of the π state to $\chi(\Pi,\omega)$, we have

$$\chi(\Pi,\omega) = |\langle\pi_\alpha|N_\alpha|0\rangle|^2\frac{1}{(\omega-\omega_\pi+i0)} + \text{part regular at } \omega_\pi. \tag{99}$$

The resonant contribution to $\chi(\Pi,\omega)$ can be expressed as

$$\chi^{\text{res}}(\Pi,\omega) = \frac{1}{\mathcal{N}^2}|\langle 0|\pi_\alpha N_\alpha|0\rangle|^2\frac{1}{(\omega-\omega_\pi+i0)} = \frac{1}{\mathcal{N}^2}|\langle 0|[\pi_\alpha N_\alpha]|0\rangle|^2\frac{1}{(\omega-\omega_\pi+i0)} \approx \frac{|\langle 0|\Delta|0\rangle|^2}{(1-n)}\frac{1}{(\omega-\omega_\pi+i0)}. \tag{100}$$

The expectation value in the numerator of the last expression is simply the amplitude of the superonducting d-wave order parameter. We emphasize that Eq. (100) does not rely on the details of the microscopic model but only on the commutation relations between the π, N, and Δ given by Eq. (18) [this is somewhat analogous to the f-sum rule (Pines and Nozieres, 1966)]. To relate the order parameter to what one typically measures in experiments, we use BCS-type arguments to connect the order parameter to the quasiparticle gap (see, however, Uemura *et al.*, 1989; Emery and Kivelson, 1995) $\langle 0|\Delta|0\rangle = C\Delta_0/V_{\text{BCS}}$. Here Δ_0 is the maximal gap for Bogoliubov quasiparticles at the antinodal point, V_{BCS} is the interaction strength that we expect to be of the order of the nearest-neighbor exchange coupling J, and C is a dimensionless constant of the order of unity. Therefore we find

$$\chi^{\text{res}}(\Pi,\omega) = C^2\frac{|\Delta_0|^2}{J^2(1-n)}\frac{1}{\omega-\omega_\pi+i0}. \tag{101}$$

As we go to the underdone regime, Δ_0 remains constant or increases slightly, and the factor $1-n$ decreases. Equation (101) predicts that the intensity of the resonance should increase; this increase has been observed in the experiments of Fong *et al.* (2000).

It is useful to note that contributions from modes other than the π excitation do not spoil the result in Eq. (100). If most of the π spectrum is accommodated in an interval $(\omega_\pi-\nu,\omega_\pi+\nu')$, one can use the Cauchy-Schwarz inequality to prove a rigorous and model-independent result (Demler, Kohno, and Zhang, 1998) that

$$\frac{1}{\pi}\int_{\omega_\pi-\nu}^{\omega_\pi+\nu'} d\omega\, \mathrm{Im}\chi^{\mathrm{res}}(\Pi,\omega) \geq \frac{|\Delta|^2}{1-n}. \tag{102}$$

The left-hand side of this equation represents the contribution of the π mode to the spin-excitation spectrum, and the right-hand side gives its lower bound. Exact equality holds when the π operator is an exact eigenoperator and hence there is only one energy eigenstate, which satisfies $\langle 0|\pi_\alpha|n\rangle \neq 0$.

Thus a simple picture of the resonant neutron scattering is as follows: when an incoming neutron is scattered off one of the electrons in a Cooper pair, it transfers a momentum of (π,π) to this electron and flips its spin. At the end of the scattering process the Cooper pair has quantum numbers of the π mode, spin $S=1$, and momentum Π. If the energy transfer matches the energy of the π excitation, we have a resonance. In the next two sections we build upon this simple argument to establish a more detailed picture of the π resonance in two cases—the strong-coupling limit described by the $SO(5)$ nonlinear σ model, and the weak-coupling limit where Fermi-liquid-type analysis can be applied.

C. π resonance in the strong-coupling regime: the *SO*(5) nonlinear σ model and the projected *SO*(5) model

In this section we review how the resonant peak observed in inelastic neutron-scattering experiments appears in the $SO(5)$ nonlinear σ model, signalling competition between the AF and SC ground states. We use the Hamiltonian of this model [see Eq. (34)] to write the operator equations of motion ($\dot{O}=i[\mathcal{H},O]$) for the order parameters n_a and symmetry generators L_{ab}, with $a,b=\{1,\ldots,5\}$. For $\mu>\mu_c=\frac{1}{2}\sqrt{g/\chi}$ the system is in the SC ground state, which we can take to be along the n_1 direction. Linearizing the equations of motion around n_1 we obtain

$$\chi\partial_t^2 n_5 = \rho\nabla_k^2 n_5, \tag{103}$$

$$\chi\partial_t^2 n_\alpha = \rho\nabla_k^2 n_\alpha - [\chi(2\mu)^2 - g]n_\alpha. \tag{104}$$

The first equation describes the Goldstone mode of the spontaneously broken charge $U(1)$ symmetry (Bogoliubov-Anderson mode), and the second equation describes a triplet massive excitation of the superspin in the direction of the AF state (see Fig. 32).

In a model with exact $SO(5)$ symmetry, superspin ordering reduces the symmetry from $SO(5)$ to $SO(4)$ and should be accompanied by the appearance of four Goldstone modes [$SO(5)$ and $SO(4)$ have ten and six symmetry generators, respectively]. In the case of approximate $SO(5)$ symmetry that we discuss here, explicit symmetry breaking turns some of the Goldstone modes into pseudo-Goldstone excitations, i.e., they acquire a finite energy. This is similar to a chiral symmetry breaking in quantum chromodynamics, where the small mass of the quarks leads to a finite mass of pions, which are the Goldstone bosons of chiral symmetry breaking (Weinberg, 1995), but it does not change the fundamental nature of the latter.

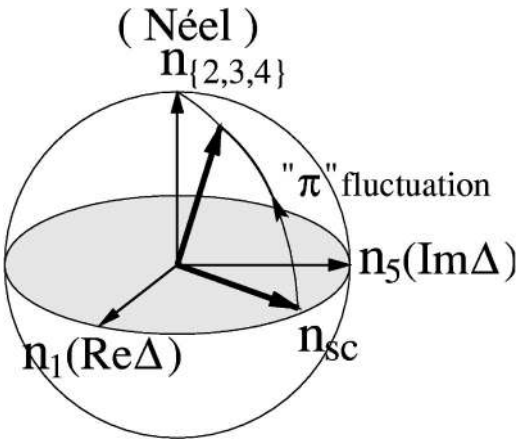

FIG. 32. The order-parameter space of the $SO(5)$ theory. π operator performs a rotation between the AF and the d-wave SC states. This small fluctuation is the new Goldstone mode of the $SO(5)$ theory.

The doping dependence of the resonance energy follows immediately from Eq. (104),

$$\omega_\pi = 2\sqrt{\mu^2-\mu_c^2} \propto \sqrt{x-x_c}. \tag{105}$$

The resonance energy is zero at the $SO(5)$-symmetric point $\mu=\mu_c$ and increases with doping x according to a square root law, where x_c is the critical doping. Vanishing of the resonance energy at μ_c is a special property of the $SO(5)$-symmetric point, and for a generic first-order transition between the AF and SC phases [see Fig. 10(a)] the resonance energy would remain finite at the transition point. When there is an intermediate uniform mixed AF/SC phase [the type-2 transition shown in Fig. 10(c)], the doping dependence of the resonance energy also obeys Eq. (105) with μ_c corresponding to the boundary between the SC and AF/SC phases (μ_{c2} in Fig. 10). Softening of the π mode in this case demonstrates a continuous transition into a state with magnetic order (Sachdev and Vojta, 2000; Demler *et al.*, 2001).

The dispersion of the π-resonance mode is model dependent. Hu and Zhang (2001) studied the dispersion of the π-resonance mode in the projected $SO(5)$ model using the strong-coupling expansion and concluded that the π mode can have a downward dispersion away from the Π point, reaching a minimum at some incommensurate wave vector. This model could possibly give a unified description of the neutron-resonance mode and the incommensurate magnetic fluctuations in the high-T_c cuprates.

In Sec. III.C we discussed the projected $SO(5)$ model that forbids double occupancy of the Cooper pairs by introducing chirality into the SC rotations. As was pointed out before, such a projection does not affect small fluctuations around the SC state (see Fig. 6) and does not change the relation (105).

D. π resonance in weak coupling: the Fermi-liquid analysis

In this section we consider a weakly interacting electron gas in a two-dimensional square lattice and show that the Fermi-liquid analysis of this system gives rise to a π mode that is very similar to the collective mode we discussed earlier in the strong-coupling limit. Using perturbative Fermi-liquid analysis to describe strongly interacting electron systems such as cuprates may cause reasonable objections from some readers. We remind the reader, however, that the goal of this exercise is to complement the strong-coupling discussion presented in the earlier sections. The benefit of the weak-coupling discussion is that it provides a simple picture of the π mode as an antibound state of two electrons in the spin-triplet state having a center-of-mass momentum Π and sitting on the neighboring lattice sites.

Our starting point is the *t*-*J*-type model on a two-dimensional lattice,

$$\mathcal{H} = -t\sum_{\langle ij\rangle\sigma} c_{i\sigma}^{\dagger}c_{j\sigma} + U\sum_{i} n_{i\uparrow}n_{i\downarrow} + J\sum_{\langle ij\rangle} \vec{S}_i\vec{S}_j. \tag{106}$$

Note that we do not impose a no-double-occupancy constraint but include the on-site Hubbard repulsion. Within the Hartree-Fock discussion presented here, the Hubbard U only renormalizes the band structure and does not affect collective excitations of the order of J. In the rest of the paper we shall therefore disregard the U term in the Hamiltonian (106) and assume that we work with the renormalized parameters.

To begin, we consider adding two noninteracting electrons to an empty two-dimensional lattice with the condition that the center of mass of the pair has momentum q. For a general q the energy of such a pair, given by $\epsilon_{q-k}+\epsilon_k$, depends on the relative momentum of the two electrons. Therefore we have a continuum of particle-particle excitations. When the center-of-mass momentum is $\Pi=(\pi,\pi)$, the whole particle-particle continuum collapses to a point. This can be verified by taking the tight-binding dispersion $\epsilon_k=-2t(\cos k_x+\cos k_y)$ and is shown schematically in Fig. 33. The collapse of the continuum makes it easier to create resonant states by adding interaction between the electrons. For example, the J term in the Hamiltonian (106) introduces an energy cost of $J/4$ for electrons sitting on the nearest-neighbor sites when their spins point in the same direction. Thus, if we make a two-electron pair in such a way that the two electrons form a triplet pair on the nearest-neighbor sites and have a center-of-mass momentum (π,π), we get an antibound state separated from the continuum by energy $J/4$. The argument above can be generalized to the case of adding two electrons on top of the filled Fermi sea. We recall that collective modes correspond to poles of the vertex functions (Abrikosov *et al.*, 1993). In the case of π resonance, we are interested in the particle-particle vertex, which we describe by Dyson's equation (Demler and Zhang, 1995) after separating the spin-triplet component of the interaction at the center-of-mass momentum Π from the *d*-wave symmetry of the electron pair,

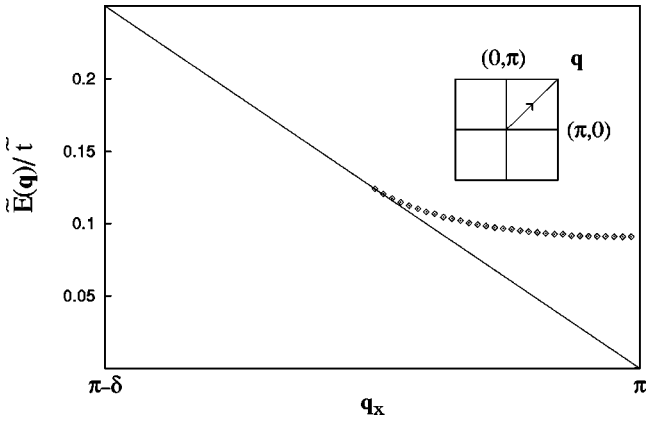

FIG. 33. The two-particle continuum and the π excitation for the tight-binding model. Note that the continuum of two-particle states collapses to a point when the center-of-mass momentum is $\Pi=(\pi,\pi)$. The π mode emerges as an anti bound state above the continuum.

$$\mathcal{H}_J = \frac{J}{4}\sum_{pp'} d_p d_k c_{p+\Pi\alpha}^{\dagger}(\sigma_2\vec{\sigma})_{\alpha\beta}c_{-p\beta}^{\dagger}c_{-k\gamma}(\vec{\sigma}\sigma_2)_{\gamma\delta}c_{k+\Pi\delta} + \cdots, \tag{107}$$

where d_p is defined in Eq. (26). From the equation presented in Fig. 34 we find the triplet particle-particle vertex

$$T(p,p',\Pi,\omega) = \frac{\frac{J}{4}d_p d_{p'}}{1-\frac{J}{4}\sum_k d_k^2\frac{1-n_k-n_{k+\Pi}}{\omega-\epsilon_k-\epsilon_{k+\Pi}}} \tag{108}$$

and observe that it has a pole at energy

$$\omega_\pi = -2\mu + \frac{J}{4}(1-n). \tag{109}$$

The first term in Eq. (109) originates from the kinetic energy of the tight-binding Hamiltonian $\epsilon_p+\epsilon_{p+\Pi}=-2\mu$, and the second part describes the nearest-neighbor exchange interaction of the triplet pair of electrons in the presence of a filled Fermi sea. The $(1-n)$ factor describes the blocking of the states below the Fermi energy from the phase space available for two-particle scattering. In the Hartree-Fock theory the chemical potential is proportional to doping; hence we find that the resonance energy in Eq. (109) scales with x. It is useful to point out that including the near-neighbor density interaction $V\Sigma_{\langle ij\rangle}n_i n_j$ in the Hamiltonian (106) will not change our discussion as long as the system remains in the *d*-wave SC state (Meixner *et al.*, 1997; Demler, Kohno, and Zhang, 1998). Such an interaction affects equally the π mode and Cooper pairs that constitute the ground state.

One can also ask how to use the perturbative approach to demonstrate the appearance of a π resonance in the spin-fluctuation spectrum below T_c. In Fig. 35 we

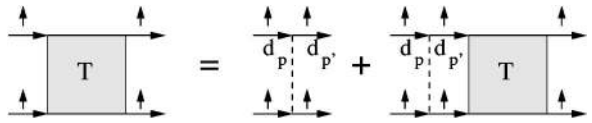

FIG. 34. Dyson's equation for the π resonance. The function $d(p)$ is defined in Eq. (26).

show that when we compute the spin-spin correlation function in the SC state, we need to include scattering of spin fluctuations at momentum (π,π) into the π pair, which corresponds to mixing the particle-particle ladder of diagrams into the particle-hole bubble. This contribution requires two anomalous Green's functions and is therefore proportional to $|\Delta|^2$. Detailed calculations based on the generalized random-phase approximation for the model (109) were presented by Demler, Kohno, and Zhang (1998); in Fig. 36, we show only a representative plot of a spin-spin correlation function $\chi(q,\omega)$ computed with an account of the π channel.

In summary, we have used a Fermi-liquid analysis to establish a simple picture of the π resonance; a triplet pair of electrons sitting on nearest-neighbor sites with the d-wave function of the pair and with the center-of-mass momentum Π.

E. Resonance precursors in the underdoped regime

In the underdoped cuprates the π resonance does not disappear above T_c but remains as a broad feature at higher temperatures (Dai *et al.*, 1996, 1998; Fong *et al.*, 1996; Mook *et al.*, 1998), with only a cusp in the temperature dependence of the intensity signalling the onset of the long-range d-wave SC order (Fong *et al.*, 2000). Demler and Zhang (1999b; Zhang, 1998) have pointed out that the most likely origin of these resonance precursors is the existence of strong d-wave SC fluctuations in the pseudogap regime of the underdoped cuprates. A precursor of π resonance in the spin-spin correlation function can be identified with a process in which a π pair and a preformed Cooper pair propagate in opposite directions, as shown in Fig. 37. Because uncondensed Cooper pairs have a finite energy, we expect precursors to appear at a slightly higher energy than the resonance itself and to have a width of the same order as the temperature (Demler and Zhang, 1999b).

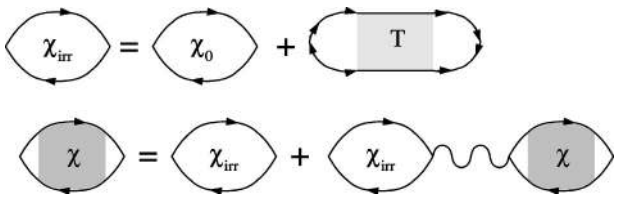

FIG. 35. π-resonance contribution to the spin susceptibility in the SC state.

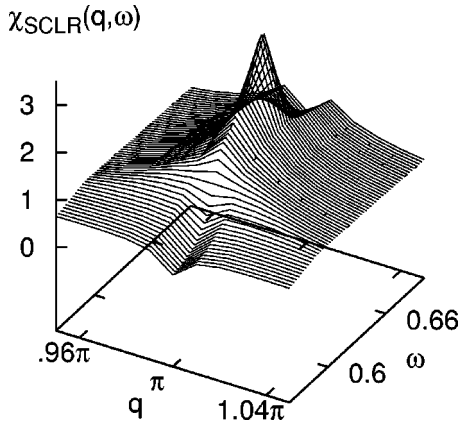

FIG. 36. Spin susceptibility in the SC state for the model (106). The wave vector is along the 0 to (π,π) direction. Susceptibility was computed using the self-consistent linear response formalism in Fig. 35. The peak at (π,π) comes from the π resonance. From Demler, Kohno, and Zhang, 1998.

F. Implications for experiments and comparison to other theories

In Sec. VI.C we discussed the π resonance as a pseudo-Goldstone mode of the $SO(5)$ nonlinear σ model, and in Sec. VI.D we gave a simple microscopic picture of the π mode as a sharp collective mode in the particle-particle channel with spin $S=1$ and momentum $\Pi=(\pi,\pi)$. From Eq. (100), we can see that the π-resonance intensity due to the contribution from the particle-particle channel scales with the square of the SC order parameter, namely,

$$I(\Pi)=\int d\omega\, \mathrm{Im}\chi^{\mathrm{res}}(\Pi,\omega)\propto|\langle\Delta(x,B,T)\rangle|^2. \tag{110}$$

Here we have explicitly shown the dependence of the SC order parameter $\Delta(x,B,T)$ on doping x, magnetic field B, and temperature T. This simple scaling relation therefore makes powerful predictions about the resonance intensity. It has been tested in a number of experiments. Our analysis explains several puzzling features of the resonance observed in experiments. The first is the striking contrast between its temperature-dependent intensity and the temperature-independent energy. In the case of the Bardasis-Schrieffer exciton (Bardasis and Schrieffer, 1961) that appears as a bound state below the quasiparticle gap for s-wave superconductors, both the energy and the intensity of the exciton are determined by the SC gap; hence, as the temperature is increased in the SC state, both the resonance energy and its intensity decrease. In the case of the π mode, on the other hand, a different behavior of the resonance intensity and energy are expected. The energy is essentially given by the energy of the π mode in the normal state and does not change with temperature. The resonance intensity is set by the d-wave SC order parameter, as given in Eq. (110); it decreases with increasing temperature and vanishes at T_c. Equation (110) also predicts that the suppression of the SC coherence by a magnetic field should lead to a

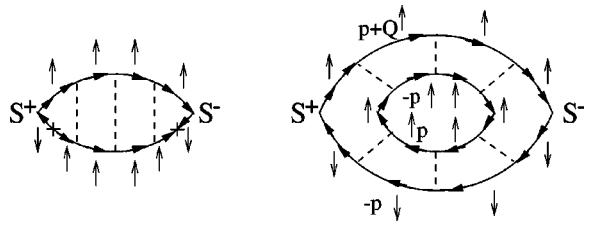

FIG. 37. Feynman diagram for the π resonance below T_c contrasted with the diagram above T_c. The + denotes the anomalous scattering in the SC state which converts a particle into a hole and vice versa.

rapid decrease in the resonance intensity without changing the resonance energy. This prediction was confirmed experimentally in a striking experiment by Dai *et al.* (2000), whose results are reproduced in Fig. 38. The *SO*(5) theory predicts (Demler and Zhang, 1995; Zhang, 1997) that with decreasing doping the resonance intensity should increase [see Eq. (101)] and its energy should decrease [see Eqs. (105) and (109)], both of which were observed by Fong *et al.* (2000), as we show in Fig. 39. Note that for small values of the chemical potential there is a small difference in the precise ω_π vs μ relation obtained from the nonlinear σ model and from Fermi-liquid analysis. We expect the strong-coupling expression (105) to be more reliable close to the AF/SC transition, where $\mu \sim \mu_c$, and suggest that comparison of the doping dependence of the resonance energy (Fong *et al.*, 2000) and the chemical potential (Ino *et al.*, 1997; Fujimori *et al.*, 1998) should be an important test of the *SO*(5) theory.

After this π-resonance theory was developed by Demler and Zhang (1995), alternative descriptions of the resonance were proposed.[4] These typically discuss the resonance as a magnetic exciton that is overdamped in the normal state but becomes sharp in the *d*-wave SC state when a gap opens up for single-particle excitations. In the *d*-wave SC state, the particle-particle channel and the particle-hole channels are mixed into each other and there are, strictly speaking, no rigorous distinctions among these different theories. However, the quantitative predictions differ in important details. Near the T_c transition, the π-resonance theory predicts the sharp onset of magnetic resonance due to coupling to the particle-particle channel, whose contribution to the magnetic scattering can be rigorously established via the Cauchy-Schwarz inequality, as shown in Eq. (102). Some of these alternative theories expect a gradual broadening of the resonance rather than a sharp reduction of the intensity as T_c is approached from below. The

[4]Such descriptions include Barzykin and Pines, 1995; Blumberg *et al.*, 1995; Liu *et al.*, 1995; Mazin and Yakovenko, 1995; Onufrieva and Rossat-Mignod, 1995; Bulut and Scalapino, 1996; Millis and Monien, 1996; Yin *et al.*, 1997; Assaad and Imada, 1998; Morr and Pines, 1998; Weng *et al.*, 1998; Brinckmann and Lee, 1999; Yoshikawa and Moriya, 1999; Sachdev and Vojta, 2000; Manske *et al.*, 2001; Norman and Pepin, 2003.

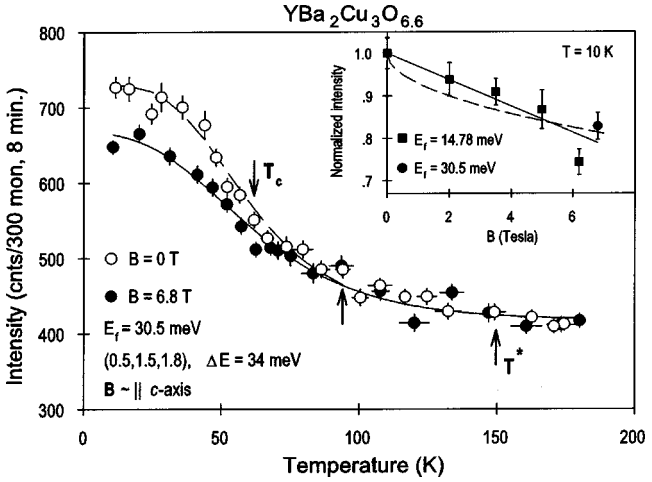

FIG. 38. Suppression of the resonance intensity by the magnetic field. From Dai *et al.*, 2000.

π-resonance theory predicts that the energy of the magnetic resonance mode will be independent of the temperature near T_c, while some of the alternative theories predict that the mode energy should vanish as the SC gap. In Sec. VII.E, we shall discuss a rigorous distinction between the π mode in the particle-particle channel and the magnetic exciton in the particle-hole channel in the

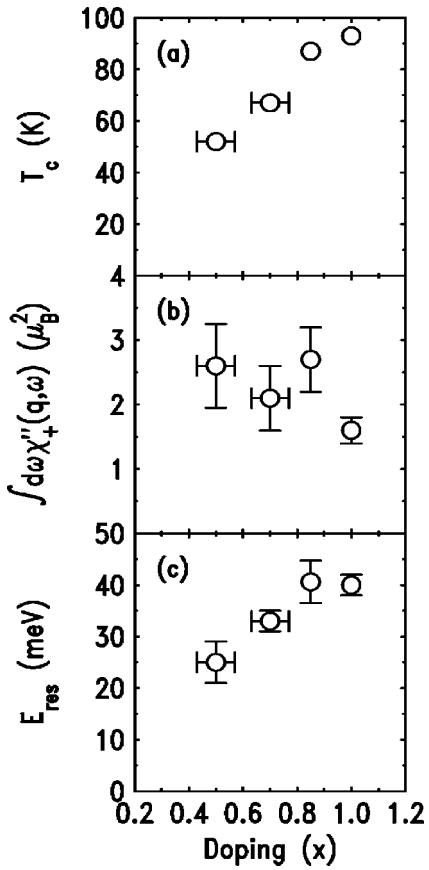

FIG. 39. Doping dependence of the resonance energy and intensity measured in neutron-scattering experiments. From Fong *et al.*, 2000.

normal state, and we shall discuss an experimental proposal by which this distinction can be tested.

Several proposals have been made regarding the implications of the resonance peak for various properties of the cuprates (see Kee *et al.*, 2002, for a critical review). Scattering of quasiparticles on the π mode was argued to be responsible for the "kink" in the quasiparticle dispersion (Johnson *et al.*, 2001), the "peak-dip-hump" structure measured in ARPES (Eschrig and Norman, 2000; Abanov *et al.*, 2001), and the pseudogap seen in optical conductivity (Schachinger *et al.*, 2001). Superconducting pairing mediated by the π resonance was suggested by Carbotte *et al.* (1999), Orenstein (1999), Abanov *et al.* (2001), and Zasadzinski *et al.* (2003), and the relation between the resonance intensity and the condensate fraction was pointed out by Chakravarty and Kee (2000). We do not discuss these proposals here, but in the next section we shall review the important role that the resonance plays in the thermodynamics of the SC state. We shall argue that the SC condensation energy may be accounted for by the lowering of spin-exchange energy due to the appearance of the resonance below T_c (Demler and Zhang, 1998).

G. The microscopic mechanism and the condensation energy

The central question in the field of high-T_c superconductivity concerns the microscopic mechanism of superconductivity. In conventional superconductors, the pairing interaction is mediated by the phonon interactions (see Maksimov *et al.*, 1997, for a review). Within the weak-coupling BCS theory, the vertex corrections are suppressed by a small parameter, namely, the ratio of the electron mass to the mass of the nuclei. Thus the interaction which mediates the pairing of electrons can be unambiguously determined. In the case of high-temperature superconductivity, the dominant interactions are the Coulomb interaction and the AF exchange interaction. In such a strongly coupled system, the traditional approach based on the Feymann diagram expansion does not work, and the nature of the pairing interaction is not easily revealed by studying low-order diagrams. However, the mechanism of superconductivity can still be addressed by identifying which of the interaction terms in the Hamiltonian lead to a lowering of the energy of the SC state. By comparing the magnitude of the energy saving associated with a particular interaction term with the actual experimental measurement of the condensation energy, the mechanism of superconductivity can be unambiguously identified. In our discussion in the previous section we showed that the π mode contributes to the spin fluctuation spectrum below T_c and therefore enhances AF correlations in the SC state. Demler and Zhang (1998) showed that π resonance can be promoted from being a consequence of superconductivity to being the real driving force behind electron pairing. By analyzing the neutron-scattering data, Demler and Zhang demonstrated that a reduction of the AF exchange energy in the superconducting state due to the appearance of the π resonance can be sufficient to stabilize superconductivity. In this section we provide the details of this argument focusing on the microscopic *t-J* model, and we discuss its relevance to the condensation energy of $YBa_2Cu_3O_{6+x}$ materials. We also demonstrate that this scenario can be formulated as an additional contribution to the BCS coupling constant in the weak-coupling regime.

1. The π-resonance contribution to the condensation energy

The SC condensation energy is defined as the energy difference between the SC and the normal states at $T=0$ (Schreiffer, 1964; Tinkham, 1995). In type-I superconductors it can be obtained directly by measuring the critical value of the magnetic field H_c at the first-order transition between the normal and SC states. At the transition point, the energies of the two phases are equal (note that at $T=0$ the free energy is equal to the energy) and, assuming that the normal state is not affected by the magnetic field, we obtain the condensation energy per unit cell

$$E_C = E_N - E_S = \frac{V_0 H_c^2}{8\pi}, \tag{111}$$

where $V_0 = a \times b \times c$ is the volume of the unit cell. For type-II superconductors including the high-T_c materials, such a simple argument is not available. However, one can use Landau-Ginzburg theory to relate the condensation energy to H_{c1} and H_{c2}, or alternatively to the SC coherence length ξ_0 and London penetration depth λ (Tinkham, 1995):

$$H_c^2 = \frac{\Phi_0}{8\pi\xi_0\lambda}, \tag{112}$$

where $\Phi_0 = hc/2e$ is the SC flux quantum. An alternative approach to measuring the condensation energy is to integrate the difference between the SC and the normal-state specific heat from $T=0$ to T_c, where the normal-state specific heat below T_c is defined as extrapolation from temperatures above the transition point (Loram *et al.*, 1990, 1994). To be more precise, let us consider the condensation energy of the optimally doped $YBa_2Cu_3O_7$. Taking the characteristic values $\xi_0 = 12-20$ Å and $\lambda = 1300-1500$ Å, with $a=b=3.85$ Å and $c=11.63$ Å, we find a condensation energy of $E_C = 3.5-12$ K per unit cell. The determination of the E_C of this material using specific-heat measurements by (Loram *et al.*, 1990, 1994) gives $E_C = 6$ K per unit cell.

Ideally, one would like to start with a microscopic model that has the kinetic energy of electrons and ions and the Coulomb energies of all particles, and to calculate the condensation energy from first principles. Although this is possible in principle, in practice this approach is very hard to accomplish because of the large scales involved in both the kinetic and the Coulomb energies. A method that is easier to pursue in practice is to start with an effective model defined on a much smaller

energy scale and try to calculate the condensation energy within this effective model. This approach has been undertaken by Scalapino and White (1998) within the *t-J* model. In the *t-J* Hamiltonian in Eq. (2), we have two terms: the kinetic energy of electrons (with the Gutzwiller projection operator) and the exchange energy of electrons. In analogy to conventional superconductors, we expect that the transition into the SC state is driven primarily by a lowering of the interaction part of the Hamiltonian, i.e., the exchange term (in conventional superconductors the relevant interaction is the electron-ion Coulomb interaction). Is it possible then to find the change in the exchange energy between the normal and SC states? Scalapino and White made the insightful observation that the value of the J term in Eq. (2) is directly related to the dynamic spin structure factor $\chi''(q,\omega)$, the quantity that is being measured directly in neutron-scattering experiments. And the change in the exchange energy, $\Delta E_J = E_J^N - E_J^S$, can be directly expressed as a frequency and momentum integral of the difference in dynamic spin structure factors $\chi_N''(q,\omega) - \chi_S''(q,\omega)$ as follows:

$$\Delta E_J = 3J\left(\frac{a}{2\pi}\right)^2 \int_{-\pi/a}^{\pi/a} d^2q \int_0^\infty \frac{d(\hbar\omega)}{\pi} \times [\chi_N''(q,\omega) - \chi_S''(q,\omega)][\cos(q_x a) + \cos(q_y a)]. \tag{113}$$

In Eq. (113) the form factor arises from the nearest-neighbor interaction. This equation applies to quasi-two-dimensional systems, and $q=(q_x,q_y)$ is a two-dimensional in-plane momentum. A generalization of Eq. (113) to bilayer systems, the case relevant for $YBa_2Cu_3O_{6.35}$, is given by Demler and Zhang (1998).

The quantity $\chi_N''(q,\omega)$ in Eq. (113) is not the normal-state spin structure above T_c but rather an extrapolated normal-state quantity at $T=0$. Experimentally, one has to carefully identify features in $\chi''(q,\omega)$ which change abruptly at T_c. From inelastic neutron-scattering experiments we know that the most drastic change between the SC and normal-state spin structure factors is the appearance of the 41-meV scattering peak. Even for underdoped materials, which have many more AF fluctuations in the normal state, the main change between the normal and SC states is the appearance of the resonance (Fong *et al.*, 2000). It is reasonable, then, to take Eq. (113) for ΔE_J, calculate the contribution of the π resonance, and argue that this will be the dominant contribution. For optimally doped $YBa_2Cu_3O_{6.35}$, Fong *et al.* (1996) measured the absolute intensity of the resonance $\int_0^\infty d(\hbar\omega)\chi_S''(\Pi,\omega)$ to be 0.52 at $T=10$ K. This resonance has a Gaussian profile centered at Π with a width $\kappa_{2D}=0.23$ Å^{-1}, so the two-dimensional integral can be easily estimated, and

$$\Delta E_J = \frac{3}{2}\pi\left(\frac{a}{2}\kappa_{2D}\right)^2 \frac{1}{2}\frac{0.52}{\pi} = 0.016J. \tag{114}$$

Taking $J=100$ meV we find that the change in the exchange energy between the normal and SC states is approximately 18 K per unit cell. This remarkable number tells us that the resonance alone can account for the SC condensation energy.

Regarding our estimate of ΔE_J in Eq. (114), a comment must be made. The dynamic spin-structure factor $S(q,\omega)$ satisfies the sum rule (Scalapino *et al.*, 1998)

$$3\left(\frac{a}{2\pi}\right)^2 \int_{-\pi/a}^{\pi/a} d^2q \int_0^\infty \frac{d(\hbar\omega)}{\pi}\chi''(q,\omega) = (1-x)S(S+1). \tag{115}$$

Therefore the spectral weight for the resonance needs to come from other regions in q-ω space. In obtaining Eq. (114) we made an additional assumption that in the normal state this weight was spread uniformly in q in $\chi''(q,\omega)$ and did not contribute to Eq. (113), since any uniform component in $\chi''(q,\omega)$ is canceled by the $[\cos(q_x a)+\cos(q_y a)]$ factor in Eq. (113). It is also useful to point out that the weight of the resonance is less than 1% of the total sum rule (Demler and Zhang, 1998; Kee *et al.*, 2002), which, when multiplied by the AF exchange energy J, gives the correct order of magnitude for the condensation energy.

The condensation energy argument can be generalized to finite temperatures. In this case the resonant peak intensity at temperature T should be related to the free-energy difference between the SC and normal states, which in turn is given by the integral of the specific-heat difference above T. This hypothesis has been analyzed by Dai *et al.* (1999), who showed that the temperature derivative of the resonant peak intensity follows very closely the specific-heat anomaly for different dopings of $YBa_2Cu_3O_{6+x}$. We show this comparison in Fig. 40. For optimal doping there is a BCS-type anomaly in the specific heat at T_c, which corresponds to the resonance appearing abruptly in the SC state. For underdoped samples the specific-heat anomaly is broadened, which agrees with the resonance precursors appearing above T_c. This highly nontrivial experimental test establishes the contribution of the π resonance to the condensation energy.

We therefore see that the π-resonance mode naturally accounts for the condensation energy in the high-T_c superconductors. The AF exchange interaction is lowered in the SC state, and this energy saving can drive the transition from the normal state to the superconducting state. Within this scenario, the AF exchange energy is decreased, while the kinetic energy is increased below the SC transition. On the other hand, a number of theories argue that the dominant driving mechanism of high-temperature superconductivity is the saving of the kinetic energy, either along the c axis, or in the CuO_2 plane (Anderson, 1997; Chakravarty *et al.*, 1999; Hirsch and Marsiglio, 2000). The c-axis kinetic-energy-saving

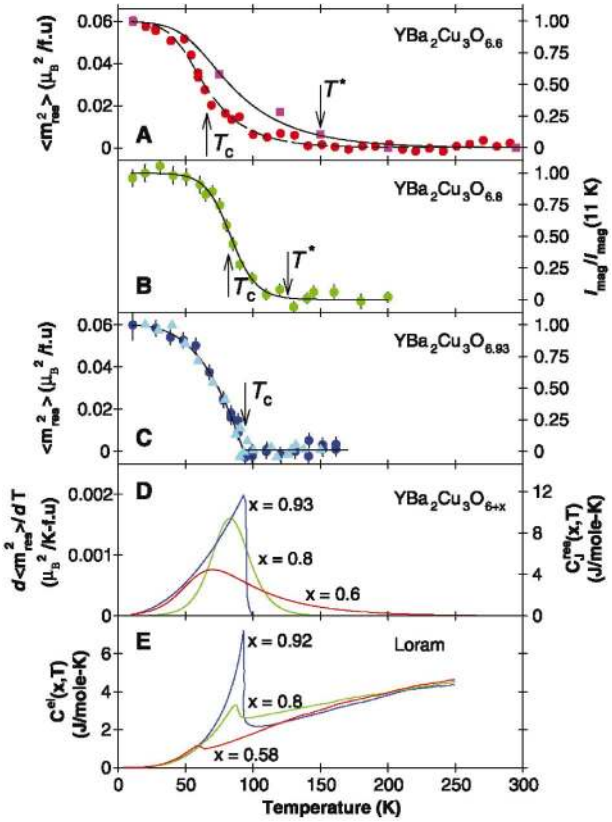

FIG. 40. (Color) Temperature dependence of the resonance intensity compared to the specific heat. From Dai *et al.*, 1999.

mechanism has been definitively ruled out experimentally (Moler *et al.*, 1998). Measurement of the *ab*-plane kinetic energy has not yielded conclusive results (Molegraaf *et al.*, 2002; Keimer, 2004). The π-resonance-based AF exchange energy saving is an experimentally established mechanism, which can account for the condensation energy in the high-T_c cuprates. Recent experiments indicate that phonon-mediated attraction also plays a role in the mechanism of high-temperature superconductivity (Lanzara *et al.*, 2001). It is possible that various mechanisms contribute constructively to the condensation energy in the high-T_c superconductors. In this case, it is important to measure the relative magnitudes of various contributions and identify the leading contribution to the condensation energy.

2. Microscopic discussions and relation to BCS pairing

In the theory of Demler and Zhang (1998), the saving of the AF exchange energy arises from the coupling of the AF order parameter $\vec{N}$ to the $\vec{\pi}$ operator in the SC state. This coupling leads to additional spectral weight, proportional to $|\Delta|^2$, in the AF spin-correlation function, thus lowering the AF exchange energy. This argument is generally valid, in both strong- and weak-coupling limits. However, it is also useful to connect this theory to the conventional BCS pairing theory in the weak-coupling limit. In the limit of weakly interacting electron gas, we

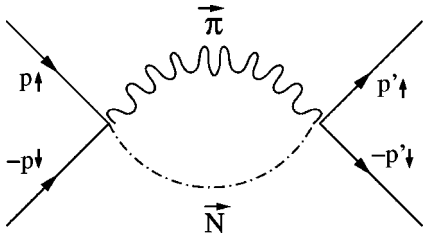

FIG. 41. SC pairing between electrons mediated by exciting a virtual magnon-π-mode pair.

can formulate this scenario as a contribution to the BCS coupling in the *d*-wave channel. In Fig. 41, we show a schematic representation of such a contribution: a Cooper pair splits into two virtual excitations—a magnon ($\vec{N}$) and a π particle ($\vec{\pi}$)—which then recombine into a Cooper pair. One can easily verify that the quantum numbers are matched in this process: quantum numbers of the combination of the π mode (charge 2, momentum Π, spin $S=1$) and the magnon (charge 0, momentum Π, spin $S=1$) sum to exactly the quantum numbers of the Cooper pair (charge 0, momentum $q=0$, spin $S=0$). This may also be formulated using electron Green's functions, as shown in Fig. 42. We start with a Cooper pair formed by the electrons $(p\uparrow)$ and $(-p\downarrow)$. After the latter electron emits a magnon, shown as an upper particle-hole ladder with total momentum Π and spin $S_z=-1$, we have two electrons with momentum Π and spin $S_z=1$. These are exactly the quantum numbers of the π mode that we describe by the lower particle-particle ladder in Fig. 42.

VII. KEY EXPERIMENTAL PREDICTIONS

A. The antiferromagnetic vortex state

A fundamental prediction of the *SO*(5) theory is the smooth rotation from the AF state to the SC state as the doping density is varied. As shown in Sec. V.B and V.C, this prediction has been tested numerically within the *t-J* model, with good agreement. However, testing this prediction directly in experiments would be much harder, since the doping level of most cuprates cannot be controlled well in the regime where the transition from the AF to SC state is expected to occur. Therefore, Zhang (1997) and Arovas *et al.* (1997) proposed testing this prediction in the vortex state of underdoped cuprates. Around the center of the vortex core, the phase of the SC order parameter winds by $\pm 2\pi$, and its amplitude is constrained to vanish at the center for topological reasons. In conventional BCS superconductors, the metallic Fermi-liquid ground state is realized inside the vortex core. In the *SO*(5) theory, the SC order parameter is embedded as a component of a higher-dimensional order parameter, namely, the superspin. When the amplitude of the SC order parameter vanishes in the vortex core, the amplitude of the superspin order parameter can still remain constant, provided that the

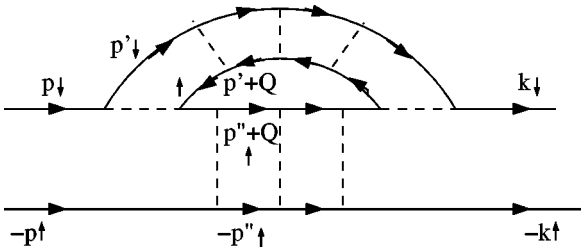

FIG. 42. Diagrammatic representation of SC pairing mediated by exciting a virtual-magnon π-mode pair: solid lines, electron propagators; dashed lines, interactions. The upper particle-hole ladder corresponds to the magnon and the lower particle-particle ladder corresponds to the π mode.

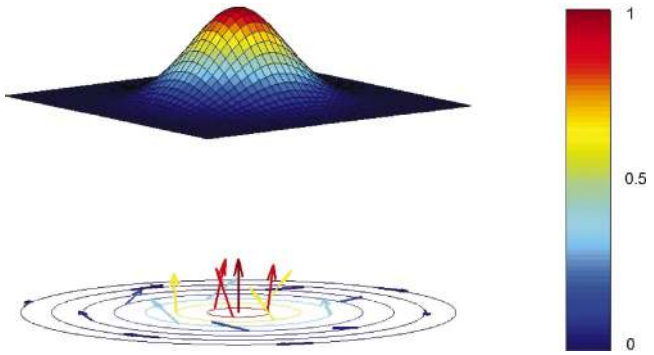

FIG. 43. (Color) SC vortex with AF core. Far from the center of the vortex core, the superspin vector lies in the SC plane and winds around the vortex core by 2π. The superspin vector lifts up to the AF direction as it approaches the center of the vortex core. The arrows represent the direction of the superspin and the color scale represents the magnitude of the AF order parameter.

superspin vector slowly rotates from the SC direction into the AF direction as the vortex core is approached. The superspin configuration near the vortex core is shown in Fig. 43. This type of topological field configuration is known as the *meron solution*, meaning half of a Skyrmion (Rajaraman, 1982). Figure 43 shows the rotation of the superspin in the vicinity of a vortex core. The AF order, which develops around the center of the vortex core, can be measured directly in experiments and can provide a quantitative test of the *SO*(5) symmetry.

When the SC order is destroyed in the vortex core, the closest competing order develops in the vortex state. Aside from commensurate or incommensurate magnetic order and charge order, a number of novel correlation states have been proposed, including, for example, circulating orbital currents (Chakravarty *et al.*, 2001; Lee, 2002) and fractionalized excitations (Sachdev, 1992; Senthil and Fisher, 2001). The vortex core state can provide a key test for various forms of the competing orders that have been proposed (Sachdev and Zhang, 2002).

Magnetic field provides a clean tuning parameter that can be used to investigate quantum transitions between the SC and AF phases. By solving both the *SO*(5) nonlinear sigma model and the Landan-Ginzburg model of competing AF and SC order parameters, Arovas *et al.* (1997) predicted the existence of the AF vortex state in the underdoped cuprates and further suggested a systematic experimental search for the AF vortex state in neutron scattering and muon spin-rotation experiments. These authors also predicted that the magnetic-field-induced AF moment should increase linearly with the applied magnetic field, or the number of vortices in the system, when the applied magnetic field is small compared to the upper critical field B_{c2}. While the original analysis of Arovas *et al.* focused on the regime where the transition between AF and SC is a direct first-order transition [corresponding to Fig. 10(a) of the phase diagram], Demler *et al.* (2001) and Zhang *et al.* (2002) analyzed the case in which there are two second-order phase transitions with an intervening uniform AF/SC mixed phase, corresponding to Fig. 10(c) of the phase diagram. In this case the AF order extends far beyond the vortex core region. The analysis of Demler *et al.* (2001) and Zhang *et al.* (2002) demonstrates that the suppression of the SC order in this regime is dominated by circulating supercurrents and leads to a logarithmic correction to the linear dependence of the field-induced moment. Recently, a number of experiments have been performed to test the prediction of the AF order in the vortex state. Neutron scattering under a magnetic field can directly measure the field-induced AF moment. Katano *et al.* (2000) measured enhanced magnetic scattering in the $La_{2-x}Sr_xCuO_4$ crystal at $x=12\%$ doping. The intensity of elastic magnetic peaks around the (π,π) point increases at $B=10$ T by as much as 50%. Lake *et al.* (2001) observed enhanced dynamic AF spin fluctuations in an optimally doped $La_{2-x}Sr_xCuO_4$ crystal at $x=16\%$ doping in an applied magnetic field. Without an applied field, the SC state has a spin gap of about 6 meV. An applied field of $B=7$ T introduces a spectral weight in the energy range of 3–4 meV. The mixed AF/SC phase has been also investigated in crystals of both underdoped $La_{2-x}Sr_xCuO_4$ at $x=10\%$ doping and La_2CuO_{4+y}. In both materials the applied magnetic field strongly enhances the quasistatic AF ordering (Khaykovich *et al.*, 2002; Lake *et al.*, 2002). The field dependence of the induced AF scattering is approximately linear, as predicted by Arovas *et al.* (1997), and it agrees quantitatively with the $B\ln(B/B_{c2})$ form proposed by Demler *et al.* (2001), with the correct value of B_{c2}. Another method of measuring the AF order is nuclear magnetic resonance (NMR). In the vortex state, the magnetic field is distributed inhomogeneously over the sample, with the maxima centered at the vortex cores. The NMR frequency thus correlates directly with the location of the nucleus in the vortex lattice. Using NMR on the ^{17}O nucleus of $YBa_2Cu_3O_7$ under a magnetic field as high as 40 T, Mitrovic *et al.* (2001, 2003) detected a sharp increase of the $1/T_1T$ rate near the vortex core as the temperature was lowered, indicating enhanced AF ordering (see also Curro *et al.*, 2000). Kakuyanagi *et al.* (2002) performed Tl NMR in a $Tl_2Ba_2CuO_{6+\delta}$ sample. Tl NMR provides a more direct test of AF ordering, since the ^{205}Tl nucleus is located directly above the Cu spins.

The temperature dependence of the $1/T_1T$ rate shows that the AF spin correlation is significantly enhanced inside the vortex core, compared with regions outside. The last class of magnetic experiments we discuss are the muon spin rotation (μSR) experiments. When muons are stopped inside a solid, their spin precesses around the local magnetic field. Since muons decay predominantly along the direction of their spin, the spatial decay pattern yields direct information about the local magnetic-field distribution in a solid. Miller *et al.* (2002) performed a μSR experiment in an underdoped $YBa_2Cu_3O_{6.5}$ system under a magnetic field of $B=4$ T. They found that the local magnetic-field distribution had a staggered pattern, superimposed on a uniform decay away from the vortex core. The staggered magnetic field detected at the muon site was about 18 G. All the experiments discussed above were carried out at fields far below the upper critical field B_{c2}, which in hole-doped materials typically exceeds 60 T. In order to establish the nature of the competing state, one has to perform experiments close to B_{c2}. This was achieved in recent neutron-scattering experiments on an electron-doped $Nd_{1.85}Ce_{0.15}CuO_4$ crystal in magnetic fields up to 14 T, far above the upper critical field B_{c2} (Kang *et al.*, 2003). Kang *et al.* found field-induced AF scattering at $(\pi,\pi,0)$ and observed that the AF moment scales approximately linearly with the applied field up to B_{c2}. The AF moment decreases with the magnetic field in the range between B_{c2} and 14 T. Their experimental data and the theoretical fit are shown in Fig. 44. The experimental findings of Kang *et al.* (2003) have been confirmed by Fujita *et al.* (2003) in a related, electron-doped material, $Pr_{1-x}LaCe_xCuO_4$. While $Nd_{1.85}Ce_{0.15}CuO_4$ material contains the magnetic Nd moment, the $Pr_{1-x}LaCe_xCuO_4$ material studied by Fujita *et al.* does not contain such magnetic ions, thus confirming that the field-induced AF moment cannot be due to any spurious effects associated with the Nd moments (Mang *et al.*, 2003). As we shall see below, the wide field range of the neutron data enables quantitative comparisons with theoretical models.

Since the original theoretical prediction of the AF vortex state, tremendous theoretical progress has been made on the subject of AF vortex lattices.[5] Based on the variational solution of the *t-J* model, Ogata (1999) concluded that the vortex core has an AF phase with an ordered moment about 10% of the full moment. This calculation established the microscopic basis of the AF vortex core. The initial AF vortex solutions were based on the static mean-field theory. In the weak-field regime where the vortex cores are separated far from each other, enhanced AF order can be viewed either as dynamic fluctuations of the AF order parameter due to the finite size of the vortex core or as the bulk AF fluctuation pulled below the spin gap and spatially bound near the vortex cores. This dynamic picture was developed by Bruus *et al.* (1999), Demler *et al.* (2001), and Hu and Zhang (2002) and could apply to experiments by Lake *et al.* in optimally doped LSCO. Classical Monte Carlo calculations of the *SO*(5) model also show the existence of the AF vortex lattice (Hu, 1999a). While the original theory of the AF vortex state was developed for the commensurate AF order, it can also be generalized to the case in which the AF ordering wave vector deviates from the (π,π) point, as in the LSCO system (Hu and

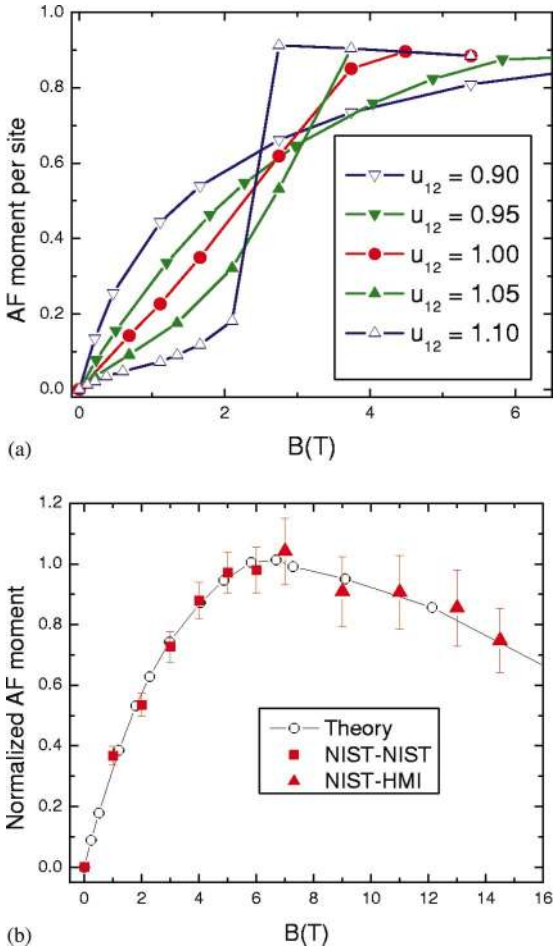

FIG. 44. (Color) Field dependence of the AF moment for different parameters of the Landau-Ginzburg theory (as defined by Chen, Wu, and Zhang, 2003). The parameters are $\rho_1=\rho_2=a^2$, $r_1=-1$, $r_2=-0.85$, $u_1=u_2=1$, and $\chi=42.4$. Here the parameters are chosen such that the maximum SC order is 1 and the SC coherence length at zero field equals the lattice constant a of the lattice model. (a) Field dependence for different values of u_{12}. The curvature strongly depends on u_{12}. (b) Fit to the neutron-scattering results of Kang *et al.* (2003) of the $Nd_{1.85}Ce_{0.15}CuO_4$ crystal with $u_{12}=0.95$. B_{c2} is about 6.2 T in this sample. The experimental data are obtained by subtracting the magnetic-field response along the *c* axis from the magnetic-field response in the *ab* plane, so that the response from the Nd moment can be removed.

[5]See, for example, Alama *et al.*, 1999; Bruus *et al.*, 1999; Hu, 1999a; Ogata, 1999; Andersen *et al.*, 2000; Han and Lee, 2000; Mortensen *et al.*, 2000; Demler *et al.*, 2001; Franz and Tesanovic, 2001; Chen *et al.*, 2002; Chen and Ting, 2002; Franz, Sheehy, and Tesanovic, 2002; Ghosal *et al.*, 2002; Hu and Zhang, 2002; Juneau *et al.*, 2002; Kivelson *et al.*, 2002; Zhang *et al.*, 2002.

Zhang, 2002; Zhang *et al.*, 2002). Antiferromagnetic ordering inside the vortex core has a profound effect on the electronic structure of the vortex, since it opens up an insulatorlike energy gap inside the vortex core where the conventional SC gap vanishes. The conventional theory of d-wave vortices based on Bogoliubov–de Gennes mean-field theory predicts a large and broad peak at the Fermi energy in the local density of states, the so-called zero-energy peak, and at the vortex core (Wang and Macdonald, 1995). However, scanning tunneling spectroscopy in BSCCO, giving the local density of states around the vortex core directly, shows only a small double-peak structure at energies of 7 meV (Pan *et al.*, 2000). A similar situation was observed in YBCO compounds (Maggioaprile *et al.*, 1995). The suppression of the local density of states due to AF ordering inside the vortex core could naturally explain this phenomenon (Ogata, 1999; Andersen *et al.*, 2000; Chen and Ting, 2002). However, other forms of order or the smallness of the core size could also offer alternative explanations (Tsuchiura *et al.*, 2003).

While experimental observation of an AF vortex state confirms a major prediction of the $SO(5)$ theory, most of these experiments have not directly tested the symmetry between AF and SC in the strictest sense. In the following, we shall discuss two aspects of the AF vortex state which directly pertain to $SO(5)$ symmetry. The spatial variation of the AF and SC order parameters around the vortex core leads to a region of space where both order parameters coexist. In this region, the π order parameter, whose magnitude can be quantitatively predicted by the $SO(5)$ orthogonality relation in Eq. (41), also develops. Ghosal, Kallin, and Berlinsky (2002) have quantitatively verified this relationship from their numerical solution of the t-J model around the vortex core. It would be desirable to find a way to measure the π order parameter and test this relation experimentally.

The detailed experimental data now available up to B_{c2} in electron-doped cuprates allow for a quantitative test of $SO(5)$ symmetry. As discussed in Sec. IV.A, within models of competing AF and SC order, a crucial test for $SO(5)$ symmetry is the relation $u_{12}^2=u_1u_2$ for the quartic term in Eq. (59). Deviation from the $SO(5)$ relation determines the curvature of the ground-state energy-versus-doping plot, which can be used to determine the nature of the transition between the AF and SC states. Recently, Chen, Wu, and Zhang (2003) numerically solved the Landau-Ginzburg model with competing AF and SC order in the vortex state and found that the deviation from the $SO(5)$ relation $u_{12}^2=u_1u_2$ also determines the curvature of the field-induced AF moment versus the magnetic-field plot for magnetic fields up to B_{c2}. The neutron-scattering data obtained in NCCO superconductors (Kang *et al.*, 2003) can be fitted by $u_{12}^2/u_1u_2=0.95$, showing that this system has only a 5% deviation from $SO(5)$ symmetry. When the magnetic field exceeds B_{c2}, it causes canting of the spin moments, thereby reducing the AF moment while increasing the ferromagnetic moment. Thus the $SO(5)$ theory quantitatively explains the experimental data over the entire magnetic-field range below 14 T. The experimental results of Fujita *et al.* (2003) in $Pr_{1-x}LaCe_xCuO_4$ are quantitatively similar. We note that the mean-field analysis of the Ginzburg-Landau free energy does not include quantum fluctuations of the AF order [the first term in Eq. (34)]. The latter should be important when the AF moments are strongly localized inside the vortex cores. We expect that proximity-effect-type coupling between neighboring AF vortices should be sufficient to suppress such fluctuations.

In the above discussions we focused on the AF moments of static vortices in the SC state. The $SO(5)$ model has also been extended to study thermally activated phase slips in one-dimensional wires (Sheehy and Goldbart, 1998). One can also construct a dual effect to the AF vortices: Goldbart and Sheehy (1998) proposed AF hedgehogs with SC cores.

B. The pair-density-wave state

In the quantum-disordered phase of the $SO(5)$ model, the hole-pair bosons become localized, forming a pair density wave. Since the superfluid density is low and pairing is strong in the underdoped regime of the high-T_c cuprates, the pair-density-wave state competes with the d-wave SC state. In the global phase diagram shown in Fig. 13, aside from the half-filled AF insulator, there are several possible pair-density-wave states surrounded by the SC phases. In contrast to the superconducting state, which can be realized for any charge density, each pair-density-wave state has a preferred charge density, the dominant one being at doping level $x=1/8$. Since the projected $SO(5)$ model is formulated on the plaquettes of the original lattice, the pair density wave naturally forms a checkerboard pattern, as depicted in Fig. 45. This state has a rotationally symmetric charge periodicity of $4a\times4a$ near doping level $x=1/8$. However, connecting the period of charge modulation to the hole density in realistic systems is not always straightforward. In most cases we find states that have both superconductivity and periodic density modulation. Hence they may be best described as *supersolids*. Supersolid phases are compressible and can accommodate extra charge without changing the period. Expressed differently, the excess charge can always be taken by the superfluid part of the Cooper-pair density without affecting the localized part. The pair-density-wave state differs from the stripe state (Zaanen and Gunnarsson, 1989; Emery *et al.*, 1999), since it does not break the symmetry of $\pi/2$ lattice rotations. It is also distinct from the Wigner crystal of individual holes proposed by Fu *et al.* (2004), which should have a charge periodicity of $\sqrt{8}a\times\sqrt{8}a$ at the same doping level. The pair-density-wave state was first proposed by Chen *et al.* (2002) in the context of the $SO(5)$ theory of the vortex state. It also arises naturally from the plaquette boson approach of Altman and Auerbach (2002). Podolsky *et al.* (2003) discussed how unconventional states with translational symmetry

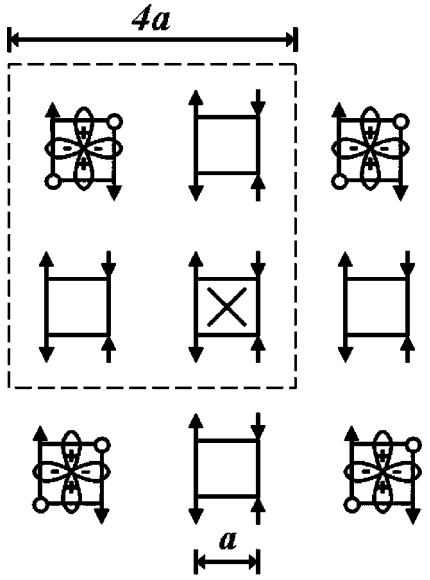

FIG. 45. Illustration of the d-wave pair-density-wave state at $x=1/8$. In this state, the d-wave hole pairs occupy every four nonoverlapping plaquettes on the original lattice. The charge unit cell is $4a\times 4a$. The $SO(5)$ model is defined on the center of the nonoverlapping plaquettes. Such a state could be realized around the vortex core, whose center is depicted by the $\times$ or realized as a generic competing state whenever SC order is reduced. In the actual realization of this state, the hole pair could be much more extended, and the AF ordering could be much reduced from the classical value.

breaking, including the pair-density-wave state, can be detected in scanning tunneling microscope (STM) experiments. The relevance of this state to tunneling experiments has also been considered (Vojta, 2002; Andersen *et al.*, 2003; Chen *et al.*, 2004).

As we can see in the global phase diagram shown in Fig. 13, the pair-density-wave state can be stabilized near doping of $x=1/8$, when the superfluid density (or the kinetic energy of the hole pairs) is small compared to interaction energy. This situation can be realized in the vortex core, near the impurities, in the underdoped cuprates or in the pseudogap phase. The STM experiments of Hoffman *et al.* (2002) measuring the local density of states near the vortex core demonstrated a $4a\times 4a$ checkerboard pattern, consistent with the hole-pair checkerboard state (Chen *et al.*, 2002) shown in Fig. 45. The vortex core can be either positively or negatively charged, depending on whether the bulk density is greater or smaller than that of the nearby pair-density-wave state (Wu *et al.*, 2004). For example, if the chemical potential is such that the bulk SC state is on the left (right) side of the $\delta=1/8$ insulator, we expect the vortex core to have more (less) hole density. The STM experiment of Howald *et al.* (2002) sees a similar real-space modulation without the applied magnetic field, possibly induced by impurities (McElroy *et al.*, 2003). More recently, Vershinin *et al.* (2004) discovered a real-space modulation of the density of states in the pseudogap phase above T_c. Enhancement of the translational symmetry breaking in the pseudogap regime of the cuprates has been proposed theoretically by Sachdev and Demler (2004). The microscopic picture of this phenomenon has been studied by Chen *et al.* (2004) using an extension of the formalism of Podolsky *et al.* (2003) for the pseudogap regime. The analysis of Chen *et al.* (2004) shows that the experimentally observed modulation is inconsistent with an ordinary site-centered charge density wave and the corresponding modulation of the Hartree-Fock potential. However, the pair-density-wave state provides good agreement with the experimental data.

C. Uniform mixed phase of antiferromagnetism and superconductivity

The phase diagram obtained from the classical competition between the AF and SC states is shown in Fig. 10. We have classified the phase transitions broadly into three different types. A type-1 transition involves a direct first-order phase transition between the AF and the SC phases. A type-2 transition involves two second-order phase transitions, with an intermediate phase that is a uniform mixture of AF and SC. The marginal type-1.5 transition describes the special $SO(5)$-symmetric case in which the chemical potential remains constant in the entire uniform mixed phase. Therefore both type-2 and type-1.5 transitions predict a uniform mixed phase of AF and SC.

Evidence for the AF/SC mixed phase exists in the excess-oxygen doped La_2CuO_{4+y}. Neutron-scattering measurements detect the onset of the AF or spin-density-wave orders at the same temperature as the superconducting T_c (Lee *et al.*, 1999). This remarkable coincidence is the hallmark of a multicritical point, which we shall return to later. Because the La_2CuO_{4+y} system has an ordering wave vector similar to that of the $La_{2-x}Sr_xCuO_4$ system, it should also be classified as a class-$B3$ trace in the global phase diagram of Fig. 13, passing through the 1/8 Mott lobe. However, in this case, the Mott phase boundary likely belongs to type 1.5 or 2, where the AF and SC order can coexist.

For $YBa_2Cu_3O_{6+x}$ materials, static magnetic ordering extending to $x\approx 0.5$ has been observed recently using muon spin rotation/relaxation measurements by Miller *et al.* (2003). Preliminary neutron-scattering experiments by Sidis *et al.* (2001) and Mook *et al.* (2002) also have reported magnetic ordering with a wave vector (π,π). Thus, in this case, we have AF coexisting with SC without any additional charge order. However, it is unclear whether two phases coexist uniformly in these materials. Assuming that future experiments verify the existence of a homogeneous phase with AF and SC orders, we conclude that the phase diagram for $YBa_2Cu_3O_{6+x}$ may be understood as moving along the $B1$ line in Fig. 13, when the system avoids all the PDW lobes but has only AF and SC orders either separately or in a uniform mixed phase.

Evidence for the mixed phase of superconductivity and antiferromagnetism has also been obtained recently in the five-layered high-T_c cuprate $HgBa_2Ca_4Cu_5O_y$. In this system, the three inner layers are predominantly antiferromagnetic, while the two outer layers are predominantly superconducting. In a Cu NMR study, Kotegawa *et al.* (2004) obtained firm evidence that the AF inner layers induce a small magnetic moment in the outer layers, establishing the case of an AF/SC uniform mixed phase in this system. However, this type of AF/SC proximity effect was not observed in artificially grown layer structures (Bozovic *et al.*, 2003).

The above discussions show that there is evidence for a uniform mixed phase of AF and SC in the high-T_c cuprates. On the other hand, microscopic probes like scanning tunneling microscopy (Pan *et al.*, 2001) reveal electronic inhomogeneities characteristic of the type-1 direct first-order transition between AF and SC. Therefore, depending on material details, some high-T_c compounds show an AF/SC mixed phase, characteristic of type-2 behavior, while others show microscopic separation between these two phases, a characteristic more consistent with type-1 behavior. It is quite remarkable that such different physical effects can be obtained in materials that are so similar. A reasonable explanation is that these systems are actually very close to the *SO*(5)-symmetric point exhibiting type-1.5 behavior. Only in this case could a slight variation tip the balance towards either the type-1 or type-2 behavior.

A genuine uniform mixed phase of AF and SC has been observed in several heavy-fermion systems in some regions of the pressure (P) -versus-temperature (T) phase diagram (Kitaoka *et al.*, 2001, 2002). Recently, such coexistence was observed through nuclear quadrupole resonance and NMR spectrum measurements in $CeCu_2(Si_{1-x}Ge_x)_2$ with a small concentration, $x=0.01$, of Ge. In $CeCu_2Si_2$, an SC phase coexists with slowly fluctuating magnetic waves. However, for AF $CeCu_2Ge_2$, which has the same lattice and electronic structure as $CeCu_2Si_2$, it was found that a SC phase could be reached at a critical pressure $P_c \sim 7.6$ GPa. Since $CeCu_2Si_2$ behaves at $P=0$ like $CeCu_2Ge_2$ at P_c, it is argued that the SC phase in $CeCu_2Si_2$ occurs close to an AF phase at $P=0$, corresponding to a critical lattice density $D=D_c$. This appears to be the reason for the strong AF fluctuations at $P=0$. A small concentration of Ge expands the unit-cell volume, reducing D below D_c, and is thus sufficient to pin the magnetic fluctuations and to produce AF long-range order within the SC phase. Noting that $D=D_{Si}[1(V_{Ge}-V_{Si})x/V_{Ge}]$ for Ge doping and that D increases with pressure, one can draw a combined phase diagram as a function of lattice density D (Kitaoka *et al.*, 2002).

Kitaoka *et al.* (2002) showed that the phase diagram of Fig. 46 could be understood in terms of an *SO*(5) superspin picture. This suggests that superconductivity in $CeCu_2Si_2$ could be mediated by the same magnetic interactions as those leading to the AF state in $CeCu_2(Si_{1-x}Ge_x)_2$.

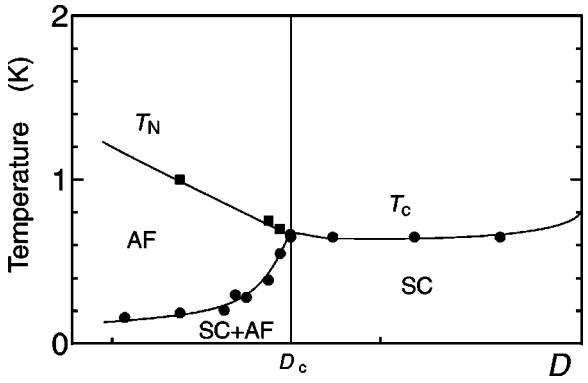

FIG. 46. The combined phase diagram as a function of lattice density D in $CeCu_2(Si_{1-x}Ge_x)_2$ ($D<D_c$) and in $CeCu_2Si_2$ ($D_c \leqslant D$) under pressure P. Note that $D \propto 1/V$, where V is the unit-cell volume, and $D=D_{Si}[1(V_{Ge}-V_{Si})x/V_{Ge}]$ in the former case. From Kitaoka *et al.*, 2002.

D. Global phase diagram and multicritical points

The *SO*(5) theory predicts the existence of a multicritical point where T_N and T_c intersect (see Fig. 10) and also predicts the general topology of the global phase diagram in the space of quantum parameters (see Fig. 13). The goal of this section is to establish the connection between the theoretical quantum phase diagram proposed in Sec. IV.B and the experimental phase diagrams of various families of cuprates. The underlying assumption for making such a connection is that most of the material-specific properties can be absorbed into parameters of the effective Hamiltonian given in Eqs. (50) and (65).

One of the best studied phase diagrams of the high-T_c superconductors is for $La_{2-x}Sr_xCuO_4$. The presence of the stripe order in these materials has been well documented by neutron-scattering experiments (Yamada *et al.*, 1998; Wakimoto *et al.*, 2000, 2001). For less than 5% doping the system is in the insulating regime with diagonal stripes, and for higher dopings the system is superconducting with collinear stripes (see Fig. 47). It is natural to relate this family of cuprates to the $B3$ trajectory on the J/V-μ phase diagram shown in Fig. 13: with increasing μ the system goes through a hierarchy of states at fractional filling factors that correspond to insulating pair-density-wave states. Near these magic filling factors, T_c of the SC state drops dramatically, while magnetic ordering increases substantially. This is indeed the behavior observed in Fig. 47. As discussed in Sec. IV.B, the two possible patterns of charge ordering are checkerboard and stripes. In the case of $La_{2-x}Sr_xCuO_4$, stripe ordering may be stabilized by tilting the CuO_6 octahedron toward the [100] tetragonal direction (parallel to the Cu-O bonds). The phase diagram in Fig. 13 predicts that the ordering wave vectors take discrete values that correspond to different Mott insulating PDW lobes. For long-range interactions, PDW phases are very densely packed, so experimentally we may observe an almost continuous dependence of incommensuration on doping, such as the one discussed by Yamada *et al.* (1998)

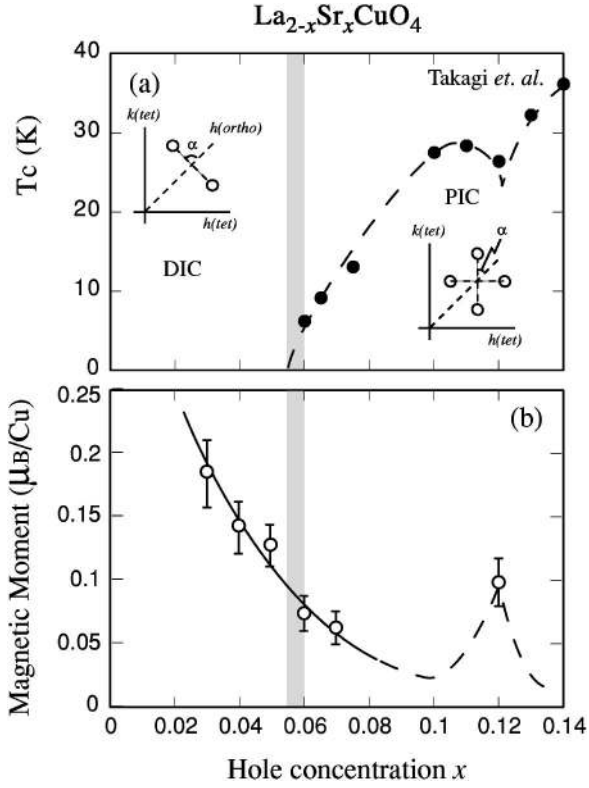

FIG. 47. Doping dependence of the SC transition temperature and magnetic moment for $La_{2-x}Sr_xCuO_4$. From Wakimoto *et al.*, 2001.

and Wakimoto *et al.* (2000). However, different states in the hierarchy are not equivalent. For example, at 1/8 doping we have a very strong insulating phase which corresponds to insulating stripes or a simple checkerboard pattern of Cooper pairs (see Fig. 12). This may explain the famous "1/8 anomaly" in the T_c-vs-doping relation for the $La_{2-x}Sr_xCuO_4$ family of cuprates. Another strong PDW phase is that for 1/16 doping, which may explain why superconductivity disappears close to this filling (see Fig. 47). A staircase of ordering wave vectors for underdoped cuprates has also been discussed in the context of doping the spin-Peierls insulating phase by Vojta and Sachdev (1999) and Sachdev (2002b).

By adding another external parameter we can tune our system continuously between $B1$ and $B3$ trajectories. This was done in recent high-pressure experiments on $La_{1.48}Nd_{0.4}Sr_{0.12}CuO_4$ (Locquet *et al.*, 1998; Sato *et al.*, 2000; Arumugam *et al.*, 2002; Takeshita *et al.*, 2003), in which a pressure of the order of 0.1 GPa was sufficient to suppress stripe ordering at 1/8 doping and stabilize the high-temperature SC phase. Such pressure experiments correspond to moving up along the $A2$ path in Fig. 13. Applying pressure along this path can directly induce a superconductor-to-insulator transition.

In contrast to the LSCO family of high-T_c cuprates, when one varies the carrier density in the YBCO or BSCO cuprates, there is no evidence for the static charge order. In these materials, charge-ordered PDW states can only be realized around vortex cores (Hoffman *et al.*, 2002), when the effective Cooper-pair kinetic energy is reduced, or near impurities (Howald *et al.*, 2002; McElroy *et al.*, 2003; Vershinin *et al.*, 2004). We therefore identify these materials with the $B1$ trajectories in the global phase diagram of Fig. 13. In this case, the AF/SC boundary can be either be type 1 or type 2. Given the evidence discussed in Sec. VII.C, these systems seem to be close to the type-1.5 marginal case in between these two types of phase transition, which means that they should have approximate $SO(5)$ symmetry.

Within the class of materials exhibiting the $B1$ type of trajectory in the global phase diagram, the $SO(5)$ theory makes a distinct prediction of the finite-temperature multicritical point where T_c and T_N intersect. An interesting issue discussed in Secs. IV.C and IV is the possibility of analyzing the critical properties of systems (such as many high-T_c cuprates) showing a direct transition between an AF and a SC phase. In particular, measuring the critical exponent associated with various physical quantities near the bicritical AF-SC point can give information about the dimension of the symmetry group at the transition (Hu and Zhang, 2000). Unfortunately, in the high-T_c cuprates, sample qualities are not high enough to enable a reliable measurement of the critical behavior near the multicritical points discussed above. On the other hand, encouraging experimental evidence for an $SO(5)$ bicritical point does exist in a class of 2D organic superconductors called BEDT salts. These materials share most common physical properties with the cuprates, and the AF-to-SC transition can be induced in them by pressure. In particular, recent experiments on k-(BEDT-TTF)$_2X$ (Kanoda, 1997) revealed an interesting phase diagram in which T_c and T_N intersect each other at a bicritical point. Kanoda (1997) measured the NMR relaxation rate $1/T_1$ in both the AF and the SC region near the bicritical point. Below a characteristic temperature T^*, $1/T_1$ diverged towards the AF transition temperature, while it exhibited a spin-gap-like behavior on the SC side. Murakami and Nagaosa (2000) analyzed these experimental data in terms of a generalized Landau-Ginzburg model including both AF and SC fluctuations near the bicritical point. Their study concentrated on the dynamic critical phenomena, in particular the relaxation rate $1/T_1$ around the bicritical point. A detailed analysis of the data allowed the extraction of the corresponding critical exponent x. Before discussing the NMR linewidth, we would like to caution the reader that there is also a first-order metal-insulator transition in addition to the AF/SC transition discussed here (Lefebvre *et al.*, 2000). The presence of the critical end point of the metal-insulator transition line may lead to some additional complications in the analysis.

On the AF side of the phase diagram, the NMR linewidth is proportional to $(T-T_N)^{-x}$ when approaching T_N from the normal state. For systems far away from the bicritical point, the dynamical critical behavior is governed by the $SO(3)$ Heisenberg model, whose exponent $x=x_3\approx 0.315$. On the other hand, when the $SO(5)$ bicriti-

cal point governs the critical dynamics, the exponent x should change to the $SO(5)$ one, $x=x_5\approx 0.584$, as obtained from the ϵ expansion. In Fig. 48, we present a log-log plot of $1/T_1$ vs $(T-T_c)/T$ (from Murakami and Nagaosa, 2000, data from Kawamoto *et al.*, 1995) for

(A) κ-(BEDT-TTF)$_2$Cu[N(CN)$_2$]Cl (solid squares), and

(B) deuterated κ-(BEDT-TTF)$_2$Cu[N(CN)$_2$]Br (open squares).

System (A) is located in the AF region away from the bicritical point and system (B) is nearly at the bicritical point. As one can see from the figure, the critical exponent, x, is 0.30 ± 0.40 for system (A) and 0.56 ± 0.40 for system (B). These values of x are in reasonably good agreement with the theoretical ones, and, in particular, support the fact that the AF/SC bicritical point is governed by the $SO(5)$-symmetric fixed point. This is the first experiment that directly measures the dimension of the symmetry group close to the AF/SC bicritical point and determines n to be close to 5. More extensive study near the critical region is certainly desirable.

A central issue of the high-T_c cuprates concerns the phase boundary between the AF and SC phases. It is also in this region that the $SO(5)$ theory makes the most direct and distinct predictions. The experiments discussed above seem consistent with the zero-temperature and finite-temperature phase diagrams presented in Figs. 13 and 10. However, a detailed quantitative comparison is still lacking. As the material properties of the high-T_c cuprates improve, direct quantitative tests of the $SO(5)$ theory, such as those performed in the organic superconductors, may become possible.

E. The particle-particle resonance mode in the normal state

In this paper we have discussed the scenario in which the resonance peak in an inelastic neutron-scattering experiment (Rossat-Mignod, Regnault, Vettier, Burlet, *et al.*, 1991; Mook *et al.*, 1993; Fong *et al.*, 1995, 1999; He *et al.*, 2001) originates from the triplet π mode in the particle-particle channel. This mode does not disappear above T_c, but it ceases to contribute to the spin-fluctuation spectrum, since the particle-particle and particle-hole channels are decoupled from each other in the normal state. An important question to ask is whether one can couple to the π channel directly and establish the existence of the resonance already in the normal state. This cannot be done using conventional electromagnetic probes, which all couple to the particle-hole channels only, but it is possible using tunneling experiments. Before we discuss the specific proposal of Bazaliy *et al.* (1997) for detecting π excitations, it is useful to remind the reader about earlier work on measuring pairing fluctuations in conventional superconductors above their transition temperatures (Anderson and Goldman, 1970). As originally proposed by Scalapino (1970), such fluctuations can be measured in a sandwich

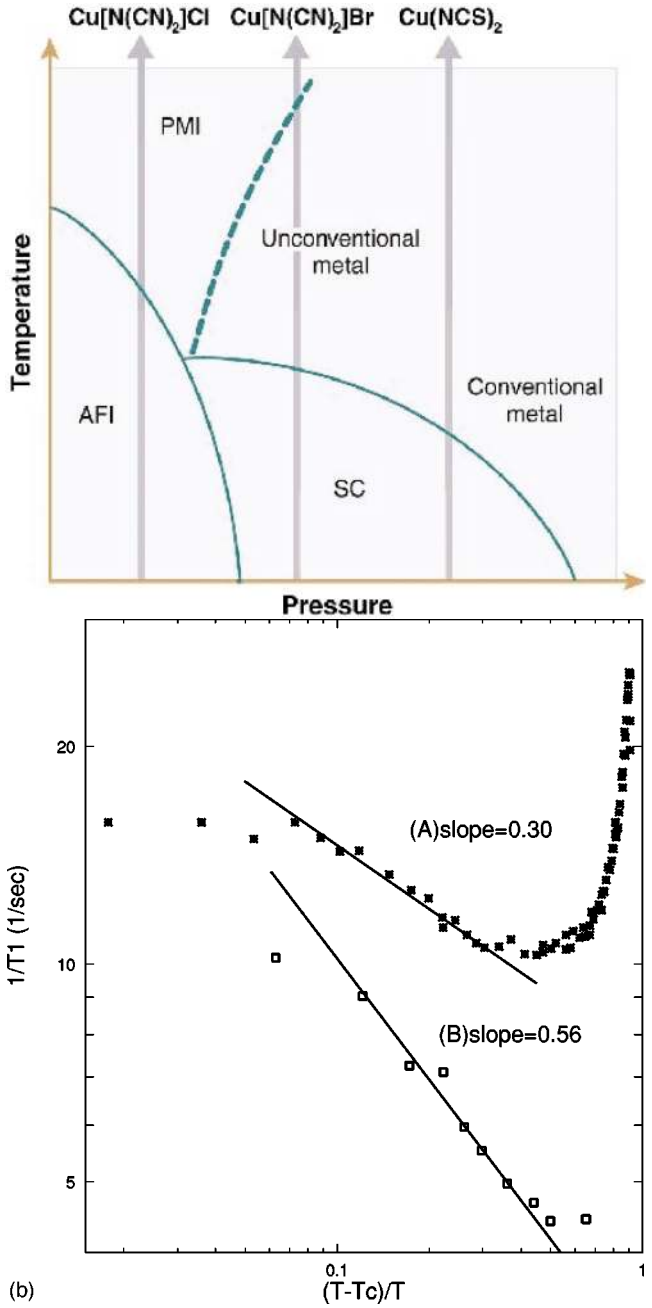

FIG. 48. (Color) Possible $SO(5)$ symmetry in BEDT salts: (a) Phase diagram. From McKenzie, 1997. (b) Log-log plot of T_1^{-1} vs $(T-T_c)/T$ for (A) κ-(BEDT-TTF)$_2$Cu[N(CN)$_2$]Cl (■), and (B) deuterated κ-BEDT-TTF)$_2$Cu[N(CN)$_2$]Br (□). (Data from Kawamoto *et al.*, 1995.)

system of two superconductor SC_1 and SC_2 with different transition temperatures in the regime $T_{c2}<T<T_{c1}$. Resonant coupling between Cooper pairs from the superconductor SC_1 and the fluctuating pairing amplitude in SC_2 leads to the peaks in the IV characteristics at voltages that correspond to half the energy of the preformed Cooper pairs in SC_2. The generalization of these tunneling experiments for detecting the π mode in the normal state of the cuprate has been suggested by Bazaliy *et al.* (1997) and is shown in Fig. 49. In place of the

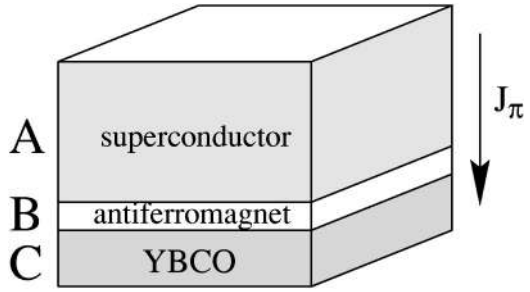

FIG. 49. Setting of the tunneling experiment for detecting the triplet particle-particle π mode in the normal state.

SC_2 region we now have some cuprate material that shows a resonance in the SC state, e.g., an underdoped YBCO (electrode C in Fig. 49), and in place of the SC_1 materials we have a different cuprate superconductor (electrode A in Fig. 49) with a higher transition temperature than material C. The system should be in the temperature regime $T_c^C < T < T_c^A$. The main difference between the setup suggested by Scalapino (1970) and that proposed by Bazaliy *et al.* is the presence of a thin layer of AF insulator between the A and C electrodes. The reason for this modification is straightforward: we need to probe the π channel in the C material that corresponds to the particle-particle mode with spin $S=1$ and momentum $\Pi=(\pi,\pi)$, whereas the SC electrode A provides Cooper pairs with $S=0$ and momentum $q=0$. If the two materials are connected as shown in Fig. 49, a Cooper pair traveling across an AF layer B can emit a magnon, which converts this Cooper pair into a π pair and allows resonant coupling between superconductor A and the π channel of the "normal" electrode C. One expects to find a resonance in the *IV* characteristics of the junction, with a peak in the tunneling current at a voltage exactly half the energy of the π resonance in the C electrode (note that this peak only appears when electrons are injected from A to C, so it appears on one side of the *IV* curve). The simple qualitative picture described above can be made more precise by considering a tunneling Hamiltonian between materials A and C,

$$H_T = \sum_{pk\sigma} T_{pk}^d a_{p\sigma}^\dagger c_{k\sigma} c^{iVt} + T_{pk}^f a_{p+Q\sigma}^\dagger c_{k-\sigma} e^{iVt} + \text{H.c.} \tag{116}$$

Here V is the applied voltage, and the $a_{p\alpha}$ and $c_{k\alpha}$ operators refer to the electronic operators in A and C with momenta p and k. The ratio of the spin-flip matrix element T_{pk}^f to the direct matrix element T_{pk}^d is on the order of Δ_{SDW}/U, where Δ_{SDW} is the spin-density-wave gap of the AF insulating material B. The diagram responsible for the resonant contribution to the tunneling current is shown in Fig. 50. The triplet vertex Γ takes into account interactions needed to create a sharp π resonance in the A electrode. The magnitude of the peak in the tunneling current was estimated by Bazaliy *et al.* (1997) to be 10 μA μV for a system of area 10^{-4} cm^2. As argued in Sec. VI, it is not easy to distinguish the particle-hole and the particle-particle origin of the π resonance below T_c since these two channels are mixed. Direct experimental detection of the triplet particle-particle mode in the normal state would give unambiguous evidence of the particle-particle nature of the π-resonance mode.

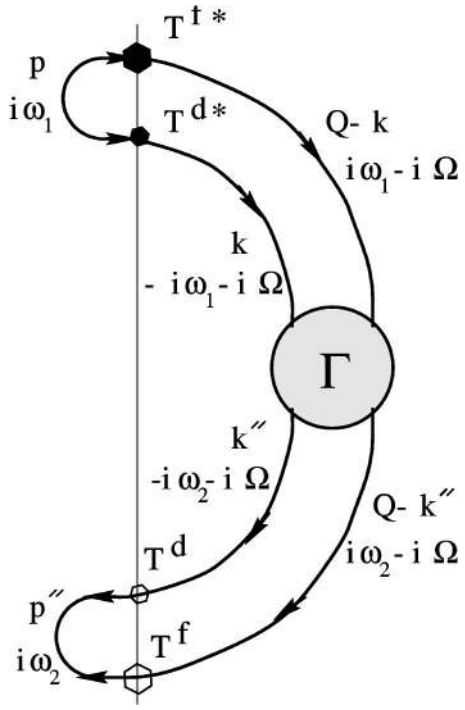

FIG. 50. Second-order tunneling diagram that gives rise to the resonant coupling of Cooper pairs and π excitations in the junction shown in Fig. 49.

F. Josephson effect in SC/AF/SC junctions

When discussing the relationship between *d*-wave superconductivity and antiferromagnetism in the high-T_c cuprates, one often finds signatures of the nearby magnetic phase in experiments performed on the SC materials. An important question to ask is whether the AF insulating phase shows any signatures of the nearby SC state. An intriguing set of experiments that possibly provides such a demonstration has observed long-range proximity effects in insulating samples of $YBa_2Cu_3O_{6+x}$-based materials coupled in the *a-b* plane directions (Barner *et al.*, 1991; Hashimoto *et al.*, 1992; Suzuki *et al.*, 1994; Decca *et al.*, 2000). The AF/SC proximity effect was also observed by Kotegawa *et al.* (2004); however, it seems to be absent in the case of artificially grown *c*-axis coupled layers (Bozovic *et al.*, 2003). The appearance of a long-range proximity effect is very natural from the point of view of the *SO*(5) theory, in which low-energy degrees of freedom correspond to rotation of the order-parameter between the AF and SC configurations. A theory of the long-range proximity effect within the *SO*(5) nonlinear sigma model has been developed by Demler, Berlinsky *et al.* (1998). Let us consider the SC/AF/SC junction shown in Fig. 51. If we set

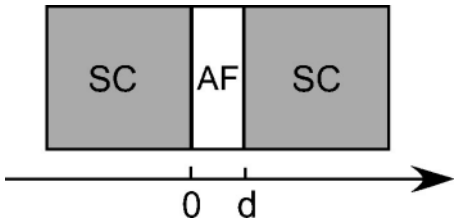

FIG. 51. The superconductor-antiferromagnet-superconductor (SC/AF/SC) junction described by Eq. (117).

Re $\Delta=\cos\theta\cos\phi$, Im $\Delta=\cos\theta\sin\phi$, and $N_3=\sin\theta$, then according to our discussion in Sec. III.B [see Eqs. (36)–(39)], the junction can be described by the effective Lagrangian density

$$\mathcal{L}(\theta,\phi)=\frac{\rho}{2}\{(\partial_i\theta)^2+\cos^2\theta(\partial_i\phi)^2\}-g\sin^2\theta. \tag{117}$$

The anisotropy term is given by $g_A>0$ inside the A region, so that the AF phase would be established in the bulk. In the superconducting regions on both sides of the junction we have $g_S<0$, and we should impose boundary conditions $\theta\to 0$ as $x\to\pm\infty$. As discussed by Demler, Berlinsky, *et al.* (1998), a simplified case corresponds to taking a strong superconductor limit for which $\theta(x=0,d)=0$. The current phase relation can now be obtained by writing the Euler-Lagrange equations for the functional (117) at a fixed current. The maximal value of θ reached at $x=d/2$, θ_0, is determined by the equation

$$\frac{d}{2\xi_A}=\frac{\cos\theta_0}{\sqrt{\omega_s^2+\cos^2\theta_0}}K(k),$$

$$k^2=\frac{\sin^2\theta_0\cos^2\theta_0}{\omega_s^2+\cos^2\theta_0}, \tag{118}$$

where $K(k)$ is the complete elliptic integral of the first kind, the dimensionless current ω_s is equal to $I\xi_A$, with I being the actual current through the junction and the characteristic length is given by

$$\xi_A=\sqrt{\rho/2g_A}. \tag{119}$$

On the other hand, the equation for the phase difference across the junction, $\Delta\Phi$, is given by

$$\Delta\Phi=2\omega_s-\frac{\cos\theta_0}{\sqrt{\omega_s^2+\cos^2\theta_0}}\Pi_1(-\sin^2\theta_0,k). \tag{120}$$

Here $\Pi_1(n,k)$ is a complete elliptic integral of the third kind. Immediately, one can see that Eq. (120) describes two different kinds of behavior for d larger or smaller than $d_{c0}=\pi\xi_A$. When $d>d_{c0}$ we have a conventional proximity effect with $I(\Delta\Phi)=I_0(d)\sin\Delta\Phi$ and $I_0(d)\propto\exp(-d/\xi_A)$. We observe, however, that the SC correlation length ξ_A may be very long if the system is close to the *SO*(5)-symmetric point [$g_A\to 0$ in Eq. (119)], which corresponds to the long-range proximity effect. When $d<d_{c0}$ we get more intriguing behavior in Eq. (120), in which for small currents the A region is uniformly superconducting, i.e., $\theta_0=0$ (proximity to a strong superconductor completely suppresses the AF order inside the A region), but when the current exceeds some critical value, the system goes into a state that has both d-wave SC and AF orders, i.e., $0<\theta_0<\pi/2$. The resulting nontrival $I(\Delta\Phi)$ are shown in Fig. 52. We note that the analysis presented above does not take into account the long-range part of the Coulomb interaction between electrons. This may become important for systems with sufficiently wide AF layers and lead to suppression of the proximity-induced SC order in the AF layer.

Several consequences of the nonsinusoidal behavior of the current-phase relation in SAS junctions have been explored by den Hertog *et al.* (1999), including current-voltage characteristics in the presence of thermal fluctuations, Shapiro steps, and the Fraunhofer pattern. Decca *et al.* (2000) used near-field scanning tunneling microscopy to photogenerate Josephson junctions in underdoped thin films of $YBa_2Cu_8O_{6+x}$. They have verified a long-range proximity effect through insulating layers but observed a conventional Fraunhofer pattern rather than the one predicted by den Hertog *et al.* (1999). The geometry of their samples, however, is different from that of the system studied by Demler, Berlinsky, *et al.* (1998) and den Hertog *et al.* (1999): the intermediate AF layer in their case is connected to large AF regions on both sides of the junctions, which suppresses rotation of the superspin in the SC direction.

In a related context, Auerbach and Altman (2000) applied the projected *SO*(5) theory to predict multiple Andreev resonance peaks in SC/AF/SC junctions.

VIII. CONCLUSIONS

In a large class of materials, including the high-T_c cuprates, the organic superconductors, and the heavy-fermion compounds, the AF and SC phases occur in close proximity to each other. The *SO*(5) theory is developed based on the assumption that these two phases share a common microscopic origin and should be treated on an equal footing. The *SO*(5) theory gives a coherent description of the rich global phase diagram of the high-T_c cuprates and its low-energy dynamics through a simple symmetry principle and a unified effective model based on a single quantum Hamiltonian. A number of theoretical predictions, including the intensity dependence of the neutron resonance mode, the AF vortex state, the pair-density-wave state, and the mixed phase of AF and SC, have been verified experimentally. The theory also sheds light on the microscopic mechanism of superconductivity and quantitatively correlates the AF exchange energy with the condensation energy of superconductivity. However, the theory is still incomplete in many ways and lacks full quantitative predictive power. While the role of fermions is well understood within the exact *SO*(5) models, their roles in the projected *SO*(5) models are still not fully worked out. As a result, the theory has not made many predictions concerning the transport properties of these materials.

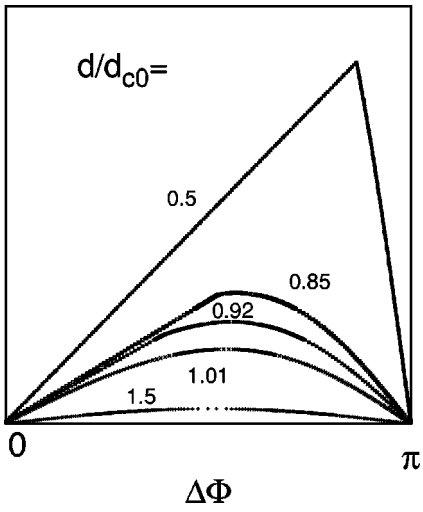

FIG. 52. Predicted current-phase characteristics of a SC/AF/SC junction with different d/d_{c0}.

Historically, throughout man's quest for the basic laws of nature, symmetry principles have always been a faithful guiding light which time and again led us out of darkness. The enigma of high-temperature superconductivity poses an unprecedented challenge in condensed-matter physics. Reflecting upon the historical developments of physical theories, it seems worthwhile to carry out the symmetry approach to this problem to its full logical conclusion. The basic idea of unifying seemingly different phases by a common symmetry principle may also prove to be useful for other strongly correlated systems.

IX. NOTATIONS AND CONVENTIONS

A. Index convention

τ^{α} denote Pauli matrices.

$\alpha,\beta=x,y,z$ denote $SO(3)$ vector spin indices.

$\sigma,\sigma'=1,2$ denote $SO(3)$ spinor indices.

$a,b,c=1,2,3,4,5$ denote $SO(5)$ superspin vector indices.

$\mu,\nu=1,2,3,4$ denote $SO(5)$ spinor indices.

$i,j=1,5$ denote $U(1)$ vector indices for superconductivity.

x,x' denote site indices.

B. Dirac Γ matrices

The general method introduced by Rabello *et al.* (1998) for constructing $SO(5)$-symmetric models uses the five Dirac Γ matrices, Γ_a $(a=1,\ldots,5)$, which satisfy the Clifford algebra,

$$\{\Gamma^a,\Gamma^b\}=2\delta^{ab}. \tag{121}$$

Rabello *et al.* introduced the following explicit representation, which is naturally adapted for discussing the unification of AF and d-wave SC order parameters:

$$\Gamma^1=\begin{pmatrix}0 & -i\tau_y\\ i\tau_y & 0\end{pmatrix},\quad \Gamma^{(2,3,4)}=\begin{pmatrix}\vec{\tau} & 0\\ 0 & {}^t\vec{\tau}\end{pmatrix},$$
$$\Gamma^5=\begin{pmatrix}0 & \tau_y\\ \tau_y & 0\end{pmatrix}. \tag{122}$$

Here $\vec{\tau}=(\tau_x,\tau_y,\tau_z)$ are the usual Pauli matrices and ${}^t\vec{\tau}$ denotes their transposition. These five Γ_a matrices form the five-dimensional vector irreps of $SO(5)$. Their commutators,

$$\Gamma^{ab}=-\frac{i}{2}[\Gamma^a,\Gamma^b], \tag{123}$$

define the ten-dimensional antisymmetric tensor irreps of $SO(5)$. In the above representation, the 10 Γ^{ab}'s are given explicitly by

$$\Gamma^{15}=\begin{pmatrix}-1 & 0\\ 0 & 1\end{pmatrix},$$

$$\Gamma^{(i+1)(j+1)}=\varepsilon_{ijk}\begin{pmatrix}\tau_k & 0\\ 0 & -{}^t\tau_k\end{pmatrix}\quad (i,j=1,2,3),$$

$$\Gamma^{(2,3,4)1}=\begin{pmatrix}0 & -\vec{\tau}\tau_y\\ -\tau_y\vec{\tau} & 0\end{pmatrix}=\tau_y\begin{pmatrix}0 & {}^t\vec{\tau}\\ -\vec{\tau} & 0\end{pmatrix},$$

$$\Gamma^{(2,3,4)5}=\begin{pmatrix}0 & -i\vec{\tau}\tau_y\\ i\tau_y\vec{\tau} & 0\end{pmatrix}=i\tau_y\begin{pmatrix}0 & {}^t\vec{\tau}\\ \vec{\tau} & 0\end{pmatrix}.$$

These Γ matrices satisfy the following commutation relations:

$$[\Gamma^{ab},\Gamma^c]=2i(\delta_{ac}\Gamma^b-\delta_{bc}\Gamma^a), \tag{124}$$

$$[\Gamma^{ab},\Gamma^{cd}]=2i(\delta_{ac}\Gamma^{bd}+\delta_{bd}\Gamma^{ac}-\delta_{ad}\Gamma^{bc}-\delta_{bc}\Gamma^{ad}). \tag{125}$$

An important property of the $SO(5)$ Lie algebra is the pseudoreality of its spinor representation. This means that there exists a matrix R with the following properties:

$$R^2=-1,\ R^{\dagger}=R^{-1}={}^tR=-R, \tag{126}$$

$$R\Gamma^aR=-{}^t\Gamma^a,\ R\Gamma^{ab}R={}^t\Gamma^{ab}. \tag{127}$$

The relations $R\Gamma^{ab}R^{-1}=-(\Gamma^{ab})^*$ indicate that the spinor representation is real, and the antisymmetric nature of the matrix R indicates that it is pseudoreal. The R matrix plays a role similar to that of $\epsilon_{\alpha\beta}$ in $SO(3)$. In our representation, the R matrix takes the form

$$R=\begin{pmatrix}0 & 1\\ -1 & 0\end{pmatrix}. \tag{128}$$

ACKNOWLEDGMENTS

We would first like to thank E. Arrigoni, H. D. Chen, C. Dahnken, J. Schafer, and C. J. Wu for their kind help

with the manuscript preparation. We have benefited from long-term collaborations, discussions, and exchanges of ideas and results with a large number of colleagues. We particularly mention G. Aeppli, E. Altman, P. Anderson, D. Arovas, G. Arnold, E. Arrigoni, A. Auerbach, S. Balatsky, G. Baskaran, Y. Bazaliy, M. Beasley, J. Berlinsky, D. Bonn, G. Bloomberg, J. Brewer, S. Brown, C. Burgess, J. C. Campuzano, S. Capponi, S. Chakravarty, K. Chaltikian, H. D. Chen, P. Chu, A. Chubukov, P. Coleman, P. C. Dai, E. Dagotto, K. Damle, S. Das Sarma, J. C. Davis, D. Dessau, C. DiCastro, S. Doniach, A. Dorneich, R. Eder, Y. Endoh, D. Fisher, M. P. A. Fisher, E. Fradkin, M. Franz, H. Fukuyama, A. Furusaki, T. Geballe, S. Girvin, M. Greiter, B. Halperin, W. Halperin, W. Hardy, P. Hedegard, C. Henley, I. Herbut, J. Hoffman, J. P. Hu, X. Hu, M. Imada, C. Kallin, A. Kapitulnik, H. Y. Kee, B. Keimer, B. Khaykovich, R. Kiefl, Y. B. Kim, S. Kivelson, Y. Kitaoka, M. Klein, W. Kohn, H. Kohno, R. Laughlin, D. H. Lee, T. K. Lee, P. Lee, Y. S. Lee, H. Q. Lin, J. Loram, S. Maekawa, R. Markiewicz, I. Martin, B. Marston, I. Mazin, R. Miller, A. Millis, K. Moler, H. Mook, A. Moreo, S. Murakami, N. Nagaosa, C. Nayak, D. Nelson, T. K. Ng, M. Norman, M. Ogata, J. Orestein, P. Ong, D. Pines, D. Podolsky, A. Polkovnikov, L. Pryadko, S. Rabello, S. Sachdev, S. H. Salk, G. Sawatzky, D. Scalapino, R. Scalettar, R. Schrieffer, D. Senechal, T. Senthil, Z. X. Shen, M. Sigrist, S. Sondhi, S. Sorrela, P. Stamp, L. Taillefer, Z. Tesanovic, M. Tinkham, A. M. Tremblay, D. van der Marel, F. Wegner, X. G. Wen, S. White, M. K. Wu, A. Yazdani, J. Zaanen, M. Zacher, G. Zarand, F. C. Zhang, G. Q. Zheng, and G. Zimanyi. E.D. was supported by NSF Grant No. DMR-0132874 and by the Sloan Foundation. W.H. was supported by the DFG under Grant No. Ha 1537/16-2. S.-C.Z. was supported by the NSF under Grant No. DMR-9814289 and the U.S. Department of Energy, Office of Basic Energy Sciences under Contract No. DE-AC03-76SF00515.

REFERENCES

Abanov, A., A. V. Chubukov, and J. Schmalian, 2001, J. Electron Spectrosc. Relat. Phenom. **117**, 129.

Abrikosov, A. A., 2000, Physica C **341-348**, 97.

Abrikosov, A. A., L. P. Gorkov, and I. E. Dzyaloshinski, 1993, *Methods of Quantum Field Theory in Statistical Physics* (Dover, New York).

Affleck, I., and J. B. Marston, 1988, Phys. Rev. B **37**, 3774.

Aharony, A., 2002, Phys. Rev. Lett. **88**, 059703.

Alama, S., A. J. Berlinsky, L. Bronsard, and T. Giorgi, 1999, Phys. Rev. B **60**, 6901.

Allen, S., H. Touchette, S. Moukouri, Y. M. Vilk, and A. M. S. Tremblay, 1999, Phys. Rev. Lett. **83**, 4128.

Altman, E., and A. Auerbach, 2002, Phys. Rev. B **65**, 104508.

Andersen, B. M., H. Bruus, and P. Hedegard, 2000, Phys. Rev. B **61**, 6298.

Andersen, B. M., P. Hedegard, and H. Bruus, 2003, J. Low Temp. Phys. **131**, 281.

Anderson, J. T., and A. M. Goldman, 1970, Phys. Rev. Lett. **25**, 743.

Anderson, P. W., 1987, Science **235**, 1196.

Anderson, P. W., 1997, *The Theory of Superconductivity in the High-T_c Cuprate Superconductors* (Princeton University, Princeton, NJ).

Anderson, P. W., P. A. Lee, M. Randeria, T. M. Rice, N. Trivedi, and F. C. Zhang, 2003, cond-mat/0311467.

Ando, Y., G. S. Boebinger, A. Passner, T. Kimura, and K. Kishio, 1995, Phys. Rev. Lett. **75**, 4662.

Ando, Y., G. S. Boebinger, A. Passner, N. L. Wang, C. Geibel, and F. Steglich, 1996, Phys. Rev. Lett. **77**, 2065.

Arovas, D. P., A. J. Berlinsky, C. Kallin, and S. C. Zhang, 1997, Phys. Rev. Lett. **79**, 2871.

Arrigoni, E., and W. Hanke, 1999, Phys. Rev. Lett. **82**, 2115.

Arrigoni, E., and W. Hanke, 2000, Phys. Rev. B **62**, 11770.

Arumugam, S., N. Mori, N. Takeshita, H. Takashima, T. Noda, H. Eisaki, and S. Uchida, 2002, Phys. Rev. Lett. **88**, 247001.

Assaad, F. F., and M. Imada, 1998, Phys. Rev. B **58**, 1845.

Auerbach, A., 1994, *Interacting Electrons and Quantum Magnetism* (Springer, New York).

Auerbach, A., and E. Altman, 2000, Phys. Rev. Lett. **85**, 3480.

Auerbach, A., F. Berruto, and L. Capriotti, 2000, in *Field Theories for Low-dimensional Condensed Matter Systems—Spin Systems and Strongly Correlated Electrons*, edited by G. Morandi, P. Sodano, A. Tagliacozzo, and V. Tognetti (Springer, New York), Chap. 5.

Balents, L., M. P. A. Fisher, and C. Nayak, 1998, Int. J. Mod. Phys. B **12**, 1033.

Balents, L., M. P. A. Fisher, and C. Nayak, 1999, Phys. Rev. B **60**, 1654.

Bardasis, A., and J. R. Schrieffer, 1961, Phys. Rev. **121**, 1050.

Bardeen, J., L. N. Cooper, and J. R. Schrieffer, 1957, Phys. Rev. **108**, 1175.

Barner, J. B., C. T. Rogers, A. Inam, R. Ramesh, and S. Bersey, 1991, Appl. Phys. Lett. **59**, 742.

Barzykin, V., and D. Pines, 1995, Phys. Rev. B **52**, 13 585.

Baskaran, G., and P. W. Anderson, 1998, J. Phys. Chem. Solids **59**, 1780.

Bazaliy, Y. B., E. Demler, and S. C. Zhang, 1997, Phys. Rev. Lett. **79**, 1921.

Bednorz, J. G., and K. A. Müller, 1986, Z. Phys. B: Condens. Matter **64**, 189.

Bernardet, K., G. G. Batrouni, J. L. Meunier, G. Schmid, M. Troyer, and A. Dorneich, 2002, Phys. Rev. B **65**, 104519.

Blumberg, G., B. P. Stojkovic, and M. V. Klein, 1995, Phys. Rev. B **52**, 15 741.

Boebinger, G. S., Y. Ando, A. Passner, T. Kimura, M. Okuya, J. Shimoyama, K. Kishio, K. Tamasaku, N. Ichikawa, and S. Uchida, 1996, Phys. Rev. Lett. **77**, 5417.

Bouwknegt, P., and K. Schoutens, 1999, Phys. Rev. Lett. **82**, 2757.

Bozovic, I., G. Logvenov, M. A. J. Verhoeven, P. Caputo, E. Goldobin, and T. H. Geballe, 2003, Nature (London) **422**, 873.

Brewer, J. H., E. J. Ansaldo, J. F. Carolan, A. C. D. Chaklader, W. N. Hardy, D. R. Harshman, M. E. Hayden, M. Ishikawa, N. Kaplan, R. Keitel, J. Kempton, R. F. Kiefl, *et al.*, 1988, Phys. Rev. Lett. **60**, 1073.

Brinckmann, J., and P. A. Lee, 1999, Phys. Rev. Lett. **82**, 2915.

Bruder, C., R. Fazio, and G. Schon, 1993, Phys. Rev. B **47**, 342.

Bruus, H., K. A. Eriksen, M. Hallundbaek, and P. Hedegard, 1999, Phys. Rev. B **59**, 4349.

Bulut, N., and D. J. Scalapino, 1996, Phys. Rev. B **53**, 5149.

Burgess, C. P., J. M. Cline, R. MacKenzie, and R. Ray, 1998, Phys. Rev. B **57**, 8549.

Calabrese, P., A. Pelissetto, and E. Vicari, 2003, Phys. Rev. B **67**, 054505.
Calandra, M., and S. Sorella, 2000, Phys. Rev. B **61**, R11 894.
Campuzano, J. C., M. R. Norman, and M. Randeria, 2002, in *Physics of Conventional and Unconventional Superconductors*, edited by K. H. Bennemann and J. B. Ketterson (Springer, New York).
Capponi, S., and D. Poilblanc, 2002, Phys. Rev. B **66**, 180503.
Carbotte, J. P., E. Schachinger, and D. D. Branch, 1999, J. Low Temp. Phys. **117**, 217.
Carlson, E. W., V. J. Emery, S. A. Kivelson, and D. Orgad, 2002, in *The Physics of Conventional and Unconventional Superconductors*, edited by K. H. Bennemann and J. B. Ketterson (Springer, New York).
Chakravarty, S., B. I. Halperin, and D. R. Nelson, 1988, Phys. Rev. Lett. **60**, 1057.
Chakravarty, S., and H. Y. Kee, 2000, Phys. Rev. B **61**, 14 821.
Chakravarty, S., H.-Y. Kee, and E. Abrahams, 1999, Phys. Rev. Lett. **82**, 2366.
Chakravarty, S., R. B. Laughlin, D. K. Morr, and C. Nayak, 2001, Phys. Rev. B **63**, 094503.
Chen, H.-D., S. Capponi, F. Alet, and S.-C. Zhang, 2003, cond-mat/0312660.
Chen, H. D., J. P. Hu, S. Capponi, E. Arrigoni, and S. C. Zhang, 2002, Phys. Rev. Lett. **89**, 137004.
Chen, H.-D., O. Vafek, A. Yazdani, and S.-C. Zhang, 2004, cond-mat/0402323.
Chen, H. D., C. J. Wu, and S. C. Zhang, 2003, cond-mat/0310289.
Chen, Y., and C. S. Ting, 2002, Phys. Rev. B **65**, 180513.
Chubukov, A., D. Pines, and J. Schmalian, 2003, in *The Physics of Superconductors*, edited by K. H. Bennemann and J. B. Ketterson (Springer, New York), pp. 450–490.
Curro, N. J., C. Milling, J. Haase, and C. P. Slichter, 2000, Phys. Rev. B **62**, 3473.
Dagotto, E., 1994, Rev. Mod. Phys. **66**, 763.
Dai, P., M. Yethiraj, H. A. Mook, T. B. Lindemer, and F. Dogan, 1996, Phys. Rev. Lett. **77**, 5425.
Dai, P. C., H. A. Mook, G. Aeppli, S. M. Hayden, and F. Dogan, 2000, Nature (London) **406**, 965.
Dai, P. C., H. A. Mook, and F. Dogan, 1998, Phys. Rev. Lett. **80**, 1738.
Dai, P. C., H. A. Mook, S. M. Hayden, G. Aeppli, T. G. Perring, R. D. Hunt, and F. Dogan, 1999, Science **284**, 1344.
Damascelli, A., Z. Hussain, and Z. X. Shen, 2003, Rev. Mod. Phys. **75**, 473.
Decca, R. S., H. D. Drew, E. Osquiguil, B. Maiorov, and J. Guimpel, 2000, Phys. Rev. Lett. **85**, 3708.
Demler, E., A. J. Berlinsky, C. Kallin, G. B. Arnold, and M. R. Beasley, 1998, Phys. Rev. Lett. **80**, 2917.
Demler, E., H. Kohno, and S. C. Zhang, 1998, Phys. Rev. B **58**, 5719.
Demler, E., S. Sachdev, and Y. Zhang, 2001, Phys. Rev. Lett. **87**, 067202.
Demler, E., and S. C. Zhang, 1995, Phys. Rev. Lett. **75**, 4126.
Demler, E., and S. C. Zhang, 1998, Nature (London) **396**, 733.
Demler, E., and S. C. Zhang, 1999a, Ann. Phys. (N.Y.) **271**, 83.
Demler, E., and S. C. Zhang, 1999b in *High Temperature Superconductivity: Coral Cables, Florida*, January 1999, edited by S. E. Barnes, J. Ashkenazi, J. L. Cohn, and F. Zuo (AIP, Melville, NY), pp. 30–35.
Demler, E., S. C. Zhang, N. Bulut, and D. J. Scalapino, 1996, Int. J. Mod. Phys. B **10**, 2137.
den Hertog, B. C., A. J. Berlinsky, and C. Kallin, 1999, Phys. Rev. B **59**, R11 645.
Doniach, S., and M. Inui, 1990, Phys. Rev. B **41**, 6668.
Dopf, G., A. Muramatsu, and W. Hanke, 1992, Phys. Rev. Lett. **68**, 353.
Dorneich, A., W. Hanke, E. Arrigoni, M. Troyer, and S. C. Zhang, 2002a, J. Phys. Chem. Solids **63**, 1365.
Dorneich, A., W. Hanke, E. Arrigoni, M. Troyer, and S. C. Zhang, 2002b, Phys. Rev. Lett. **88**, 057003.
Dorneich, A., and M. Troyer, 2001, Phys. Rev. E **64**, 066701.
Duffy, D., S. Haas, and E. Kim, 1998, Phys. Rev. B **58**, R5932.
Eder, R., A. Dorneich, M. G. Zacher, W. Hanke, and S. C. Zhang, 1999, Phys. Rev. B **59**, 561.
Eder, R., W. Hanke, and S. C. Zhang, 1998, Phys. Rev. B **57**, 13 781.
Emery, V. J., and S. A. Kivelson, 1995, Nature (London) **374**, 434.
Emery, V. J., S. A. Kivelson, and J. M. Tranquada, 1999, Proc. Natl. Acad. Sci. U.S.A. **96**, 8814.
Eschrig, M., and M. R. Norman, 2000, Phys. Rev. Lett. **85**, 3261.
Fjaerstad, J. O., and J. B. Marston, 2002, Phys. Rev. B **65**, 125106.
Fisher, M. E., M. N. Barber, and D. Jasnow, 1973, Phys. Rev. A **8**, 1111.
Fisher, M. P. A., P. B. Weichman, G. Grinstein, and D. S. Fisher, 1989, Phys. Rev. B **40**, 546.
Fong, H. F., P. Bourges, Y. Sidis, L. P. Regnault, J. Bossy, A. Ivanov, D. L. Milius, I. A. Aksay, and B. Keimer, 1999, Phys. Rev. Lett. **82**, 1939.
Fong, H. F., P. Bourges, Y. Sidis, L. P. Regnault, J. Bossy, A. Ivanov, D. L. Milius, I. A. Aksay, and B. Keimer, 2000, Phys. Rev. B **61**, 14 773.
Fong, H. F., B. Keimer, P. W. Anderson, D. Reznik, F. Dogan, and I. A. Aksay, 1995, Phys. Rev. Lett. **75**, 316.
Fong, H. F., B. Keimer, D. Reznik, D. L. Milius, and I. A. Aksay, 1996, Phys. Rev. B **54**, 6708.
Frahm, H., and M. Stahlsmeier, 2001, Phys. Rev. B **63**, 125109.
Franz, M., D. E. Sheehy, and Z. Tesanovic, 2002, Phys. Rev. Lett. **88**, 257005.
Franz, M., and Z. Tesanovic, 2001, Phys. Rev. B **63**, 064516.
Franz, M., Z. Tesanovic, and O. Vafek, 2002, Phys. Rev. B **66**, 054535.
Fu, H. C., J. C. Davis, and D. H. Lee, 2004, cond-mat/0403001.
Fujimori, A., A. Ino, T. Mizokawa, C. Kim, Z. X. Shen, T. Sasagawa, T. Kimura, K. Kishio, M. Takaba, K. Tamasaku, H. Eisaki, and S. Uchidau, 1998, J. Phys. Chem. Solids **59**, 1892.
Fujita, M., M. Matsuda, S. Katano, and K. Yamada, 2003, cond-mat/0311269.
Furusaki, A., and S. C. Zhang, 1999, Phys. Rev. B **60**, 1175.
Georgi, H., 1982, *Lie Algebras in Particle Physics* (Addison-Wesley, Reading, MA).
Ghosal, A., C. Kallin, and A. J. Berlinsky, 2002, Phys. Rev. B **66**, 214502.
Goldbart, P. M., and D. E. Sheehy, 1998, Phys. Rev. B **58**, 5731.
Gopalan, S., T. M. Rice, and M. Sigrist, 1994, Phys. Rev. B **49**, 8901.
Greiner, M., 2002, Nature (London) **415**, 39.
Greiter, M., 1997, Phys. Rev. Lett. **79**, 4898.
Gros, C., 1989, Ann. Phys. (N.Y.) **189**, 53.
Halperin, B. I., T. C. Lubensky, and S. K. Ma, 1974, Phys. Rev. Lett. **32**, 292.
Han, J. H., and D. H. Lee, 2000, Phys. Rev. Lett. **85**, 1100.

Harada, K., and N. Kawashima, 1997, Phys. Rev. B **55**, R11 949.
Hashimoto, T., M. Sagoi, Y. Mizutani, J. Yoshida, and K. Mizushima, 1992, Appl. Phys. Lett. **60**, 1756.
He, H., P. Bourges, Y. Sidis, C. Ulrich, L. P. Regnault, S. Pailhes, N. S. Berzigiarova, N. N. Kolesnikov, and B. Keimer, 2002, Science **295**, 1045.
He, H., Y. Sidis, P. Bourges, G. D. Gu, A. Ivanov, N. Koshizuka, B. Liang, C. T. Lin, L. P. Regnault, E. Schoenherr, and B. Keimer, 2001, Phys. Rev. Lett. **86**, 1610.
Hebert, F., G. G. Batrouni, R. T. Scalettar, G. Schmid, M. Troyer, and A. Dorneich, 2002, Phys. Rev. B **65**, 014513.
Henley, C. L., 1998, Phys. Rev. Lett. **80**, 3590.
Herbut, I. F., 2002, Phys. Rev. Lett. **88**, 047006.
Hill, R. W., C. Proust, L. Taillefer, P. Fournier, and R. L. Greene, 2001, Nature (London) **414**, 711.
Himeda, A., and M. Ogata, 1999, Phys. Rev. B **60**, R9935.
Hirsch, J. E., and F. Marsiglio, 2000, Phys. Rev. B **62**, 15 131.
Hirsch, J. E., S. Tang, E. Loh, and D. J. Scalapino, 1988, Phys. Rev. Lett. **60**, 1668.
Hoffman, J. E., E. W. Hudson, K. M. Lang, V. Madhavan, H. Eisaki, S. Uchida, and J. C. Davis, 2002, Science **295**, 466.
Hofstetter, W., J. I. Cirac, P. Zoller, E. Demler, and M. D. Lukin, 2002, Phys. Rev. Lett. **89**, 220407.
Hong, S. P., and S. H. S. Salk, 1999, Physica B **261**, 1053.
Howald, C., H. Eisaki, N. Kaneko, M. Greven, and A. Kapitulnik, 2002, cond-mat/0208442.
Howald, C., R. Fournier, and A. Kapitulnik, 2001, Phys. Rev. B **64**, 100504.
Hu, J.-P., and S.-C. Zhang, 2000, Physica C **431**, 93.
Hu, J. P., and S. C. Zhang, 2001, Phys. Rev. B **64**, 100502.
Hu, J. P., and S. C. Zhang, 2002, J. Phys. Chem. Solids **63**, 2277.
Hu, X., 1999a, cond-mat/9906237.
Hu, X., 1999b, J. Low Temp. Phys. **117**, 289.
Hu, X., 2001, Phys. Rev. Lett. **87**, 057004.
Imada, M., A. Fujimori, and Y. Tokura, 1998, Rev. Mod. Phys. **70**, 1039.
Ino, A., T. Mizokawa, A. Fujimori, K. Tamasaku, H. Eisaki, S. Uchida, T. Kimura, T. Sasagawa, and K. Kishio, 1997, Phys. Rev. Lett. **79**, 2101.
Inui, M., S. Doniach, P. Hirschfeld, and A. E. Ruckenstein, 1988, Phys. Rev. B **37**, 2320.
Ioffe, L. B., and A. J. Millis, 2002, J. Phys. Chem. Solids **63**, 2259.
Jaksch, D., C. Bruder, J. I. Cirac, C. W. Gardiner, and P. Zoller, 1998, Phys. Rev. Lett. **81**, 3108.
Jerome, D., A. Mazaud, M. Ribault, and K. Bechgaard, 1980, J. Phys. (Paris), Lett. **41**, L95.
Johnson, P. D., T. Valla, A. V. Fedorov, Z. Yusof, B. O. Wells, Q. Li, A. R. Moodenbaugh, G. D. Gu, N. Koshizuka, C. Kendziora, Jian Sha, and D. G. Hinks, 2001, Phys. Rev. Lett. **87**, 177007.
Jöstingmeier, M., A. Dorneich, E. Arrigoni, W. Hanke, and S.-C. Zhang, 2003, Phys. Rev. B **68**, 245111.
Juneau, M., R. MacKenzie, M. A. Vachon, and J. M. Cline, 2002, Phys. Rev. B **65**, 140512.
Kakuyanagi, K., K. Kumagai, and Y. Matsuda, 2002, J. Phys. Chem. Solids **63**, 2305.
Kakuyanagi, K., K. Kumagai, Y. Matsuda, and M. Hasegawa, 2003, Phys. Rev. Lett. **90**, 197003.
Kang, H. J., P. C. Dai, J. W. Lynn, M. Matsuura, J. R. Thompson, S. C. Zhang, D. N. Argyriou, Y. Onose, and Y. Tokura, 2003, Nature (London) **423**, 522.
Kanoda, K., 1997, Hyperfine Interact. **104**, 235.
Kastner, M. A., R. J. Birgeneau, G. Shirane, and Y. Endoh, 1998, Rev. Mod. Phys. **70**, 897.
Katano, S., M. Sato, K. Yamada, T. Suzuki, and T. Fukase, 2000, Phys. Rev. B **62**, R14 677.
Kawamoto, A., K. Miyagawa, Y. Nakazawa, and K. Kanoda, 1995, Phys. Rev. B **52**, 15 522.
Kee, H. Y., S. A. Kivelson, and G. Aeppli, 2002, Phys. Rev. Lett. **88**, 257002.
Keimer, B., 2004, private communication.
Khaykovich, B., Y. S. Lee, R. W. Erwin, S. H. Lee, S. Wakimoto, K. J. Thomas, M. A. Kastner, and R. J. Birgeneau, 2002, Phys. Rev. B **66**, 014528.
Kitaoka, Y., K. Ishida, Y. Kawasaki, O. Trovarelli, C. Geibel, and F. Steglich, 2001, J. Phys.: Condens. Matter **13**, L79.
Kitaoka, Y., Y. Kawasaki, T. Mito, S. Kawasaki, G. Q. Zheng, K. Ishida, D. Aoki, Y. Haga, R. Settai, Y. Onuki, C. Geibel, and F. Steglich, 2002, J. Phys. Chem. Solids **63**, 1141.
Kivelson, S., D. H. Lee, and S. C. Zhang, 1992, Phys. Rev. B **46**, 2223.
Kivelson, S. A., G. Aeppli, and V. J. Emery, 2001, Proc. Natl. Acad. Sci. U.S.A. **98**, 11903.
Kivelson, S. A., E. Fradkin, and V. J. Emery, 1998, Nature (London) **393**, 550.
Kivelson, S. A., D. H. Lee, E. Fradkin, and V. Oganesyan, 2002, Phys. Rev. B **66**, 144516.
Kohn, W., and J. M. Luttinger, 1965, Phys. Rev. Lett. **15**, 524.
Kopec, T. K., and T. A. Zaleski, 2001, Phys. Rev. Lett. **87**, 097002.
Kopec, T. K., and T. A. Zaleski, 2003, Physica C **387**, 65.
Kosterlitz, J. M., D. R. Nelson, and M. E. Fisher, 1976, Phys. Rev. B **13**, 412.
Kotegawa, H., Y. Tokunaga, Y. Araki, G. q. Zheng, Y. Kitaoka, K. Tokiwa, K. Ito, T. Watanabe, A. Iyo, Y. Tanaka, and H. Ihara, 2004, cond-mat/0401416.
Lake, B., G. Aeppli, K. N. Clausen, D. F. McMorrow, K. Lefmann, N. E. Hussey, N. Mangkorntong, M. Nohara, H. Takagi, T. E. Mason, and A. Schroder, 2001, Science **291**, 1759.
Lake, B., H. M. Ronnow, N. B. Christensen, G. Aeppli, K. Lefmann, D. F. McMorrow, P. Vorderwisch, P. Smeibidl, N. Mangkorntong, T. Sasagawa, M. Nohara, H. Takagi, *et al.*, 2002, Nature (London) **415**, 299.
Lanczos, C., 1950, J. Res. Natl. Bur. Stand. **45**, 255.
Lang, K. M., V. Madhavan, J. E. Hoffman, E. W. Hudson, H. Eisaki, S. Uchida, and J. C. Davis, 2002, Nature (London) **415**, 412.
Lanzara, A., P. V. Bogdanov, X. J. Zhou, S. A. Kellar, D. L. Feng, E. D. Lu, T. Yoshida, H. Eisaki, A. Fujimori, K. Kishio, J. I. Shimoyama, T. Noda, *et al.*, 2001, Nature (London) **412**, 510.
Laughlin, R. B., 2002, cond-mat/0209269.
Lee, D. H., and S. A. Kivelson, 2003, Phys. Rev. B **67**, 024506.
Lee, I. J., D. S. Chow, W. G. Clark, J. Strouse, M. J. Naughton, P. M. Chaikin, and S. E. Brown, 2003, Phys. Rev. B **68**, 092510.
Lee, I. J., M. J. Naughton, G. Danner, and P. M. Chaikin, 1997, Phys. Rev. Lett. **78**, 3555.
Lee, P. A., 2002, J. Phys. Chem. Solids **63**, 2149.
Lee, Y. S., R. J. Birgeneau, M. A. Kastner, Y. Endoh, S. Wakimoto, K. Yamada, R. W. Erwin, S. H. Lee, and G. Shirane, 1999, Phys. Rev. B **60**, 3643.
Lefebvre, S., P. Wzietek, S. Brown, C. Bourbonnais, D. Jer-

ome, C. Meziere, M. Fourmigue, and P. Batail, 2000, Phys. Rev. Lett. **85**, 5420.
Levi, B. G., 2002, Phys. Today **55** (2), 14.
Lin, H. H., L. Balents, and M. P. A. Fisher, 1998, Phys. Rev. B **58**, 1794.
Liu, D. Z., Y. Zha, and K. Levin, 1995, Phys. Rev. Lett. **75**, 4130.
Locquet, J. P., J. Perret, J. Fompeyrine, E. Machler, J. W. Seo, and G. V. Tendeloo, 1998, Nature (London) **394**, 453.
Loram, J. W., K. A. Mirza, J. R. Cooper, W. Y. Liang, and J. M. Wade, 1994, J. Supercond. **7**, 243.
Loram, J. W., K. A. Mirza, and P. F. Freeman, 1990, Physica C **171**, 243.
Maggioaprile, I., C. Renner, A. Erb, E. Walker, and O. Fischer, 1995, Phys. Rev. Lett. **75**, 2754.
Maksimov, E., D. Savrasov, and S. Savrasov, 1997, Phys. Usp. **40**, 337.
Mang, P., S. Larochelle, and M. Greven, 2003, cond-mat/0308607.
Manske, D., I. Eremin, and K. H. Bennemann, 2001, Phys. Rev. B **63**, 054517.
Manske, D., I. Eremin, and K. H. Bennemann, 2003, Phys. Rev. B **67**, 134520.
Maple, M. B., 1998, J. Magn. Magn. Mater. **177**, 18.
Markiewicz, R. S., and M. T. Vaughn, 1998, J. Phys. Chem. Solids **59**, 1737.
Marston, J. B., J. O. Fjaerestad, and A. Sudbo, 2002, Phys. Rev. Lett. **89**, 056404.
Mathur, N. D., F. M. Grosche, S. R. Julian, I. R. Walker, D. M. Freye, R. K. W. Haselwimmer, and G. G. Lonzarich, 1998, Nature (London) **394**, 39.
Mazin, I. I., and V. M. Yakovenko, 1995, Phys. Rev. Lett. **75**, 4134.
McElroy, K., R. W. Simmonds, J. E. Hoffman, D.-H. Lee, J. Orenstein, H. Eisaki, S. Uchidak, and J. C. Davis, 2003, Science **422**, 592.
McKenzie, R. H., 1997, Science **278**, 820.
Meixner, S., W. Hanke, E. Demler, and S. C. Zhang, 1997, Phys. Rev. Lett. **79**, 4902.
Micnas, R., J. Ranninger, and S. Robaszkiewicz, 1990, Rev. Mod. Phys. **62**, 113.
Miller, R. J., R. F. Kiefl, J. H. Brewer, J. E. Sonier, D. A. Bonn, W. N. Hardy, R. X. Liang, J. M. Mnard, and P. Poon, 2003, unpublished.
Miller, R. I., R. F. Kiefl, J. H. Brewer, J. E. Sonier, J. Chakhalian, S. Dunsiger, G. D. Morris, A. N. Price, D. A. Bonn, W. H. Hardy, and R. Liang, 2002, Phys. Rev. Lett. **88**, 137002.
Millis, A. J., and H. Monien, 1996, Phys. Rev. B **54**, 16 172.
Mitrovic, V. F., E. E. Sigmund, M. Eschrig, H. N. Bachman, W. P. Halperin, A. P. Reyes, P. Kuhns, and W. G. Moulton, 2001, Nature (London) **413**, 501.
Mitrovic, V. F., E. E. Sigmund, W. P. Halperin, A. P. Reyes, P. Kuhns, and W. G. Moulton, 2003, Phys. Rev. B **67**, 220503.
Molegraaf, H. J. A., C. Presura, D. van der Marel, P. H. Kes, and M. Li, 2002, Science **295**, 2239.
Moler, K. A., J. R. Kirtley, D. G. Hinks, T. W. Li, and M. Xu, 1998, Science **279**, 1193.
Mook, H. A., P. C. Dai, S. M. Hayden, G. Aeppli, T. G. Perring, and F. Dogan, 1998, Nature (London) **395**, 580.
Mook, H. A., P. C. Dai, S. M. Hayden, A. Hiess, J. W. Lynn, S. H. Lee, and F. Dogan, 2002, Phys. Rev. B **66**, 144513.
Mook, H. A., M. Yethiraj, G. Aeppli, T. E. Mason, and T. Armstrong, 1993, Phys. Rev. Lett. **70**, 3490.
Moreo, A., and D. J. Scalapino, 1991, Phys. Rev. Lett. **66**, 946.
Morningstar, C. J., and M. Weinstein, 1996, Phys. Rev. D **54**, 4131.
Morr, D. K., and D. Pines, 1998, Phys. Rev. Lett. **81**, 1086.
Mortensen, N. A., H. M. Ronnow, H. Bruus, and P. Hedegard, 2000, Phys. Rev. B **62**, 8703.
Murakami, S., and N. Nagaosa, 2000, J. Phys. Soc. Jpn. **69**, 2395.
Murakami, S., N. Nagaosa, and M. Sigrist, 1999, Phys. Rev. Lett. **82**, 2939.
Nayak, C., 2000, Phys. Rev. B **62**, R6135.
Nelson, D. R., and J. M. Kosterlitz, 1977, Phys. Rev. Lett. **39**, 1201.
Norman, M. R., and C. Pepin, 2003, Rep. Prog. Phys. **66**, 1547.
Ogata, M., 1999, Int. J. Mod. Phys. B **13**, 3560.
Onufrieva, F., and J. Rossat-Mignod, 1995, Phys. Rev. B **52**, 7572.
Orenstein, J., 1999, Nature (London) **401**, 333.
Orenstein, J., and A. J. Millis, 2000, Science **288**, 468.
Pan, S. H., E. W. Hudson, A. K. Gupta, K. W. Ng, H. Eisaki, S. Uchida, and J. C. Davis, 2000, Phys. Rev. Lett. **85**, 1536.
Pan, S. H., J. P. O'Neal, R. L. Badzey, C. Chamon, H. Ding, J. R. Engelbrecht, Z. Wang, H. Eisaki, S. Uchida, A. K. Guptak, K. W. Ng, E. W. Hudson, *et al.*, 2001, Nature (London) **413**, 282.
Park, K., and S. Sachdev, 2001, Phys. Rev. B **64**, 184510.
Pich, C., and E. Frey, 1998, Phys. Rev. B **57**, 13 712.
Pines, D., and P. Nozières, 1966, *The Theory of Quantum Liquids* (Benjamin Cummings, New York).
Podolsky, D., E. Altman, T. Rostunov, and E. Demler, 2004, cond-mat/0403406.
Podolsky, D., E. Demler, K. Damle, and B. I. Halperin, 2003, Phys. Rev. B **67**, 094514.
Pryadko, L., S. Kivelson, and O. Zachar, 2003, cond-mat/0306342.
Rabello, S., H. Kohno, E. Demler, and S. C. Zhang, 1998, Phys. Rev. Lett. **80**, 3586.
Rajaraman, R., 1982, *Solitons and Instantons* (Elsevier Science, New York).
Riera, J. A., 2002a, Phys. Rev. B **66**, 134523.
Riera, J. A., 2002b, Phys. Rev. B **65**, 174526.
Ronning, F., C. Kim, D. L. Feng, D. S. Marshall, A. G. Loeser, L. L. Miller, J. N. Eckstein, I. Bozovic, and Z. X. Shen, 1998, Science **282**, 2067.
Rossat-Mignod, J., L. P. Regnault, C. Vettier, P. Bourges, P. Burlet, J. Bossy, J. Y. Henry, and G. Lapertot, 1991, Physica C **185**, 86.
Rossat-Mignod, J., L. P. Regnault, C. Vettier, P. Bourges, P. Burlet, J. Bossy, J. Y. Henry, and G. Lapertot, 1992, Physica B **180**, 383.
Rossat-Mignod, J., L. P. Regnault, C. Vettier, P. Burlet, J. Y. Henry, and G. Lapertot, 1991, Physica B **169**, 58.
Rozhkov, A. V., and A. J. Millis, 2002, Phys. Rev. B **66**, 134509.
Sachdev, S., 1992, Phys. Rev. B **45**, 389.
Sachdev, S., 2000, *Quantum Phase Transitions* (Cambridge University, Cambridge, England).
Sachdev, S., 2002a, Rev. Mod. Phys. **75**, 913.
Sachdev, S., 2002b, Ann. Phys. (N.Y.) **303**, 226.
Sachdev, S., and R. N. Bhatt, 1990, Phys. Rev. B **41**, 9323.
Sachdev, S., and E. Demler, 2004, Phys. Rev. B **69**, 144504.
Sachdev, S., and M. Vojta, 2000, in *New Theoretical Approaches to Strongly Correlated Systems*, Lectures at the NATO Advanced Study Institute/EC Summer School, edited

by A. M. Tsvelik (Kluwer Academic, Dordrecht).
Sachdev, S., and S. C. Zhang, 2002, Science **295**, 452.
Sandvik, A. W., 1997, Phys. Rev. B **56**, 11 678.
Sandvik, A. W., 1999, Phys. Rev. B **59**, R14 157.
Sato, H., A. Tsukada, M. Naito, and A. Matsuda, 2000, Phys. Rev. B **62**, R799.
Scalapino, D., S. C. Zhang, and W. Hanke, 1998, Phys. Rev. B **58**, 443.
Scalapino, D. J., 1970, Phys. Rev. Lett. **24**, 1052.
Scalapino, D. J., 1995, Phys. Rep. **250**, 330.
Scalapino, D. J., and S. R. White, 1998, Phys. Rev. B **58**, 8222.
Scalettar, R. T., G. G. Batrouni, A. P. Kampf, and G. T. Zimanyi, 1995, Phys. Rev. B **51**, 8467.
Scalettar, R. T., E. Y. Loh, J. E. Gubernatis, A. Moreo, S. R. White, D. J. Scalapino, R. L. Sugar, and E. Dagotto, 1989, Phys. Rev. Lett. **62**, 1407.
Schachinger, E., J. P. Carbotte, and D. N. Basov, 2001, Europhys. Lett. **54**, 380.
Schollwoeck, U., S. Chakravarty, J. O. Fjaerestad, J. B. Marston, and M. Troyer, 2003, Phys. Rev. Lett. **90**, 186401.
Schrieffer, J. R., 1964, *Theory of Superconductivity* (Benjamin Cummings, New York).
Schrieffer, J. R., X. G. Wen, and S. C. Zhang, 1989, Phys. Rev. B **39**, 11 663.
Schulz, H., 1998, cond-mat/9808167.
Senthil, T., and M. P. A. Fisher, 2001, Phys. Rev. B **63**, 134521.
Senthil, T., A. Vishwanath, L. Balents, S. Sachdev, and M. P. A. Fisher, 2004, Science **303**, 1490.
Sheehy, D. E., and P. M. Goldbart, 1998, Phys. Rev. B **57**, R8131.
Shelton, D. G., and D. Senechal, 1998, Phys. Rev. B **58**, 6818.
Shen, K. M., *et al.*, 2004, Phys. Rev. B **69**, 054503.
Shen, Z. X., A. Lanzara, S. Ishihara, and N. Nagaosa, 2002, Philos. Mag. B **82**, 1349.
Sidis, Y., C. Ulrich, P. Bourges, C. Bernhard, C. Niedermayer, L. P. Regnault, N. H. Andersen, and B. Keimer, 2001, Phys. Rev. Lett. **86**, 4100.
Singleton, J., and C. Mielke, 2002, Contemp. Phys. **43**, 63.
Sorella, S., G. B. Martins, F. Becca, C. Gazza, L. Capriotti, A. Parola, and E. Dagotto, 2002, Phys. Rev. Lett. **88**, 117002.
Stock, C., W. Buyers, R. Liang, D. Peets, Z. Tun, D. Bonn, W. Hardy, and R. Birgeneau, 2004, Phys. Rev. B **69**, 014502.
Suzuki, Y., J. M. Triscone, C. B. Eom, M. R. Beasley, and T. H. Geballe, 1994, Phys. Rev. Lett. **73**, 328.
Takeshita, N., T. Sasagawa, T. Sugioka, Y. Tokural, and H. Takagi, 2003, cond-mat/0305111.
Tallon, J. L., and J. W. Loram, 2001, Physica C **349**, 53.
Taniguchi, H., K. Kanoda, and A. Kawamoto, 2003, Phys. Rev. B **67**, 014510.
Timusk, T., and B. Statt, 1999, Rep. Prog. Phys. **62**, 61.
Tinkham, M., 1995, *Introduction to Superconductivity* (McGraw-Hill, New York).
Tranquada, J. M., B. J. Sternlieb, J. D. Axe, Y. Nakamura, and S. Uchida, 1995, Nature (London) **375**, 561.
Tsuchiura, H., M. Ogata, Y. Tanaka, and S. Kashiwaya, 2003, J. Low Temp. Phys. **131**, 209.
Tsuei, C. C., and J. R. Kirtley, 2000, Rev. Mod. Phys. **72**, 969.
Uemura, Y., 2002, Solid State Commun. Special Issue, edited by Y. U. A. J. Millis and S. Uchida.
Uemura, Y. J., G. M. Luke, B. J. Sternlieb, J. H. Brewer, J. F. Carolan, W. N. Hardy, R. Kadono, J. R. Kempton, R. F. Kiefl, S. R. Kreitzman, P. Mulhern, T. M. Riseman, *et al.*, 1989, Phys. Rev. Lett. **62**, 2317.
van der Linden, W., 1992, Phys. Rep. **220**, 53.
van Duin, C. N. A., and J. Zaanen, 2000, Phys. Rev. B **61**, 3676.
van Harlingen, D. J., 1995, Rev. Mod. Phys. **67**, 515.
van Otterlo, A., K. H. Wagenblast, R. Baltin, C. Bruder, R. Fazio, and G. Schon, 1995, Phys. Rev. B **52**, 16 176.
Varma, C. M., 1999, Phys. Rev. Lett. **83**, 3538.
Vershinin, M., S. Misra, S. Ono, S. Abe, Y. Ando, and A. Yazdani, 2004, cond-mat/0402320.
Vojta, M., 2002, Phys. Rev. B **66**, 104505.
Vojta, M., and S. Sachdev, 1999, Phys. Rev. Lett. **83**, 3916.
Vonsovsky, S. V., Y. A. Izyumov, and E. Z. Kurmaev, 1982, *Superconductivity of Transition Metals* (Springer, New York).
Vuletic, T., P. Auban-Senzier, C. Pasquier, D. Jerome, M. Heritier, and K. Bechgaard, 2002, Eur. Phys. J. B **25**, 319.
Wakimoto, S., R. J. Birgeneau, M. A. Kastner, Y. S. Lee, R. Erwin, P. M. Gehring, S. H. Lee, M. Fujita, K. Yamada, Y. Endoh, K. Hirota, and G. Shirane, 2000, Phys. Rev. B **61**, 3699.
Wakimoto, S., R. J. Birgeneau, Y. S. Lee, and G. Shirane, 2001, Phys. Rev. B **63**, 172501.
Wang, Y., and A. H. Macdonald, 1995, Phys. Rev. B **52**, R3876.
Wegner, F. J., 2000, Eur. Phys. J. B **14**, 11.
Weinberg, S., 1995, *The Quantum Theory of Fields* (Cambridge University, New York).
Wen, X. G., and P. A. Lee, 1996, Phys. Rev. Lett. **76**, 503.
Weng, Z. Y., D. N. Sheng, and C. S. Ting, 1998, Phys. Rev. Lett. **80**, 5401.
White, S. R., and D. J. Scalapino, 1998, Phys. Rev. Lett. **80**, 1272.
Wu, C., V. W. Liu, and E. Fradkin, 2003, Phys. Rev. B **68**, 115104.
Wu, C. J., H. D. Chen, J. P. Hu, and S. C. Zhang, 2004, Phys. Rev. A **69**, 043609.
Wu, C. J., J. P. Hu, and S. C. Zhang, 2003, Phys. Rev. Lett. **91**, 186402.
Wu, L. A., M. Guidry, Y. Sun, and C. L. Wu, 2003, Phys. Rev. B **67**, 014515.
Wu, M. K., J. R. Ashburn, C. J. Torng, P. H. Hor, R. L. Meng, L. Gao, Z. J. Huang, Y. Q. Wang, and C. W. Chu, 1987, Phys. Rev. Lett. **58**, 908.
Yamada, K., C. H. Lee, K. Kurahashi, J. Wada, S. Wakimoto, S. Ueki, H. Kimura, Y. Endoh, S. Hosoya, G. Shirane, R. J. Birgeneau, M. Greven, *et al.*, 1998, Phys. Rev. B **57**, 6165.
Yang, C. N., 1989, Phys. Rev. Lett. **63**, 2144.
Yang, C. N., and S. C. Zhang, 1990, Mod. Phys. Lett. B **4**, 759.
Yeh, N., 2002, Bull. Assoc. Asia Pacific Phy. Socs. (AAPPS) **12**, 2.
Yin, L., S. Chakravarty, and P. W. Anderson, 1997, Phys. Rev. Lett. **78**, 3559.
Yokoyama, H., and M. Ogata, 1996, J. Phys. Soc. Jpn. **65**, 3615.
Yoshikawa, H., and T. Moriya, 1999, J. Phys. Soc. Jpn. **68**, 1340.
Zaanen, J., 1999a, Physica C **317-318**, 217.
Zaanen, J., 1999b, Science **286**, 251.
Zaanen, J., and O. Gunnarsson, 1989, Phys. Rev. B **40**, 7391.
Zacher, M. G., W. Hanke, E. Arrigoni, and S. C. Zhang, 2000, Phys. Rev. Lett. **85**, 824.
Zaleski, T. A., and T. K. Kopec, 2000a, Physica C **341**, 237.
Zaleski, T. A., and T. K. Kopec, 2000b, Phys. Rev. B **62**, 9059.
Zasadzinski, J. F., L. Coffey, P. Romano, and Z. Yusof, 2003, Phys. Rev. B **68**, 180504.
Zhang, F. C., C. Gros, T. M. Rice, and H. Shiba, 1988, Supercond. Sci. Technol. **1**, 36.
Zhang, F. C., and T. M. Rice, 1988, Phys. Rev. B **37**, 3759.

Zhang, S. C., 1990, Phys. Rev. Lett. **65**, 120.
Zhang, S. C., 1991, Int. J. Mod. Phys. B **5**, 153.
Zhang, S. C., 1997, Science **275**, 1089.
Zhang, S. C., 1998, cond-mat/9808309.
Zhang, S. C., J. P. Hu, E. Arrigoni, W. Hanke, and A. Auerbach, 1999, Phys. Rev. B **60**, 13 070.
Zhang, Y., E. Demler, and S. Sachdev, 2002, Phys. Rev. B **66**, 094501.